

QUANTUM FIELD THEORY IN LOW-DIMENSIONAL
CONDENSED-MATTER SYSTEMS

Quantum field theory in low-dimensional condensed-matter systems

Natália Menezes Silva da Costa

Ph.D. Thesis Utrecht University, August 2018

ISBN: 978-90-393-7027-8

Printed by: Xerox

QUANTUM FIELD THEORY IN LOW-DIMENSIONAL
CONDENSED-MATTER SYSTEMS

KWANTUMVELDENTHEORIE IN LAAGDIMENSIONALE
GECONDENSEERDE MATERIESYSTEMEN

(met een samenvatting in het Nederlands)

Proefschrift

ter verkrijging van de graad van doctor aan de Universiteit Utrecht op
gezag van de rector magnificus, prof. dr. H.R.B.M. Kummeling, ingevolge het
besluit van het college voor promoties in het openbaar te verdedigen op maandag
27 augustus 2018 des middags te 2.30 uur

door

NATÁLIA MENEZES SILVA DA COSTA

geboren op 28 december 1990 te Recife, Brazilië

Promotor: Prof. dr. C. de Morais Smith

CONTENTS

1	Introduction	1
2	Graphene as a Dirac material	11
2.1	Tight-binding model for monolayer graphene	11
2.2	Graphene' spinful low-energy theory	14
2.3	Remarks on the Dirac theory	15
2.4	Electromagnetic interactions in the plane	17
3	Weak external magnetic fields in graphene-like systems	21
3.1	Introduction	21
3.2	The model	24
3.3	Electron self-energy	25
3.3.1	The zero-mass case	26
3.3.2	Weak magnetic field approximation	27
3.3.3	The fermionic mass contribution	29
3.4	Renormalization group study	30
3.4.1	Velocity renormalization	31
3.4.2	The running mass	32
3.5	Conclusions	33
3.A	Details of the Self-energy calculations	34
3.B	Renormalization-group calculations	36
4	On the spin gyromagnetic factor in graphene	39
4.1	Introduction	39
4.2	Anisotropic pseudo-QED	40
4.3	The electron (2+1)D vertex function	41
4.4	Form factor calculation	43
4.5	Comparison with experiments	45
4.5.1	Graphene on SiO ₂	45
4.5.2	Graphene on SiC(111)	50

4.6	Conclusions	51
4.A	Form factor detailed calculation	51
5	Excitonic gap generation in thin-film topological insulators	57
5.1	Introduction	57
5.2	The model	59
5.3	Single-surface description	62
5.4	Dynamical gap generation	63
5.4.1	Short-range interactions	63
5.4.2	Long-range interaction	67
5.4.3	Application: Bi ₂ Se ₃ thin-film	68
5.5	Conclusions	69
5.A	Effective interactions after projection	70
5.B	Derivation of interactions in Eq. (5.3.5)	70
5.C	η -function in the strong coupling regime	72
6	Emergent helical Luttinger liquid in 2D topological insulators from electromagnetic interactions	75
6.1	Introduction	75
6.2	Conformal QED on the boundary of topological insulators	77
6.3	Thirring model and helical Luttinger liquid	80
6.4	Luttinger-parameter discussion	81
6.5	Conclusions	83
6.A	Details on the projection from (3+1)D to (1+1)D	84
6.B	Effective action and (1+1)D Lagrangian	87
6.C	Details on the bosonization procedure	88
6.D	Masses in the Thirring model and the backscattering interaction	92
7	Atypical Hall conductivity in the Varma phase	95
7.1	Introduction	95
7.2	DKP theory on the Lieb lattice	97
7.3	Landau levels in the DKP theory	99
7.4	Chern-Simons theory and Hall conductivity	100
7.5	Edge modes	102
7.6	Experimental realization	104
7.7	Conclusions	105
7.A	Low-energy Hamiltonian	105
7.B	DKP Landau-level solution	106
7.C	Polarization tensor details	109
	Bibliography	111
	Summary	123
	Samenvatting	126

Acknowledgments	131
Curriculum Vitae	133

PUBLICATIONS

This thesis is based on the following publications:

- N. Menezes, Van Sergio Alves and C. Morais Smith, *The influence of a weak magnetic field in the Renormalization-Group functions of (2+1)-dimensional Dirac systems*, Eur. Phys. J. B **89**, 271 (2016), Editor's choice.
- N. Menezes, Van Sergio Alves, E. C. Marino, L. Nascimento, Leandro O. Nascimento and C. Morais Smith, *Spin g-factor due to electronic interactions in graphene*, Phys. Rev. B **95**, 245138 (2017).
- N. Menezes, C. Morais Smith and G. Palumbo, *Excitonic Gap Generation in Thin-Film Topological Insulators*, J. Phys.: Condens. Matter **29**, 335601 (2017).
- N. Menezes, G. Palumbo and C. Morais Smith, *Conformal QED in Two-Dimensional Topological Insulators*, Sci. Rep. **7**, 14175 (2017).
- N. Menezes, C. Morais Smith and G. Palumbo, *Chern-Simons theory and atypical Hall conductivity in the Varma phase*, Phys. Rev. B **97**, 075135 (2018).

Other works to which the author has contributed:

- S. H. Kooi, N. Menezes, Van Sergio Alves and C. Morais Smith, *Quantum Valley Hall Effect in Massive Dirac Systems Coupled to a Scalar Field*, arXiv:cond-mat/1702.02812.
- E. C. Marino, L. O. Nascimento, V. S. Alves, N. Menezes and C. Morais Smith, *Quantum-electrodynamical approach to the exciton spectrum in Transition-Metal Dichalcogenides*, arXiv:cond-mat/1710.08960, accepted for publication in 2D Materials.

DEFINITIONS & ABBREVIATIONS

Some common definitions among the different chapters:

- In this thesis, different fields are being used to describe the quasiparticles and the mediators of the interactions. Here, we resume the nature of those fields: Ψ, ψ are Dirac fields; $\phi_i, \varphi, \theta, \chi$ are bosonic fields; and $A_\mu, \mathcal{A}_\mu^i, W_\mu^i, h_\mu$ are the gauge fields.
- The Minkowski metric is used in all chapters, both in (2+1)D and (1+1)D, and the signature is either $g^{\mu\nu} = \text{diag}(1, -1, -1)$ or $\text{diag}(1, -1)$.
- The Fermi velocity is often written as v_F , while the speed of light is c . We define their ration as $\beta \equiv v_F/c$.
- If not written explicitly, then the Planck constant and the speed of light are taken as $\hbar = c = 1$.
- ε denotes the dielectric constant of a material, and $\varepsilon_0 = 1$ is its value in the vacuum.
- α represents the fine-structure constant of a material, and e is the electric charge.
- K_L denotes the Luttinger parameter.
- \mathcal{B} denotes magnetic field, n is the density, \mathcal{N} is the Landau level index and N is flavor.
- $\gamma^\mu, \sigma^\mu, \beta^\mu$ are the Dirac, Pauli and Duffin-Kemmer-Petiau matrices, respectively.

Abbreviations along the text:

- $(\mathcal{Q}^1+1)D$: Spacetime dimensions
- $\mathcal{Q} D$: Spatial dimensions
- QED: Quantum electrodynamics
- PQED: Pseudo-quantum electrodynamics
- CQED: Conformal quantum electrodynamics
- TI(s): Topological insulator(s)
- DKP: Duffin-Kemmer-Petiau
- HLL: Helical Luttinger liquid
- QHE: Quantum Hall effect
- QSHE: Quantum spin Hall effect
- QAHE: Quantum anomalous Hall effect
- FQHE: Fractional quantum Hall effect
- RG: Renormalization group
- TMDs: Transition metal dichalcogenides

¹ $\mathcal{Q} = 1, 2$ or 3 .

INTRODUCTION

The low-energy physics of quantum systems often reveals emergent phenomena due to a collective behavior of the particles, and interactions among them can lead to surprising effects.

Graphene

Graphene is a 2D semimetal made out of carbon atoms, which basically is an atom-thick sheet of (bulk) graphite. Although theoretical studies of a 2D version of graphite are dated to the past century, only in 2004 graphene was isolated and characterized [1, 2]. This experimental realization yielded the Nobel prize in 2010 for Andre Geim and Konstantin Novoselov, and boosted the research in condensed-matter physics towards novel 2D materials.

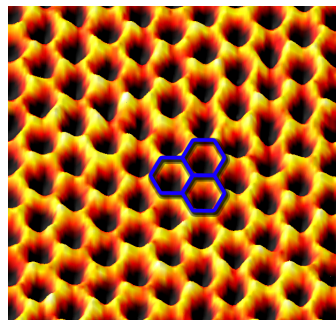


Figure 1.1: A sheet of suspended graphene from TEAM (Transmission Electron Aberration-Corrected Microscope) displays individual carbon atoms in yellow on the honeycomb lattice (the blue contour was added to show the lattice structure). Figure extracted from Ref. [3].

The energy configuration of a material is intrinsically related to the arrangement of the atoms in a lattice. In graphene, the carbon atoms are organized in a

honeycomb structure (see Fig. 1.1) and the mobile electrons exhibit a relativistic-like dispersion at low-energies. This turned graphene into a platform for studies on the Dirac theory in condensed matter. A linear energy spectrum commonly suggests that a given system is critical, and interaction effects may be suppressed below a critical value of the interaction. Hence, for long, a non-interacting theory of graphene had been considered sufficient to describe its physics. However, further investigation has shown that electronic interactions may play a relevant role.

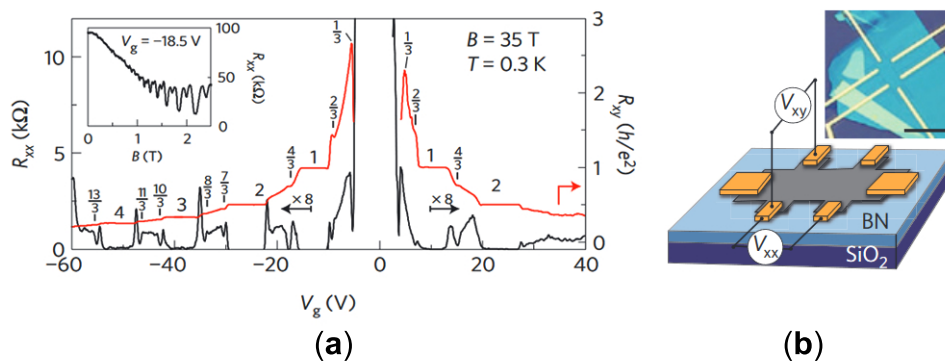


Figure 1.2: **(a)** Magnetoresistance and Hall resistance measurements versus gate voltage at magnetic fields of 35T. **(b)** Schematic representation of the Hall bar device. Figures extracted from Ref. [4].

Magnetoresistance experiments performed on a graphene sample deposited on a hexagonal boron-nitride substrate using strong magnetic fields, such as 35T, show signatures of fractional quantization of the Hall resistance [4], i.e. fractional quantum Hall effect (FQHE), with $R_{xy} = (1/\nu)h/e^2$ (see Figs. 1.2 **(a)** and **(b)**). The observed fractions at which the Hall conductivity exhibits plateaus indicate states of interacting electrons, where the excitations have a fractional value of the elementary charge. Earlier experiments on suspended graphene [5, 6] exhibited similar features.

In addition, not long after the experiments on the FQHE, the analysis of the Shubnikov-de Haas (SdH) oscillations in suspended graphene probed the renormalization of its low-energy linear spectrum [7]. By measuring SdH oscillations for different values of magnetic field and electron density as a function of temperature, and using the Lifshitz-Kosevich formula, the group of Geim and Novoselov found effective values of the cyclotron mass at a given density, $m_c = \hbar\sqrt{\pi n}/v_F^*$. From this relation, the Fermi velocity displayed a logarithmic deviation from the linear behavior, thus, reshaping the energy dispersion (see Figs. 1.3 **(a)** and **(b)**). This result has been further confirmed experimentally [8, 9], and also successfully

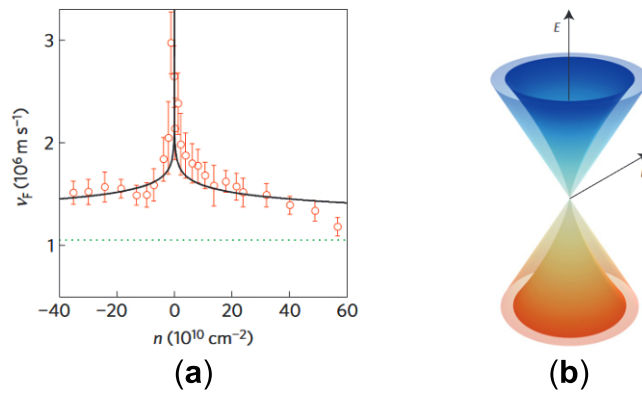


Figure 1.3: (a) Experimental data probing the renormalization of the Fermi velocity and (b) illustration of the low-energy dispersion reshaping due to interactions. Figures extracted from Ref. [7].

explained through a renormalization group study of electronic interactions in 2D Dirac-like systems [10–15].

Moreover, new measurements of SdH oscillations – in tilted magnetic fields – revealed a spin degeneracy lifting that could not be justified in terms of single-particle physics [16]. For this experiment, graphene was deposited on top of a SiO_2 substrate, and the spin g -factor was obtained by analyzing how the SdH oscillation amplitudes increase upon changing the applied magnetic fields. In the case of non-interacting electrons, the Dirac theory predicts a value 2 for the spin g -factor, and it is well-known in particle physics that this value may be modified due to interaction effects [17–20]. This also seems to be the case for graphene (see Fig. 1.4), because the experiments suggest that the spin g -factor enhancement is due to a collective behavior. Additional resolution of the spin degeneracy lifting in graphene on SiC has confirmed this picture [21].

All the experiments that we have briefly discussed enlighten the importance of interactions in graphene. On the theoretical side, the renormalization of the Fermi velocity reveals itself to be the key ingredient for the signature of interaction effects. Many theoretical works have proved its logarithmic behavior [10–15]. However, fewer studies attempted at explaining the corrections to the spin g -factor and how to connect it with the renormalization of the Fermi velocity. This issue is discussed in the original research work presented in chapter 4. Furthermore, all the mentioned experiments to reveal the effect of interactions in graphene were performed in the presence of external magnetic fields. Yet, previous theoretical studies on the renormalization of the Fermi velocity neither considered the effect of an external magnetic field nor justified why it is not necessary to do so. Hence, the question on whether the magnetic field influences the renormalization of such important physical parameter was still open, and we address it in this thesis in

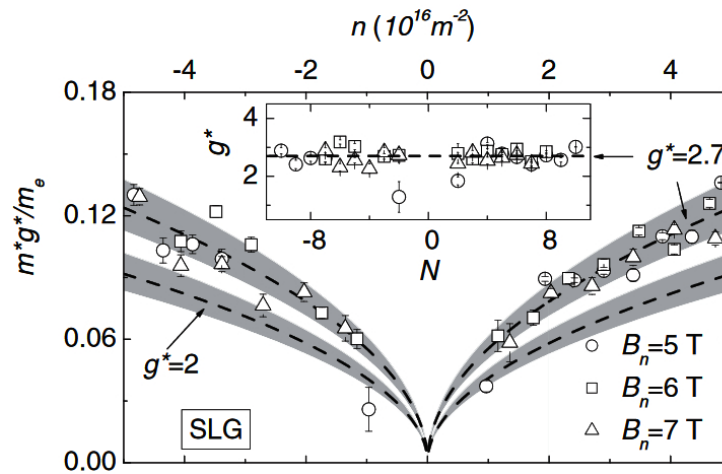


Figure 1.4: Experimental data for the spin gyromagnetic factor in single-layer graphene deposited on SiO_2 . Figure extracted from Ref. [16].

chapter 3.

Topological Insulators

Not only graphene has low-energy excitations that resemble massless Dirac fermions, but also another class of materials known as topological insulators (TIs). These are materials characterized by an insulating bulk while their edges/surfaces conduct electrons, as represented in Figs. 1.5 (a). The peculiarity of this kind of material lies on the fact that the conducting edges/surfaces are protected by charge

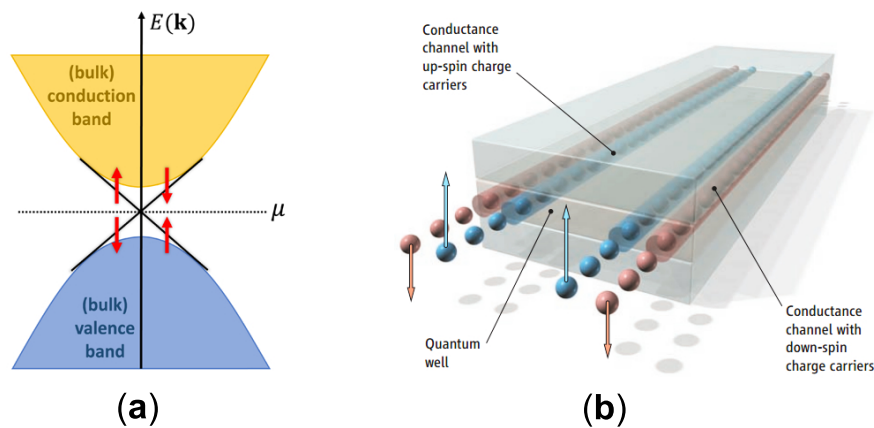


Figure 1.5: (a) Illustrative picture of the topological insulator non-trivial band structure. (b) Schematic picture of the QSHE extracted from Ref. [22].

conservation and time-reversal symmetry. The system is robust against local perturbations, as long as they do not break the symmetries. Because the spin configuration is locked to the momentum propagation – known as spin-momentum locking – quantized spin currents counter-propagate at the edges, as shown in Fig. 1.5 (b).

The original proposal for the occurrence of this type of non-trivial insulator was made for graphene [23]. However, the spin-orbit coupling that gives rise to the effect, by opening a gap while preserving time-reversal symmetry, is not strong enough in carbon atoms. Nevertheless, later on, the search for this new state of matter succeeded by considering a different kind of semiconductor: HgTe/(Hg,Cd)Te quantum wells [22, 24]. Measurements of the longitudinal resistance as a function of the gate voltage at zero magnetic fields revealed a conductance of $2e^2/h$, meaning that each edge channel contributes with an unit of the quantized conductance [22]. Although the first works on TIs were performed for 2D materials, similar versions of TIs in 3D have been theoretically formulated [25], and then experimentally discovered [26, 27]. Instead of 1D edges, these systems support 2D surface gapless modes, which are topologically protected by symmetry.

In order to distinguish a trivial from a non-trivial band insulator in time-reversal-invariant systems, Kane and Mele introduced the concept of \mathbb{Z}_2 topological invariant [28]. This quantity is either even or odd, and counts the number of degenerated (Kramer) pairs of edge modes. Essentially, for an even number of degenerated pairs the system reveals to be a trivial insulator, while for an odd number, the result is a TI. So far, the classification of these fermionic topological phases has been successfully established for the case of non-interacting systems, for all dimensions, in terms of their symmetries [29–32], as depicted in Fig. 1.6. However, much less is known about the complete classification and characterization of interacting systems, for which a variety of quantum phenomena and quasi-particles emerge in the low-energy regime.

At this point, it is important to distinguish systems with symmetry protected topological order (short-range entangled states) from those topologically ordered (long-range entangled states). The TIs discussed here are part of the first group, while the FQHE is a subject of the second group. Interactions per se on top of symmetry protected systems cannot change the short-range nature of their entangled states into a long-range one. Nevertheless, interactions may drive the transition from a trivial to a non-trivial insulator, and also lead to interesting phenomena in the scope of Landau theory for continuous phase transitions and more. In chapters 5 and 6, we address the role of electromagnetic interactions in 3D and 2D TIs.

Topological materials are, nowadays, a rich and well developed research field in condensed-matter physics. However, it is worth to recall that the study of

Periodic table of topological insulators/superconductors

Cartan	d												
	0	1	2	3	4	5	6	7	8	9	10	11	...
<i>Complex case:</i>													
A	\mathbb{Z}	0	\mathbb{Z}	0	\mathbb{Z}	0	\mathbb{Z}	0	\mathbb{Z}	0	\mathbb{Z}	0	...
AIII	0	\mathbb{Z}	0	\mathbb{Z}	0	\mathbb{Z}	0	\mathbb{Z}	0	\mathbb{Z}	0	\mathbb{Z}	...
<i>Real case:</i>													
AI	\mathbb{Z}	0	0	0	$2\mathbb{Z}$	0	\mathbb{Z}_2	\mathbb{Z}_2	\mathbb{Z}	0	0	0	...
BDI	\mathbb{Z}_2	\mathbb{Z}	0	0	0	$2\mathbb{Z}$	0	\mathbb{Z}_2	\mathbb{Z}_2	\mathbb{Z}	0	0	...
D	\mathbb{Z}_2	\mathbb{Z}_2	\mathbb{Z}	0	0	0	$2\mathbb{Z}$	0	\mathbb{Z}_2	\mathbb{Z}_2	\mathbb{Z}	0	...
DIII	0	\mathbb{Z}_2	\mathbb{Z}_2	\mathbb{Z}	0	0	0	$2\mathbb{Z}$	0	\mathbb{Z}_2	\mathbb{Z}_2	\mathbb{Z}	...
AII	$2\mathbb{Z}$	0	\mathbb{Z}_2	\mathbb{Z}_2	\mathbb{Z}	0	0	0	$2\mathbb{Z}$	0	\mathbb{Z}_2	\mathbb{Z}_2	...
CII	0	$2\mathbb{Z}$	0	\mathbb{Z}_2	\mathbb{Z}_2	\mathbb{Z}	0	0	0	$2\mathbb{Z}$	0	\mathbb{Z}_2	...
C	0	0	$2\mathbb{Z}$	0	\mathbb{Z}_2	\mathbb{Z}_2	\mathbb{Z}	0	0	0	$2\mathbb{Z}$	0	...
CI	0	0	0	$2\mathbb{Z}$	0	\mathbb{Z}_2	\mathbb{Z}_2	\mathbb{Z}	0	0	0	$2\mathbb{Z}$...

Figure 1.6: Periodic table: classification of non-interacting topological insulators and topological superconductors from Refs. [31–33].

2D topological systems started in the early 80's, with the experimental discovery of the integer quantum Hall effect (IQHE) in GaAs [34]. Thereafter, the deep relation between this novel phase and the topological invariant (namely, Chern number) induced by a non-trivial Berry phase was theoretically unveiled [35]. An essential feature of these quantum states is that time-reversal symmetry is broken in the bulk. Next, we discuss the breaking of this symmetry within a model that goes beyond the Dirac fermions picture used to describe both graphene and the boundary of TIs.

Chern insulator beyond Dirac materials

The basic idea behind the IQHE lies on the effect of a strong perpendicular magnetic field (at low temperatures) on a 2D quantum electronic system. The magnetic field breaks time-reversal symmetry by modifying the motion of the electrons and forcing them to realize quantized circular orbits that are either clockwise or counterclockwise. In a finite-size system, such cyclotron orbits are disrupted at the edges of the material, leading to chiral currents that are quantized in units of e^2/h .

Not long after the discovery of the IQHE, a fundamental question of how to generate similar phenomenon without external magnetic fields emerged, and it was solved by Haldane based on symmetry aspects [36]. He showed that by breaking time-reversal symmetry with fluxes within a honeycomb lattice (see Fig. 1.7), chiral currents may be generated even in the absence of a magnetic field. Because

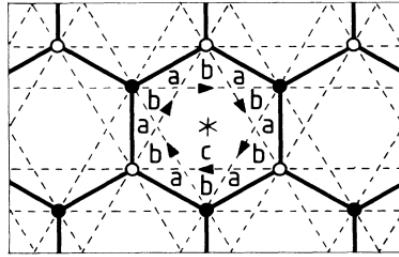


Figure 1.7: The Haldane phase indicated by the arrows connecting the next-nearest-neighbors. Figure extracted from Ref. [36].

the mechanism that drives the symmetry breaking is not a real external magnetic field, there are no Landau levels. This phenomenon became known as the QAHE and the material as Chern insulator.

Motivated by the burst of topological phases, the search for different topological materials from different lattice configurations increased considerably. This was the case of the Lieb lattice, which is nothing but a decorated square lattice (see Fig. 1.8 (a)). This is actually the planar lattice of high-Tc cuprates. In the context of high-Tc cuprates, Varma proposed that a broken time-reversal symmetry phase, with staggered currents flowing in the plaquettes in a way to preserve translational symmetry as shown in Fig. 1.8 (a), should be responsible for the pseudogap phase of cuprates [37]. Similarly to the Haldane phase, the Varma phase also displays the QAHE.

Here, the novelty lies on the low-energy behavior of such copper-oxide system, which is a bit different from graphene or topological insulators. Its spectrum is not solely represented by a Dirac cone, but also contains a zero energy (flat)

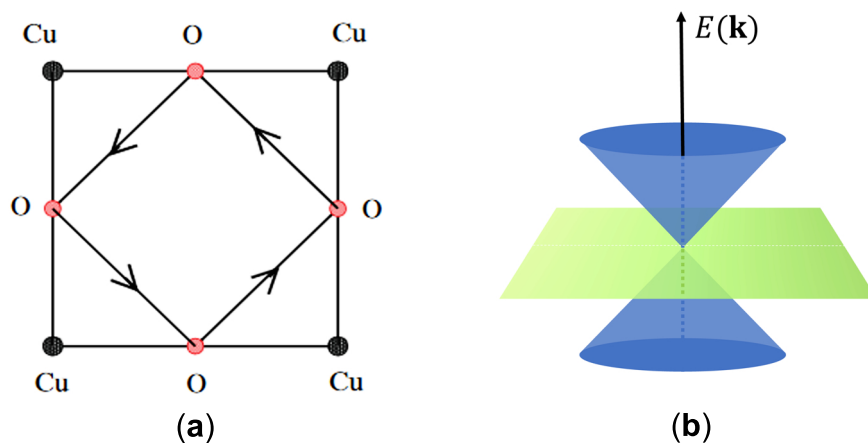


Figure 1.8: (a) Varma phase from Ref. [37]. (b) Illustrative picture of the low-energy spectrum of the copper-oxide (CuO_2) model.

band (see Fig. 1.8 (b)). The non-dispersive band changes the character of the low-energy quasiparticles, which cannot be described by a Dirac Hamiltonian. In recent literature, this kind of model is also known as the pseudospin-1 system because the lattice structure is made out of three sublattices, and their algebra may be formulated in terms of spin-1 matrices (instead of spin-1/2 Pauli matrices).

Originally, the copper-oxide lattice model was introduced for the studies of high-Tc cuprates, and these compounds are actually 3D structures. Therefore, experimental measurements on the 2D physics of the copper-oxide Lieb lattice seemed not to be possible until recent years, when similar lattice models were implemented in artificial electronic [38, 39] and photonic [40–42] systems. The experimental access to 2D integer-pseudospin systems has not only opened the way to probe novel quantum phenomena, but also has stimulated the theoretical research on the physics beyond Dirac materials. Motivated by these considerations, we have investigated in Chapter 7 the topological response of the Varma phase mentioned above through the Chern-Simons theory from a relativistic field theory description beyond Dirac fermions, known as the Duffin-Kemmer-Petiau (DKP) theory.

Outline

The scope of this thesis is to investigate interaction effects and gauge fields in condensed-matter systems through quantum field theory techniques. We divided the work in this thesis in two parts: the first concerns the research developed in graphene; while the second refers to the works on 2D and 3D topological insulators with, and without, time-reversal symmetry.

In Chapter 2, we review the basic physics behind graphene, its mapping to the Dirac theory and discuss a framework to treat electromagnetic interactions. The concepts presented in Chapter 2 are needed for the understanding of the model used in the original work in Chapter 3, where we address the question on whether and how weak magnetic fields would modify the renormalization of the Fermi velocity. To conclude the first part of this thesis, in Chapter 4, we compute the corrections to the spin gyromagnetic factor due to interactions and compare the results with experiments.

In the second part of this thesis, we investigate the effect of electromagnetic interactions in 3D thin films of time-reversal-invariant TIs in chapter 5, while in Chapter 6, we consider materials with one dimension lower and look at the effect of interactions at the boundary of 2D time-reversal-invariant TIs. At last, in Chapter 7, we investigate the topological response of the Varma phase of a cuprate lattice. Some of the chapters are accompanied by appendix sections with details of the original work. A summary of this thesis is presented at the end.

PART I: MONOLAYER GRAPHENE
AND INTERACTIONS

GRAPHENE AS A DIRAC MATERIAL

In this chapter, we review the physics of graphene from the tight-binding model to its low-energy continuum theory. At small momenta, graphene exhibits an emergent linear dispersion, which can be described by a 2D Dirac theory. By coupling this Dirac-like theory to a quantum electromagnetic field in 3D, we show how to obtain a description that takes into account the dimensional mismatch between light and matter. The result is a dimensional reduced theory known as PQED. This preliminary knowledge is needed for the understanding of the original work presented in Chapters 4 and 3.

2.1 Tight-binding model for monolayer graphene

Graphene is a two-dimensional material solely made of carbon atoms distributed in a hexagonal (or honeycomb-like) lattice (see Fig. 2.1 (a)). To describe such bi-dimensional structure, we consider a triangular Bravais¹ lattice with a basis given in terms of two carbon atoms A and B , where the later correspond to a mirror image of the former. The primitive lattice vectors \mathbf{a}_1 and \mathbf{a}_2 in the A -atom sublattice are

$$\mathbf{a}_1 = \frac{a}{2} (3, \sqrt{3}), \quad \mathbf{a}_2 = \frac{a}{2} (3, -\sqrt{3}), \quad (2.1.1)$$

where $a = 1.42\text{\AA}$ is the shortest distance between two carbon atoms. We determine the vectors of the reciprocal (Fourier space) lattice by using the condition $\mathbf{a}_i \cdot \mathbf{a}_j^* =$

¹A Bravais lattice is defined as an infinite distribution of discrete points generated by a set of translation operators \mathbf{T} in the basis of the primitive vectors \mathbf{a}_i , i.e. $\mathbf{T} = n_i \mathbf{a}_i$ ($n_i \in \mathbb{Z}$). This definition does not apply to the honeycomb lattice, which has nonequivalent points (A and B) that cannot be reproduced by the same operator \mathbf{T} .

$2\pi\delta_{ij}$,

$$\mathbf{a}_1^* = \frac{2\pi}{3a} (1, \sqrt{3}), \quad \mathbf{a}_2^* = \frac{2\pi}{3a} (1, -\sqrt{3}). \quad (2.1.2)$$

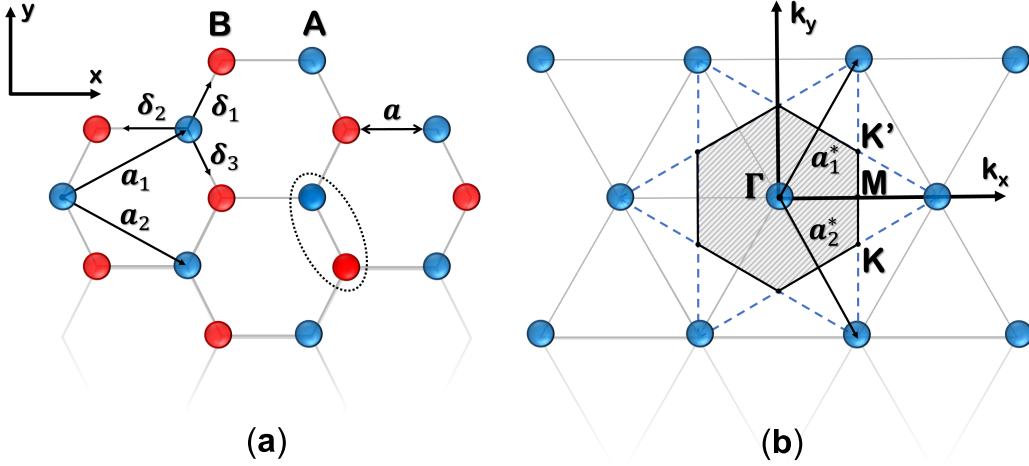


Figure 2.1: (a) Schematic picture of graphene's lattice with the blue (A) and red (B) circles, representing the carbon atoms in different sublattices. a is the lattice spacing. The dotted line around A and B illustrates the unit cell, and the vectors δ_i (with $i = 1, 2, 3$) define the location of A 's nearest-neighbors sites. (b) The Brillouin zone is represented by the shaded region, and at its corners there are two inequivalent points, namely K and K' .

In Fig. 2.1 (b), we draw the reciprocal lattice and define the first Brillouin zone, where two inequivalent points K and K' emerge at the corner,

$$K = \frac{4\pi}{3\sqrt{3}a} (0, 1), \quad K' = \frac{4\pi}{3\sqrt{3}a} (0, -1). \quad (2.1.3)$$

Analogously to the original honeycomb lattice (with A and B atoms), the K and K' points are not connected by any translation operator in the reciprocal lattice, i.e. $\mathbf{T}^* = n_i \mathbf{a}_i^*$.

In order to calculate the electronic band structure of such system, it is also convenient to define three nearest-neighbor vectors of A with respect to B , as shown in Fig. 2.1 (a), namely

$$\delta_1 = \frac{a}{2} (1, \sqrt{3}), \quad \delta_2 = -a (1, 0), \quad \delta_3 = \frac{a}{2} (1, -\sqrt{3}). \quad (2.1.4)$$

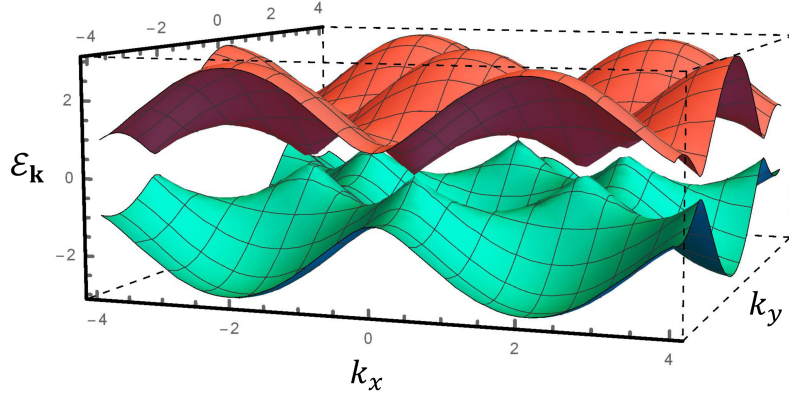


Figure 2.2: Plot of the energy dispersion $\mathcal{E}_{\mathbf{k}}$ given by Eq. (2.1.9), where positive and negative energy bands are represented by different colors. Here, we can see the formation of the six K(K')-points around $\mathcal{E}_{\mathbf{k}} = 0$.

The non-interacting tight-binding Hamiltonian of the lattice depicted in Fig. 2.1 (a), with only nearest-neighbor hopping, is

$$H_{\text{tb}} = -\mathcal{T} \sum_{s=\uparrow,\downarrow} \sum_{\langle i,j \rangle} \left(a_{is}^\dagger b_{js} + b_{js}^\dagger a_{is} \right), \quad (2.1.5)$$

where $\mathcal{T} \cong 3\text{eV}$ [43] is the hopping parameter, and s denotes spins up/down. The operators $a_{is}^\dagger (b_{is}^\dagger)$ and $a_{is} (b_{is})$ correspond to creation and annihilation of electrons, respectively, sitting on the $A(B)$ -sublattices. In the reciprocal space, the Hamiltonian (2.1.5) becomes

$$H_{\text{tb}} = -\mathcal{T} \sum_{s=\uparrow,\downarrow} \sum_{\ell,\mathbf{k}} \left(e^{-i\mathbf{k}\cdot\boldsymbol{\delta}_\ell} a_{\mathbf{k}s}^\dagger b_{\mathbf{k}s} + e^{i\mathbf{k}\cdot\boldsymbol{\delta}_\ell} b_{\mathbf{k}s}^\dagger a_{\mathbf{k}s} \right), \quad (2.1.6)$$

with $\boldsymbol{\delta}_\ell$ given in Eq. (2.1.4) for $\ell = 1, 2, 3$. We can rewrite Eq. (2.1.6) in a matrix form by introducing the spinor $\psi_{\mathbf{k}s}^\dagger = (a_{\mathbf{k}s}^\dagger \ b_{\mathbf{k}s}^\dagger)$,

$$H_{\text{tb}} = \sum_{s=\uparrow,\downarrow} \sum_{\mathbf{k}} \left(a_{\mathbf{k}s}^\dagger \ b_{\mathbf{k}s}^\dagger \right) \begin{pmatrix} 0 & \lambda_{\mathbf{k}} \\ \lambda_{\mathbf{k}}^* & 0 \end{pmatrix} \begin{pmatrix} a_{\mathbf{k}s} \\ b_{\mathbf{k}s} \end{pmatrix} = \sum_s \sum_{\mathbf{k}} \psi_{\mathbf{k}s}^\dagger \mathcal{H}_{\mathbf{k}} \psi_{\mathbf{k}s}, \quad (2.1.7)$$

where

$$\lambda_{\mathbf{k}} = -\mathcal{T} \sum_{\ell=1}^3 e^{-i\mathbf{k}\cdot\boldsymbol{\delta}_\ell} = -\mathcal{T} e^{iak_x} \left[1 + 2e^{-i\frac{3a}{2}k_x} \cos\left(\frac{\sqrt{3}a}{2}k_y\right) \right]. \quad (2.1.8)$$

In this case, it is straightforward to obtain the energy eigenvalues, $\mathcal{E}_{\mathbf{k}} = \pm|\lambda_{\mathbf{k}}|$, thus

$$\mathcal{E}_{\mathbf{k}} = \pm|\mathcal{T}| \left[1 + 4 \cos \left(\frac{\sqrt{3}a}{2} k_y \right) \cos \left(\frac{3a}{2} k_x \right) + 4 \cos^2 \left(\frac{\sqrt{3}a}{2} k_y \right) \right]^{1/2}. \quad (2.1.9)$$

By setting $\mathcal{E}_{\mathbf{k}} = 0$ in Eq. (2.1.9), and considering the region around $k_x = 0$, we find two solutions $k_y = \pm 4\pi/(3\sqrt{3}a)$. Consistently, this result leads us to the K and K' points as in Eq. (2.1.3), also known as valley degrees of freedom.

2.2 Graphene' spinful low-energy theory

To describe the low-energy excitations, we look at the vicinity of the valleys (K, K'), where the momentum \mathbf{k} may be expanded as $\mathbf{k} = \boldsymbol{\kappa} + \mathbf{p}$ (with $\boldsymbol{\kappa} = \mathbf{K}, \mathbf{K}'$). In this way, for small momenta the Hamiltonian density $\mathcal{H}_{\mathbf{k}}$ in Eq. (2.1.7) becomes

$$\mathcal{H}(\mathbf{p}) = \hbar v_F \sum_s \psi^\dagger(\mathbf{p}) (p_x \sigma_y + \tau_v p_y \sigma_x) \psi(\mathbf{p}), \quad (2.2.1)$$

where $v_F = 3a\mathcal{T}/2\hbar \cong 10^6 \text{m/s}$ is the Fermi velocity in graphene, and $\tau_v = \pm 1$ is a valley index (+ for K , - for K'). Furthermore, the wavefunction ψ does not change by a displacement of the valleys, i.e. $\psi_s(\mathbf{p}) = \psi_s(\mathbf{p} + \boldsymbol{\kappa})$.

From now on, we focus on a single valley, and obtain the corresponding Lagrangian density

$$\mathcal{L} = -\hbar \sum_s \bar{\psi}_s(p) (v_F p_j \tilde{\sigma}^j + p_0 \sigma_z) \psi_s(p), \quad (2.2.2)$$

where $\bar{\psi} \equiv \psi^\dagger \sigma_z$, and p_0 (or $-i\partial_t$) corresponds to the frequency-component of the four-momentum vector, which is obtained after a Legendre transformation. Here, the Pauli matrices refer to the sublattice (A, B) structure, with $\tilde{\sigma}^j \equiv i\sigma^j$ (for $j = x, y$). Now, we will include the spin configuration within the theory by increasing the size of the spinor $\psi_{2 \times 2} \rightarrow \Psi_{4 \times 4}$. In this way, we define a $\bar{\Psi} \equiv \Psi^\dagger \sigma_z \otimes s_z \equiv \Psi^\dagger \gamma^0$, where s_z is a Pauli matrix in spin space. By doing so, we find

$$\begin{aligned} \mathcal{L} &= -\hbar \left[\bar{\psi}_\uparrow(p) (v_F p_j \tilde{\sigma}^j + p_0 \sigma_z) \psi_\uparrow(p) + \bar{\psi}_\downarrow(p) (v_F p_j \tilde{\sigma}^j + p_0 \sigma_z) \psi_\downarrow(p) \right] \\ &= -\hbar \bar{\Psi}(p, s) \left[v_F s_z \otimes p_j \tilde{\sigma}^j + p_0 s_z \otimes \sigma_z \right] \Psi(p, s) \\ &= -\hbar \bar{\Psi}(p, s) \gamma^\mu p_\mu \Psi(p, s) \equiv i\hbar \bar{\Psi}(r, s) \gamma^\mu \partial_\mu \Psi(r, s) \end{aligned} \quad (2.2.3)$$

where $p_\mu = (p_0, v_F p_j)$, $\gamma^0 = \text{diag}(\sigma_z, -\sigma_z)$ and $\gamma^j = \text{diag}(\tilde{\sigma}^j, -\tilde{\sigma}^j)$. Eq. (2.2.3) represents a massless 2D Dirac Lagrangian density, where the electrons do not

propagate with the speed of light but with the Fermi velocity. Interestingly, the Dirac mass that would add to the Lagrangian density (2.2.3) as $m\bar{\Psi}\Psi$ actually represents an intrinsic spin-orbit term $m\sigma_z \otimes s_z$ in the Hamiltonian density picture (2.2.1).

Directly from Eq. (2.2.3), we may write down the propagator

$$S_F(p) = \frac{-i}{\gamma^\mu p_\mu}, \quad (2.2.4)$$

the pole of which yields the energy dispersion, $E_\pm(\mathbf{p}) \approx \pm v_F |\mathbf{p}|$, as illustrated in Fig. 2.3.

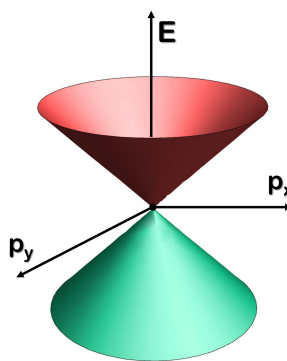


Figure 2.3: Illustration of a Dirac cone. The different colors for positive and negative energies indicate that by setting the chemical potential at $E = 0$, also called half-filling, the system reveals an emergent particle-hole symmetry.

The electron dispersion relation in solid-state materials strongly depends on the crystal-lattice geometry, and we showed that the low-energy limit of graphene's tight-binding model may be mapped into the Dirac theory. By including the effect of spin, we obtained a 4×4 -representation of the theory, which will be useful for the original work in Chapter 4. In the next sections, we will make use of the quantum-field-theory framework to discuss the effect of interactions and external gauge fields in graphene-like materials.

2.3 Remarks on the Dirac theory

It is well-known that the Dirac theory leads to remarkable results, specially when coupled to an external gauge field. Here, we distinguish two situations: the first, when we couple fermions to a constant external magnetic field perpendicular to their plane of propagation; and second, when the gauge field is spacetime dependent. While the first yields the Landau-level spectrum for spin-1/2 particles, the

second may be mapped into the Pauli Hamiltonian in the non-relativistic limit ($m \gg |\mathbf{p}|$, where m is the Dirac mass). In particular, the second shows how single particle interaction effects – such as the spin-orbit coupling – emerge [44]. For later comparison with models beyond the Dirac fermions picture, in this section, we review the Landau-level solution.

We start from the massless 2D Dirac equation minimally coupled to an external gauge field via $\partial_\mu \rightarrow D_\mu = \partial_\mu - i(e/\hbar)A_\mu^{\text{ext}}$,

$$i\hbar \frac{\partial \psi_s(r)}{\partial t} = -i\hbar v_F \sigma^j D_j \psi_s(r), \quad (2.3.1)$$

where we have already set the scalar potential to zero $A_0 = 0$, and j refers to the x, y -components. Because the free Hamiltonian of the system is spin degenerated, we may focus on the effect of the magnetic field in a spin-polarized configuration, i.e. in a 2×2 -matrix representation, as shown in Eq. (2.3.1). In this way, here, the spin is treated just as a flavor, which will be omitted. Now, we fix A_μ^{ext} to be the Landau gauge, $A_\mu^{\text{ext}} = (0, 0, \mathcal{B}x)$, and assume stationary solutions, $\psi(r) = X(\mathbf{r})T(t) = X(\mathbf{r})e^{-iEt}$, where $E > 0$ is the energy eigenvalue. With these considerations, and $X = (X_1 \ X_2)^T$, we find the coupled equations

$$\begin{aligned} -iv_F [\hbar(\partial_x - i\partial_y) - e\mathcal{B}x] X_2 &= EX_1, \\ -iv_F [\hbar(\partial_x + i\partial_y) + e\mathcal{B}x] X_1 &= EX_2. \end{aligned} \quad (2.3.2)$$

From the expressions above, we obtain

$$\begin{aligned} v_F^2 [\hbar^2 (\partial_x^2 + \partial_y^2) - e^2 \mathcal{B}^2 x^2 - \hbar e \mathcal{B} s_z - 2ie\mathcal{B}x\partial_y] X(\mathbf{r}) &= -E^2 X(\mathbf{r}) \\ v_F^2 [\hbar^2 \partial_x^2 - (p_y - e\mathcal{B}x)^2 - \hbar e \mathcal{B} s_z] \tilde{X}(x) &= -E^2 \tilde{X}(x), \end{aligned} \quad (2.3.3)$$

where we used that $X_{1,2}(\mathbf{r}) = e^{ip_y y} \tilde{X}_{1,2}(x)$, $\tilde{X} = (\tilde{X}_1 \ \tilde{X}_2)^T$ and $s_z = \text{diag}(1, -1)$. By changing the variables $x \rightarrow \tilde{x} = \sqrt{e\mathcal{B}/\hbar}[(p_y/e\mathcal{B}) - x]$, we rewrite Eq. (2.3.3) as

$$[\partial_{\tilde{x}}^2 - \tilde{x}^2 - \text{sgn}(e\mathcal{B})s_z] \tilde{X} = -\frac{E^2}{|e\mathcal{B}|\hbar v_F^2} \tilde{X}. \quad (2.3.4)$$

The solutions of the differential Eq. (2.3.4) are identified as the Hermite polynomials, which exist for

$$\frac{E^2 - e\mathcal{B}\hbar v_F^2 s_z}{|e\mathcal{B}|\hbar v_F^2} = \mathcal{N} + 1, \quad (2.3.5)$$

with $\mathcal{N} \in \mathbb{N}$. Here, the sign of the charge e was already fixed by the minimal coupling to represent electrons. In the case of positive charge, one may change $e \rightarrow -e$ in Eq. (2.3.6). The energy eigenvalue in Eq. (2.3.6) has two positive

energy solutions,

$$\begin{aligned} E_+ &= \pm v_F \sqrt{2\hbar|e\mathcal{B}|(\mathcal{N} + 1)}, \\ E_- &= \pm v_F \sqrt{2\hbar|e\mathcal{B}|\mathcal{N}}. \end{aligned} \quad (2.3.6)$$

which depend on the value of the s_z . Naturally, this result indicates that the spin-1/2 configuration is an intrinsic part of the solution. For $\mathcal{N} = 0$, there is a single zero-energy solution (E_-), consequently, the lowest Landau level is associated to a non-degenerated state, while all the other energy levels $\mathcal{N} > 0$ are doubly spin degenerated.

2.4 Electromagnetic interactions in the plane

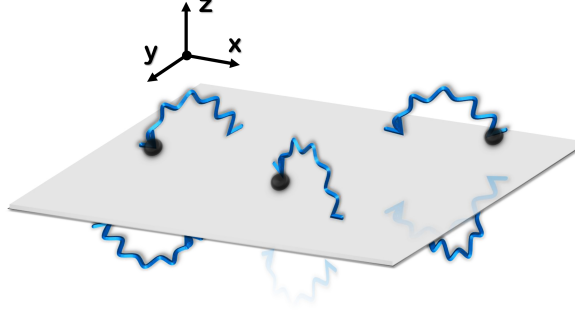


Figure 2.4: Illustration of the dimensional mismatch between electrons (black points), which move in 2D, and photons (blue wavy lines), which propagate in 3D.

In this section, we address the problem of dealing with electromagnetic interactions when there is a *mismatch* between the degrees of freedom of the gauge field and the charge carriers. This issue is illustrated in Fig. 2.4. We review the solution to this question by using the dimensional-reduction procedure performed in Ref. [45] for a 2D Dirac field interacting through an emergent 3D electromagnetic field, which is case of graphene.

We start by writing down the partition function of the system

$$\mathcal{Z} = \int \mathcal{D}\bar{\psi} \int \mathcal{D}\psi \int \mathcal{D}A_\rho \exp\left(\frac{i}{\hbar} S_{\text{QED}}\right), \quad (2.4.1)$$

where

$$S_{\text{QED}}[A_\mu, \bar{\Psi}, \Psi] = i\hbar \int d^3r \bar{\Psi} \gamma^\rho \partial_\rho \Psi - \int d^4r \left(\frac{\varepsilon_0 c}{4} F_{\mu\nu} F^{\mu\nu} + e j_{3+1}^\mu A_\mu \right), \quad (2.4.2)$$

with $d^3r = v_F dx dy dt$ and $d^4r = c dx dy dz dt$, is a QED-like action with broken Lorentz symmetry due to the different velocities. $F_{\mu\nu} \equiv \partial_\mu A_\nu - \partial_\nu A_\mu$ is the field-strength tensor and $j_{3+1}^\mu = \bar{\Psi} \gamma^\mu \Psi$ is the electron current. We may obtain the effective interaction felt by the electrons upon integrating out the gauge field A_μ in Eq. (2.4.1),

$$\mathcal{Z} = \int \mathcal{D}\bar{\psi} \int \mathcal{D}\psi \exp\left(\frac{i}{\hbar} S_{\text{eff}}[\bar{\psi}, \psi]\right), \quad (2.4.3)$$

with $S_{\text{eff}}[\bar{\psi}, \psi] = S_{\text{D}} + S_{\text{int}}$. Here, S_{D} represents the free Dirac action and S_{int} is the resulting current-current interaction after the integration of A_μ , i.e.

$$S_{\text{int}} = -\frac{e^2}{2\varepsilon_0 c} \int d^4r d^4r' j_{3+1}^\mu(r) \frac{1}{(-\square)} j_\mu^{3+1}(r'). \quad (2.4.4)$$

We performed the Wick rotation in Eq. 2.4.4, and \square is the d'Alembertian operator in the Euclidean space. Now, by imposing a constraint on the matter current,

$$j_{3+1}^\mu(t, x, y, z) = j_{2+1}^\rho(t, x, y) \delta(z), \quad (2.4.5)$$

we project the effective interaction in 2D. By inserting Eq. (2.4.5) into Eq. (2.4.4), we find

$$S_{\text{int}} = -\frac{e^2}{2\varepsilon_0 c} \int d^3r d^3r' j_{2+1}^\rho(r) \left[\frac{1}{(-\square)} \right]_\star j_\rho^{2+1}(r'). \quad (2.4.6)$$

The symbol \star indicates that one must compute the effect of the constraint (2.4.5) on the mediator of the interaction, i.e.

$$\left[\frac{1}{(-\square)} \right]_{z=z'=0} = \frac{1}{2} \int \frac{d^3k}{(2\pi)^3} \frac{e^{ik \cdot (r-r')}}{\sqrt{k^2}}. \quad (2.4.7)$$

Eq. (2.4.7) represents the effective interaction between the electron currents on the plane, which in the static limit reduces to the Coulomb interaction

$$\begin{aligned} V_{\text{Coulomb}} &= \frac{1}{2} \int \frac{d^2k}{(2\pi)^2} \frac{e^{i[k_x(x-x') + k_y(y-y')]}{\sqrt{k_x^2 + k_y^2}} \\ &= \frac{1}{2(2\pi)^2} \int_0^\infty k dk \int_0^{2\pi} d\varphi \frac{e^{i|k||r-r'|_{2\text{D}} \cos \varphi}}{\sqrt{k^2}} \\ &= \frac{1}{4\pi|r-r'|_{2\text{D}}}. \end{aligned} \quad (2.4.8)$$

After the dimensional-reduction procedure to find an effective (2+1)D theory for

the interacting electrons, it is convenient to understand what kind of electromagnetic theory generates it. Therefore, by performing a Hubbard-Stratonovich transformation, we introduce a new gauge field A'_ρ in (2+1)D, with the corresponding field-strength tensor $F'^{\rho\tau}$, and find the following action

$$S_{\text{PQED}}[A'_\rho, \bar{\Psi}, \Psi] = i\hbar \int d^3r \bar{\Psi} \gamma^\rho \partial_\rho \Psi - \int d^3r \left(\frac{\varepsilon_0 c}{2} F'_{\rho\tau} \frac{1}{\sqrt{\square}} F'^{\rho\tau} + e j_{2+1}^\rho A'_\rho \right). \quad (2.4.9)$$

Eq. (2.4.9) describes the theory we were looking for. Even though the electrons in graphene are constrained to move on a plane, the electromagnetic field through which they interact spreads in 3D. Integrating away out-of-the-plane photons, we obtained an effective interaction that is non-local in space and time (see Eq. (2.4.7)). In spite of being fully 2D, the pseudo-QED (PQED) action conveys all properties of the genuine 3D electromagnetic interaction. This theory has been called PQED because it involves pseudo-differential operators, but sometimes the name reduced QED is also used in the literature [46, 47]. It has been shown to respect causality [48], scale invariance, the Huygens principle, and unitarity [49], apart from exhibiting an $1/R$ static Coulomb potential. Actually, the propagator in PQED in coordinate space coincides with the one of QED₂₊₁ in momentum space [48], and these two theories are dual to each other [49].

WEAK EXTERNAL MAGNETIC FIELDS IN GRAPHENE-LIKE SYSTEMS

The experimental observation of the renormalization of the Fermi velocity v_F as a function of doping has been a landmark for confirming the importance of electronic interactions in graphene. Although the experiments were performed in the presence of a perpendicular magnetic field \mathcal{B} , the measurements are well described by an RG theory that did not include it. Here we clarify this issue, for both massive and massless Dirac systems, and show that for the weak magnetic fields at which the experiments are performed, there is no change in the RG functions. Our calculations are carried out in the framework of the PQED formalism, which accounts for dynamical interactions. We include only the linear dependence in \mathcal{B} , and solve the problem using two different parametrizations, the Feynman and the Schwinger one. We confirm the results obtained earlier within the RG procedure and show that, within linear order in the magnetic field, the only contribution to the renormalization of the Fermi velocity for the massive case arises due to electronic interactions. In addition, for gapped systems, we observe a running of the mass parameter.

Note: This chapter is based in Ref. [50], where I contributed by performing all the calculations in the work.

3.1 Introduction

The synthesis of graphene [1], a 2D material composed of carbon atoms organized in a honeycomb lattice, had a huge impact in condensed-matter physics. Due to the lattice geometry, this material has two inequivalent Dirac points (K and K'),

each one associated to a valley degree of freedom. In the vicinity of these points, the free electrons exhibit a linear dispersion relation, i.e., $E \propto v_F |\mathbf{k}|$, where v_F is the Fermi velocity, which has a bare value three hundred times smaller than the speed of light.

After graphene, other layered 2D materials with similar properties have been realized, such as silicene [51], stanene [52], germanene [53] and transition metal dichalcogenides (TMDs) [54]. Unlike graphene, which has a gapless spectrum, these other layered materials present an intrinsic bandgap. Silicene, stanene and germanene are semiconductors represented by a single-atom species. Instead of carbon atoms, this other class of materials is composed by heavier atoms (e.g., silicon, germanium). When these atoms with larger ionic radius assemble to form honeycomb structures, the lattices are not flat like graphene, but buckled, which leads to the gap in the spectrum. On the other hand, TMDs consist of layers composed of more than one-atom species. The TMDs layers are weakly bonded by Van der Waals interactions, which permits their treatment as a 2D system. Chemically, the TMDs' composition is represented as MX_2 , where M is the transition-metal atom (Mo, W etc.) and X is the chalcogen atom (Se, S or Te). According to the choice of atoms, these layered materials can exhibit a wide range of physical properties, which includes superconducting, magnetic or topological-insulating behavior, for example. The wide bandgap present in monolayer TMDs is very convenient for electronic applications [54].

For all these materials, the Fermi velocity is an important parameter that characterizes the system. Therefore, a relevant question in the description of the Dirac electrons in these systems is how the Fermi velocity renormalizes due to interactions. Even before the isolation and characterization of graphene, this question was answered through field-theoretical studies that have predicted the effect of interactions in 2D massless Dirac systems, where the electrons and the photons can live in different dimensions [10, 11, 45]. Indeed, both in graphene and related gapped 2D systems, the electrons are constrained to move on a plane, while the mediators of the interaction (photons) can propagate in 3D. Differently from usual QED in (2+1)D, these kind of effective theories generate a Coulomb potential between the electrons proportional to the inverse of the distance, similar to QED in (3+1)D.

An RG study of graphene predicted logarithmic corrections to the Fermi velocity as a function of doping n (or energy) [10–15], which was later observed in many experiments [7–9]. In addition, the renormalized v_F also depends strongly on the dielectric constant ε_G of the medium surrounding the graphene sample, i.e.

$$v_F(n) = v_F(n_0) \left[1 - \frac{\alpha_0}{8\varepsilon_G(n)} \ln \left(\frac{n}{n_0} \right) \right]. \quad (3.1.1)$$

The experimental confirmation of this renormalization called the attention to the role of interactions in graphene and other 2D condensed-matter systems that can be described by relativistic Dirac electrons. Moreover, since the Fermi velocity is the characteristic velocity of the system, all the physical observables carry this information, and this effect is also seen in indirect measurements, e.g., in the quantum capacitance [55] and in the spin g -factor [16, 21]. A theoretical description of the corrections to the g -factor due to interactions can only account for the experimental data upon insertion of the renormalized Fermi velocity and dielectric constant as a function of doping [56].

Although theoretical studies have clarified the role of interactions in renormalizing the Fermi velocity, most of the experiments verifying this behavior are performed in the presence of a magnetic field. The remaining question, to be answered theoretically, is then whether the RG functions are modified or not due to a magnetic field applied perpendicularly to the graphene plane.

A study of the Schwinger-Dyson equations in the *static* limit in the presence of a magnetic field suggests a renormalization of the Fermi velocity in each of the Landau levels due to electron-electron interactions [47]. On the other hand, the experimental findings are well fitted by an RG description that ignores the magnetic field. An important issue in this comparison is the intensity of the magnetic field. Although the calculations in Ref. [47] are made in the “weak” field approximation [57], they cannot describe the experiments detecting the renormalization of the Fermi velocity [7–9] because these experiments are not in the Landau-level, but in the Shubnikov-de Haas regime.

Here, we investigate this problem within the PQED framework, which accounts for *dynamical* interactions, using a field-theoretical method. Since PQED is a renormalizable theory, i.e., the coupling constant is dimensionless, we use perturbation theory up to one-loop order to obtain the first correction to the fermionic propagator due to interactions, and under the presence of a weak external magnetic field. We show that in the weak-field approximation, we may separate the electron self-energy in two pieces: one at zero magnetic field, and another with a linear dependence on the field. Focusing only on the \mathcal{B} -field term, through two different parametrizations, Feynman’s and Schwinger’s, we compute the contribution due to the magnetic field, which happens to be finite. Within the RG equations, we show that neither the weak magnetic field nor any finite contribution modify the renormalization of the Fermi velocity. In addition, for gapped systems we find that the mass renormalizes and its flow depends on the strength of the interaction.

3.2 The model

The particular system of our interest is illustrated in Fig. 3.1. There are electrons propagating with a Fermi velocity v_F in a 2D space, under the influence of an external magnetic field applied perpendicularly to it. Moreover, the photons through which the electrons interact are not confined to the plane, and can propagate in 3D, with the speed c .

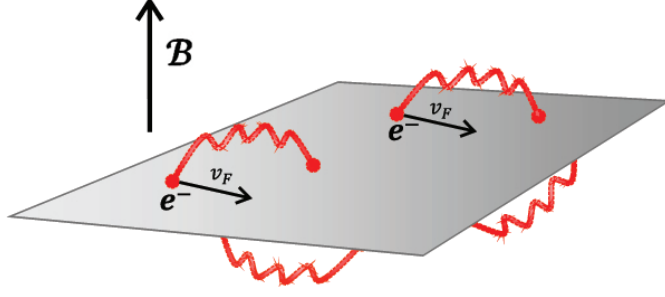


Figure 3.1: Illustrative picture of the system studied.

Mathematically, the dimensional mismatch illustrated above can be described by imposing a constraint in the matter current, and the result – as already shown – is the PQED [45]. The PQED Lagrangian, in the presence of an external magnetic field, is given by

$$\mathcal{L} = -\frac{1}{2} \frac{F_{\mu\nu} F^{\mu\nu}}{\sqrt{\square}} + \bar{\psi} (i\gamma^\mu \bar{\partial}_\mu - m) \psi - e\bar{\psi} \Gamma^\mu \psi A_\mu, \quad (3.2.1)$$

where \square is the d'Alembertian operator, $\gamma^\mu = (\gamma^0, \gamma^i)$, $\bar{\partial}_\mu = (\partial_0, v_F \partial_i)$, $\Gamma^\mu = (\gamma^0, \beta \gamma^i)$, $A_\mu = (A_0, A_i)$, $F_{\mu\nu} = \partial_\mu A_\nu - \partial_\nu A_\mu$, m is the fermionic mass and the dimensionless parameter $\beta = v_F/c$. Now, the minimal coupling is written as a sum of a quantum $A_\mu^{(q)}$ and a classical $A_\mu^{(e)}$ contributions, i.e. $A_\mu = A_\mu^{(q)} + A_\mu^{(e)}$. The first term is the vector potential associated to the quantized dynamical electromagnetic field, which describes the interaction between the photon and the fermion fields, whereas the second is due to the external magnetic field. In this work, we adopt the Landau gauge $A_\mu^{(e)} = (0, 0, \mathcal{B}x)$, with \mathcal{B} denoting a constant magnetic field that couples minimally to the free-fermion momentum to generate the discrete Landau levels.

The Schwinger's proper-time representation of the fermion propagator in (2+1)D in momentum space is [17]

$$S_F(\bar{k}) = \int_0^\infty ds \exp [is (k_0^2 + i\eta_c - m^2) - iv_F^2 \mathbf{k}^2 \ell_B^2 \tan (s|e\mathcal{B}|)] \\ \times [k_0 \gamma^0 - v_F \mathbf{k} \cdot \boldsymbol{\gamma} - m - v_F (k^1 \gamma^2 - k^2 \gamma^1) \tan (s|e\mathcal{B}|)] [1 + \gamma^1 \gamma^2 \tan (s|e\mathcal{B}|)], \quad (3.2.2)$$

where $\bar{k}^\mu = (k_0, v_F \mathbf{k})$ is the electron momentum with $\bar{k}^2 = k_0^2 - v_F^2 \mathbf{k}^2$, the parameter s is the proper time of the particles while they travel throughout their paths in the Feynman diagram [17], η_c is the *causal* factor, and $\ell_B = \sqrt{c(|e\mathcal{B}|)^{-1}}$ is the magnetic length (we assume $\hbar = 1$). The $\gamma^{1,2}$ and the $k^{1,2}$ are the spatial components of the γ -matrices and the momentum, respectively. Here, we neglect finite-density contributions because we are interested in the behavior of the system near the Dirac points. Perturbative calculations taking into account these extra contributions were performed in QED₂₊₁ [58] and QED₃₊₁ [59].

The poles of the fermionic propagator yield the energy dispersion relation $p_0 = \pm E_{\mathcal{N}} = \pm \sqrt{2|e\mathcal{B}|\mathcal{N} + m^2}$, where \mathcal{N} is the quantum number associated with the discrete Landau levels [58]. The photon propagator in the Landau gauge and the interaction vertex are defined, respectively, as

$$G_{\mu\nu}(k) = \frac{-icg_{\mu\nu}}{2\varepsilon\sqrt{k^2}}, \quad (3.2.3)$$

$$\Gamma_0^\mu = -ie(\gamma^0, \beta\gamma^j), \quad (3.2.4)$$

where the photon momentum is $k_\mu = (k_0, c\mathbf{k})$ with $k^2 = k_0^2 - c^2\mathbf{k}^2$.

3.3 Electron self-energy

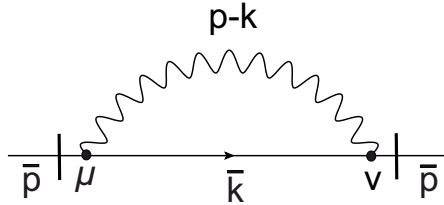


Figure 3.2: Electron self-energy. The bar symbol on top of the momenta is used to denote the electron momentum, which enters with the Fermi velocity v_F , contrarily to the photon propagator, which occurs with the speed of light.

The electron self-energy Σ , represented by the Feynman diagram given in Fig. 3.2, carries the information about the propagation of the electron under the effect of interactions. Therefore, to investigate the possible renormalization of the parameters contained in the Dirac Lagrangian, i.e., the Fermi velocity, the electron mass and the fermionic field itself, one needs to calculate Σ . First, we will analyze the zero-mass case, and then discuss what changes in the presence of the fermionic mass.

3.3.1 The zero-mass case

In one-loop order, the diagram represented in Fig. 3.2 reads

$$\begin{aligned}
\Sigma(\bar{p}) &= i \int \frac{d^3k}{(2\pi)^3} \Gamma_0^\mu S_F(\bar{k}) \Gamma_0^\nu G_{\mu\nu}(p-k) \\
&= -\frac{(1-2\beta^2)ce^2}{2\varepsilon} \int_0^\infty ds \int \frac{d^3k}{(2\pi)^3} \exp \left[is(k_0^2 + i\eta_c) \right. \\
&\quad \left. - iv_F^2 \mathbf{k}^2 \ell_B^2 \tan(s|e\mathcal{B}|) \right] \frac{k_0 \gamma^0 d_1(\mathcal{B}) - v_F \mathbf{k} \cdot \gamma d_2(\mathcal{B})}{\sqrt{(k_0 - p_0)^2 - c^2(\mathbf{k} - \mathbf{p})^2}}, \quad (3.3.1)
\end{aligned}$$

where $d_1(\mathcal{B}) = 1 + \gamma^1 \gamma^2 \tan(s|e\mathcal{B}|)$, and $d_2(\mathcal{B}) = 1 + \tan^2(s|e\mathcal{B}|)$ (for more details of the calculations see Sec. 3.A). Using Schwinger's parametrization,

$$\frac{1}{M^z} = \frac{(-i)^z}{\Gamma(z)} \int_0^\infty d\xi \xi^{z-1} e^{i\xi M}, \quad (3.3.2)$$

we may rewrite the self-energy as

$$\begin{aligned}
\Sigma(\bar{p}) &= -\frac{(1-2\beta^2)ce^2}{2(i\pi)^{1/2}\varepsilon} \int_0^\infty \frac{d\xi}{\xi^{1/2}} \int_0^\infty ds \int \frac{d^3k}{(2\pi)^3} \left[k_0 \gamma^0 d_1 + v_F \mathbf{k} \cdot \gamma d_2 \right] \\
&\quad \times \exp \left[i(s + \xi) \left(k_0 - \frac{\xi p_0}{s + \xi} \right)^2 - iD_B \left(\mathbf{k} - \frac{\xi c^2 \mathbf{p}}{D_B} \right)^2 - \Delta_B \right], \quad (3.3.3)
\end{aligned}$$

where

$$\begin{aligned}
\Delta_B(p_0, \mathbf{p}) &\equiv -i\xi p_0^2 \left(1 - \frac{\xi}{s + \xi} \right) + i\xi c^2 \mathbf{p}^2 \left(1 - \frac{\xi c^2}{D_B} \right), \\
D_B &= v_F^2 \ell_B^2 \tan(s|e\mathcal{B}|) + \xi c^2.
\end{aligned}$$

Shifting the variables in Eq. (3.3.3) as $k_0 \rightarrow k_0 + \xi p_0/(s + \xi)$, $\mathbf{k} \rightarrow \mathbf{k} + \xi c^2 \mathbf{p}/D_B$, and then evaluating the integrals over \mathbf{k} and k_0 (more details in Sec. 3.A), we obtain

$$\Sigma(\bar{p}) = -\frac{i(1-2\beta^2)\alpha\beta}{4\pi} (p_0 \gamma^0 I_1 + v_F \mathbf{p} \cdot \gamma I_2), \quad (3.3.4)$$

where $\alpha = e^2/4\pi\varepsilon v_F$ and the I_i 's are the following parametric integrals:

$$\begin{aligned}
I_1 &= \int_0^\infty d\xi \int_0^\infty ds \frac{\xi^{1/2} d_1(\mathcal{B})}{(s+\xi)^{3/2} [\beta^2 \ell_B^2 \tan(s|e\mathcal{B}|) + \xi]} \times \\
&\exp \left\{ i \frac{s\xi p_0^2}{s+\xi} - i\xi v_F^2 \beta^{-2} \mathbf{p}^2 \left(1 - \frac{\xi}{\beta^2 \ell_B^2 \tan(s|e\mathcal{B}|) + \xi} \right) \right\}, \\
I_2 &= \int_0^\infty d\xi \int_0^\infty ds \frac{\xi^{1/2} d_2(\mathcal{B})}{(s+\xi)^{1/2} [\beta^2 \ell_B^2 \tan(s|e\mathcal{B}|) + \xi]^2} \times \\
&\exp \left\{ i \frac{s\xi p_0^2}{s+\xi} - i\xi v_F^2 \beta^{-2} \mathbf{p}^2 \left(1 - \frac{\xi}{\beta^2 \ell_B^2 \tan(s|e\mathcal{B}|) + \xi} \right) \right\}.
\end{aligned}$$

Until now, we considered the full Landau-levels contribution to the one loop self-energy. Nonetheless, to solve analytically the parametric integrals and proceed with a more intuitive expression for the self-energy, it is necessary to examine some approximations. The first useful one is to consider only terms up to linear order in $\beta = v_F/c$. Since linear terms in β are already of order of $1/300$, second- or higher-order terms would generate negligible contributions that can be discarded. Hence, we have

$$\begin{aligned}
I_1 &\approx \int_0^\infty d\xi \int_0^\infty ds \frac{d_1(\mathcal{B})}{\sqrt{\xi}(s+\xi)^{3/2}} \exp \left[i \frac{s\xi}{\xi+s} p_0^2 - i \frac{v_F^2 \mathbf{p}^2 \tan(s|e\mathcal{B}|)}{|e\mathcal{B}|} \right], \\
I_2 &\approx \int_0^\infty d\xi \int_0^\infty ds \frac{d_2(\mathcal{B})}{\xi^{3/2} \sqrt{s+\xi}} \exp \left[i \frac{s\xi}{\xi+s} p_0^2 - i \frac{v_F^2 \mathbf{p}^2 \tan(s|e\mathcal{B}|)}{|e\mathcal{B}|} \right].
\end{aligned}$$

3.3.2 Weak magnetic field approximation

The second approximation concerns the magnetic field. In the weak-field expansion, one may retain only terms which are up to linear order in the \mathcal{B} -field. In this case, the parametric integrals become

$$I_1 \approx \int_0^\infty d\xi \int_0^\infty ds \frac{\exp \left\{ -\frac{is}{s+\xi} [(s+\xi)v_F^2 \mathbf{p}^2 - p_0^2 \xi] \right\} (1 + \gamma^1 \gamma^2 s |e\mathcal{B}|)}{\sqrt{\xi}(s+\xi)^{3/2}}, \quad (3.3.5)$$

$$I_2 \approx \int_0^\infty d\xi \int_0^\infty ds \frac{\exp \left\{ i \frac{s}{s+\xi} [v_F^2 \mathbf{p}^2 (s+\xi) - p_0^2 \xi] \right\}}{\xi^{3/2} \sqrt{s+\xi}}. \quad (3.3.6)$$

We observe in Eqs. (3.3.5) and (3.3.6) that the linear in \mathcal{B} term gives only an extra contribution to the p_0 component because I_2 does not depend on \mathcal{B} [see also Eq. (3.3.4)]. The remaining integrals are just the effect of interactions, as we expect for zero magnetic field. The same result can be obtained if one starts with

the fermionic propagator already in the weak-field approximation [59], i.e.,

$$S_F(\bar{k}) = \int_0^\infty ds \exp [is (k_0^2 - v_F^2 \mathbf{k}^2)] (k_0 \gamma^0 - v_F \mathbf{k} \cdot \boldsymbol{\gamma} + |e\mathcal{B}| s k_0 \gamma^0 \gamma^1 \gamma^2 + \dots). \quad (3.3.7)$$

Therefore, within these approximations, the additional contribution to the electron self-energy due to the magnetic field can be computed separately. In other words,

$$\Sigma(\bar{p}) = \Sigma^{(0)}(\bar{p}) + \Sigma^{(1)}(\bar{p}) + \dots,$$

where $\Sigma^{(0)}$ is the self-energy in the absence of magnetic field, and the expansion follows with the dependence on the \mathcal{B} -field, as for the propagator in Eq. (3.3.7).

Now, starting from the propagator in the weak-field approximation, and performing the integrals in two different parametrizations in order to double check our results, we find (see Sec. 3.A for details)

1. Feynman parametrization

$$\begin{aligned} -i\Sigma^{(1)}(\bar{p}) &= \frac{i\alpha\beta|e\mathcal{B}|}{4\pi} \int_0^1 dx \frac{p_0 \gamma^0 \gamma^1 \gamma^2}{\sqrt{1-x} [v_F^2 \mathbf{p}^2 - p_0^2 (1-x)]} \\ &= -\frac{i\alpha\beta|e\mathcal{B}|}{2\pi} \frac{\sin^{-1} \left(\sqrt{\frac{p_0^2}{v_F^2 \mathbf{p}^2 - p_0^2}} \right)}{v_F |\mathbf{p}| p_0} p_0 \gamma^0 \gamma^1 \gamma^2, \end{aligned} \quad (3.3.8)$$

2. Schwinger parametrization

$$\begin{aligned} -i\Sigma^{(1)}(\bar{p}) &= \frac{\alpha\beta|e\mathcal{B}|}{4\pi} \int_0^\infty d\xi \int_0^\infty ds \frac{se^{is[p_0^2(\frac{\xi}{s+\xi}) - v_F^2 \mathbf{p}^2]}}{(s+\xi)^{3/2} \xi^{1/2}} p_0 \gamma^0 \gamma^1 \gamma^2 \\ &= -\frac{i\alpha\beta|e\mathcal{B}|}{2\pi} \frac{\coth^{-1} \left(\frac{v_F |\mathbf{p}|}{p_0} \right)}{v_F |\mathbf{p}| p_0} p_0 \gamma^0 \gamma^1 \gamma^2, \end{aligned} \quad (3.3.9)$$

where Eqs. (3.3.8) and (3.3.9) are equivalent. Although the results obtained for the two parametrizations may seem different at first glance, below we plot both trigonometric functions together to show their qualitative behavior, and illustrate that the result is indeed independent of the parametrization scheme in the regime of validity of the theory.

In the y -axis in Fig. 3.3, we represent

$$y(x) = \sin^{-1} \left[(x^2 - 1)^{-1/2} \right],$$

with a black solid line, and

$$y(x) = \coth^{-1}(x),$$

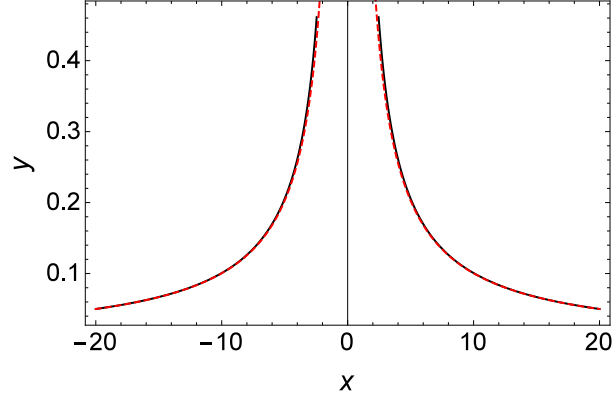


Figure 3.3: Qualitative comparison between the trigonometric functions in Eqs. (3.3.8) and (3.3.9) to show their equivalence. The black solid line represents the inverse of the sine function, and the red dashed line represents the inverse of the cotangent hyperbolic function.

with a red dashed line, for a given value of $x = v_F |\mathbf{p}| / |p_0|$. Both trigonometric functions are only valid for $\text{Re} [|x|] \geq 1$.

These results show that in linear order the magnetic field gives a finite contribution to the electron self-energy. Although this result suggests that the magnetic field will not modify the flow of the Fermi velocity, in the next section we explicitly calculate the RG equations to show that this is indeed the case.

3.3.3 The fermionic mass contribution

Now, we will examine what effectively happens in the study of the self-energy for the massive case. The expansion of the propagator given in Eq. (3.2.2) up to linear order in the magnetic field yields

$$S_F^{(0)}(\bar{k}) = i \frac{k_0 \gamma^0 - v_F \mathbf{k} \cdot \boldsymbol{\gamma} + m}{k_0^2 - v_F^2 \mathbf{k}^2 - m^2}, \quad (3.3.10)$$

and

$$S_F^{(1)}(\bar{k}) = -|e\mathcal{B}| \frac{k_0 \gamma^0 + m}{[k_0^2 - v_F^2 \mathbf{k}^2 - m^2]^2} \gamma^1 \gamma^2. \quad (3.3.11)$$

As we have seen already for the massless case, the linear contributions on the magnetic field appeared to be finite and do not affect the RG functions. Therefore, here we will focus on the mass term of Eq. (3.3.10) because this will give us the divergent contribution that will affect the mass renormalization.

Following a standart procedure, we find

$$-i\Sigma^{(0)}(m) = -\frac{\alpha\beta}{2\pi\epsilon} (1 + 2\beta^2) m I_3, \quad (3.3.12)$$

where $\epsilon \rightarrow 0$ and

$$I_3 = \frac{1}{c^2} \int_0^1 dx \frac{x^{-1/2}}{[\beta^2(x-1) - x]}. \quad (3.3.13)$$

3.4 Renormalization group study

In order to use the RG functions, first we need to define the expression for the inverse of the free-fermion propagator in the presence of the magnetic field. This turns out not to be a problem because the information about the \mathcal{B} -field is contained within the Schwinger's phase factor [17] and the inverse of the propagator happens to be the same as in the case of zero \mathcal{B} -field [59, 60]. Based on this statement, we can start from the propagator as in Eq. (3.2.2), without any approximations, and obtain an expression for the self-energy with all the possible contributions coming from the magnetic field. Hence, the case of a weak magnetic field would only be considered in the approximation for the self-energy.

The RG equation is given by

$$\left(\mu \frac{\partial}{\partial \mu} + \beta_e \frac{\partial}{\partial e} + \beta_{v_F} \frac{\partial}{\partial v_F} + \beta_c \frac{\partial}{\partial c} + \gamma_m m \frac{\partial}{\partial m} - N_F \gamma_\psi - N_A \gamma_A \right) \Gamma^{(N_F, N_A)} = 0, \quad (3.4.1)$$

where $\Gamma^{(N_F, N_A)}$ represent the vertex functions, with N_F and N_A the number of fermion and photon external lines, respectively, in the Feynman diagrams. The functions γ_ψ and γ_A are the respective anomalous dimension of the fermion and photon fields, $m\gamma_m = \mu \partial m / \partial \mu$ is a dimensionless function for the mass, and β_i ($i = e, v_F, c$) are the beta-functions associated to the parameters of the PQED Lagrangian. We use dimensional regularization to obtain the vertex functions in Eq. (3.4.1).

In the case of the fermion two-point function, we have

$$\left(\mu \frac{\partial}{\partial \mu} + \beta_e \frac{\partial}{\partial e} + \beta_{v_F} \frac{\partial}{\partial v_F} + \beta_c \frac{\partial}{\partial c} + \gamma_m m \frac{\partial}{\partial m} - 2\gamma_\psi \right) \Gamma^{(2,0)} = 0, \quad (3.4.2)$$

with

$$\Gamma^{(2,0)} = -i (\gamma^0 p_0 + v_F \gamma^i p_i + m) - i\Sigma. \quad (3.4.3)$$

Here, we write the self-energy Σ in a general form, where all the possible contributions of an external magnetic field could be included.

According to our approximation $\Sigma \approx \Sigma^{(0)} + \Sigma^{(1)}$, the self-energy can then be written as

$$-i\Sigma = e^2 \left(\text{finite}^{(2,0)} + \ln \mu \text{Res}^{(2,0)} \right) + e^3 f(\mathcal{B}), \quad (3.4.4)$$

where we divide the zero magnetic field part into a finite and a divergent contribution, with

$$\text{Res}^{(2,0)} = \mathcal{W}_1 \gamma^0 p_0 + \mathcal{W}_2 \gamma^i p_i + \mathcal{W}_3 m, \quad (3.4.5)$$

representing the pole term proportional to $1/\epsilon$. For the RG purposes, here, the explicit form of the $\text{finite}^{(2,0)}$ contribution is irrelevant. The coefficients \mathcal{W}_1 and \mathcal{W}_2 are determined using Eq. (3.3.4) for $\mathcal{B} = 0$, whereas \mathcal{W}_3 is determined from Eq. (3.3.12), and the function $f(\mathcal{B})$ is the finite result obtained from Eq. (3.3.8) or (3.3.9).

3.4.1 Velocity renormalization

Now, expanding each of the parameters in Eq. (3.4.2) in terms of the coupling constant e , e.g.,

$$\beta_{v_F} = \beta_{v_F}^{(1)} e + \beta_{v_F}^{(2)} e^2 + \beta_{v_F}^{(3)} e^3 + \dots,$$

going up to third order, and applying Eq. (3.4.2), we find that $\gamma_\psi^{(1)} = \beta_{v_F}^{(1)} = 0$. Moreover, performing the same analysis for the other two vertex functions, $\Gamma^{(2,1)}$ and $\Gamma^{(0,2)}$, we find that $\gamma_A^{(1)} = \beta_c^{(1)} = \beta_e^{(1)} = 0$ (for more details of the calculations see Sec. 3.B). In second order in the coupling constant, for $\beta_{v_F}^{(2)}$, we obtain the well-known renormalization of the Fermi velocity solely due to interaction effects [10, 11]. This is expected because the magnetic-field term enters in Eq. (3.4.4) as e^3 , hence, the only possible contribution should be seen in this order of the coupling constant. At third order in e , we observe that the corrections to $\beta_{v_F}^{(3)}$, depending on the finite part of the self-energy, would appear for $\beta_e^{(2)} \neq 0$. However, $\beta_e^{(2)} \propto \gamma_A^{(1)}$, and as the photon self-energy has no divergences in one-loop order, using dimensional regularization, its anomalous dimension is null ($\gamma_A^{(1)} = \gamma_A^{(2)} = 0$). Thus, $\beta_{v_F}^{(3)} = 0$, and no additional renormalization term is generated due to the presence of an external magnetic field.

The fact that only the $\mathcal{B} = 0$ term in Eq. (3.2.2) contributes to the renormalization of the parameters in the Lagrangian (3.2.1) may suggest that the distinction between weak- or strong-field limit is irrelevant. However, the weak- or strong-field case is determined by the comparison between the two length scales in the theory, namely the magnetic length $\ell_B \propto \mathcal{B}^{-1/2}$ and doping $\ell_n \propto n^{-1/2}$. The RG flow is

suppressed and stops at the largest length (or smallest energy) scale; hence, at the critical point ($n \approx 0$) the doping energy is the one that determines the cutoff.

3.4.2 The running mass

The second-order expansion in the coupling constant yields the mass function

$$\begin{aligned}\gamma_m^{(2)} &= -i(\mathcal{W}_3 + \mathcal{W}_1) = -\frac{e^2}{8\pi^2 c\varepsilon} \int_0^1 dx \frac{x^{1/2}(1 - 2\beta^2) + x^{-1/2}(1 + 2\beta^2)}{\beta^2(x - 1) - x} \\ &= -\frac{\alpha}{2\pi} F(\beta),\end{aligned}\tag{3.4.6}$$

where

$$F(\beta) = 2 \frac{(1 - \beta^2 + \beta^4) \text{ArcTan} [(-1 + \beta^{-2})^{1/2}]}{(-1 + \beta^{-2})^{1/2}(-\beta + \beta^3)} + 2 \frac{(\beta^2 - 2\beta^4)}{(-\beta + \beta^3)}.$$

Now, calculating Eq. (3.4.6) on the fixed point of the theory ($\beta = 1$), we obtain

$$\lim_{\beta \rightarrow 1} \gamma_m^{(2)} = \frac{5\alpha}{3\pi}.\tag{3.4.7}$$

The mass parameter runs as

$$\frac{\partial \ln m(\mu)}{\partial \ln(\mu/\mu_0)} = \gamma_m^{(2)}(\beta),\tag{3.4.8}$$

and integrating Eq. (3.4.8), we obtain

$$m(\mu) = m_0 \left(\frac{\mu}{\mu_0} \right)^{\gamma_m^{(2)}} \approx m_0 \left(\frac{\mu}{\mu_0} \right)^{5\alpha/3\pi},\tag{3.4.9}$$

with $m_0 = m(\mu_0)$. We see from Eq. (3.4.7) that $\gamma_m^{(2)}$ has a positive sign and depends on α .

These are the two main results of this chapter: first, the magnetic field does not renormalize any of the parameters of the Lagrangian (3.2.1), and second, the interaction defines how fast the mass parameter runs. Furthermore, as expected, the mass parameter cures infrared divergences that may arise due to the \mathcal{B} -field expansion.

3.5 Conclusions

Motivated by the fact that most of the experiments of the Fermi velocity renormalization in graphene are performed in the presence of a weak external magnetic field [7–9], whereas the field-theoretical models either ignore the latter [10, 11] or study the problem in the (strong field) Landau-level regime [47], we decided to revise the topic.

Our starting point is the PQED formalism, which accounts for dynamical interactions, under the presence of a weak perpendicular magnetic field. The magnetic field contribution to the self-energy was obtained using two different but equivalent parametrization schemes. The analysis of the RG shows that a weak magnetic field has no additional effect in the renormalization of the Fermi velocity, within linear order in \mathcal{B} . In this particular theory, because the photon field has null anomalous dimension, up to third-order in the coupling constant e , no finite contributions coming from the electron self-energy can modify this renormalization. Hence, in this approximation, it is sufficient to consider only the effect of interactions to observe how the velocity changes with respect to the energy scale of the theory.

It has been observed in Ref. [55], through measurements of quantum capacitance, that the Fermi velocity displays the same indistinguishable logarithmic renormalized behavior as a function of doping both in the absence or in the presence of a weak magnetic field. Our results confirm that, from a theoretical perspective, this should be indeed the case.

A simple analysis of the perturbation theory shows that our results hold also for high-order loops due to the fact that the theory is renormalizable. Therefore, in the weak-field expansion, any contribution depending on the magnetic field \mathcal{B} would generate additional finite terms to the electron self-energy, which do not change the RG functions. This result does not depend on the massive or massless nature of the system.

In massive systems, however, we obtain a renormalization of the mass parameter, the flow of which depends on the strength of the interaction α . This renormalization effect is solely due to the electron-electron interaction.

Even though the weak magnetic field has no effect in the RG functions, finite temperatures could affect this renormalization [61, 62]. In addition, for stronger magnetic fields, it was shown theoretically using the Schwinger-Dyson equations that within the static approximation the interactions renormalize the Fermi velocity with a factor that depends on the Landau-level index [47]. The generalization of this theory to the dynamical case and stronger magnetic fields, however, remains to be done. We hope that our results will stimulate measurements of the

renormalization of the Fermi velocity in massive Dirac systems, analogously to experiments performed in graphene.

3.A Details of the Self-energy calculations

Fermionic propagator

Before introducing the fermionic propagator of Eq. (3.2.2) with $m = 0$ in the expression for the self-energy, as shown in Eq. (3.3.1), we combine the γ -matrices in a compact way,

$$\begin{aligned}
\mathcal{F}_N(\bar{k}) &= [k_0\gamma^0 - v_F\mathbf{k} \cdot \boldsymbol{\gamma} - v_F(k^1\gamma^2 - k^2\gamma^1) \tan(s|e\mathcal{B}|)] [1 + \gamma^1\gamma^2 \tan(s|e\mathcal{B}|)] \\
&= k_0\gamma^0 [1 + \gamma^1\gamma^2 \tan(s|e\mathcal{B}|)] - v_F\mathbf{k} \cdot \boldsymbol{\gamma} [1 + \gamma^1\gamma^2 \tan(s|e\mathcal{B}|)] \\
&\quad - v_F(k^1\gamma^2 - k^2\gamma^1) \tan(s|e\mathcal{B}|) [1 + \gamma^1\gamma^2 \tan(s|e\mathcal{B}|)] \\
&= k_0\gamma^0 d_1(\mathcal{B}) - v_F\mathbf{k} \cdot \boldsymbol{\gamma} - v_F(k^1\gamma^2 - k^2\gamma^1) \tan(s|e\mathcal{B}|) \\
&\quad - v_F(\gamma^1 k^1 + \gamma^2 k^2) \gamma^1 \gamma^2 \tan(s|e\mathcal{B}|) - v_F(k^1\gamma^2 - k^2\gamma^1) \gamma^1 \gamma^2 \tan^2(s|e\mathcal{B}|) \\
&= k_0\gamma^0 d_1(\mathcal{B}) - v_F\mathbf{k} \cdot \boldsymbol{\gamma} d_2(\mathcal{B}),
\end{aligned}$$

where we use that $\gamma^1\gamma^2 = -\gamma^2\gamma^1$, $(\gamma^i)^2 = -1$, and $\mathcal{F}_N(\bar{k})$ is the term that multiplies the exponential in the integrand of Eq. (3.2.2), i.e.,

$$S_F(\bar{k}) = \int_0^\infty ds \mathcal{F}_N(\bar{k}) \exp [is(k_0^2 + i\epsilon) - iv_F^2 \mathbf{k}^2 \ell_B^2 \tan(s|e\mathcal{B}|)].$$

Integrals over the loop-momentum k

The integrals over k in Sec. 3.3, after the shift of the variables as

$$k_0 \rightarrow k_0 + \frac{\xi p_0}{s + \xi}, \quad \text{and} \quad \mathbf{k} \rightarrow \mathbf{k} + \frac{\xi c^2 \mathbf{p}}{D_B},$$

are given by

$$\int_{-\infty}^{\infty} dk_0 (\mathcal{G}_1 \gamma^0 k_0 + \mathcal{G}_2) \exp [i(s + \xi)k_0^2] = \frac{\pi^{1/2} \mathcal{G}_2}{(-i)^{1/2} (s + \xi)},$$

and

$$\int_{-\infty}^{\infty} \int_{-\infty}^{\infty} dk_1 dk_2 (\mathcal{G}_3 + \mathcal{G}_4 \gamma^1 k^1 + \mathcal{G}_5 \gamma^2 k^2) \exp [-iD_B(k_1^2 + k_2^2)] = \frac{i\pi \mathcal{G}_3}{D_B},$$

where

$$\begin{aligned}\mathcal{G}_1 &= d_1(\mathcal{B}), & \mathcal{G}_4 &= \mathcal{G}_5 = v_F d_2(\mathcal{B}), \\ \mathcal{G}_3 &= \gamma^0 p_0 \frac{\xi}{\xi + s} d_1(\mathcal{B}) + v_F \mathbf{p} \cdot \gamma \frac{\xi c^2}{D_{\mathcal{B}}} d_2(\mathcal{B}), \\ \mathcal{G}_2 &= \mathcal{G}_3 + v_F \mathbf{k} \cdot \gamma d_2(\mathcal{B}).\end{aligned}$$

Weak-field limit calculations

In the weak-field approximation, after integrating the linear contribution in the magnetic field in Eq. (3.3.7), we obtain

$$S_F^{(1)}(\bar{k}) = -|e\mathcal{B}| \frac{k_0 \gamma^0 \gamma^1 \gamma^2}{(k_0^2 - v_F^2 \mathbf{k}^2)^2}, \quad (3.A.1)$$

and the B -field term in the self-energy reads

$$\begin{aligned}-i\Sigma^{(1)}(\bar{p}) &= \int \frac{d^D k}{(2\pi)^D} \Gamma_0^\mu S_F^{(1)}(\bar{p} - \bar{k}) \Gamma_0^\nu G_{\mu\nu}(k) \\ &= -\frac{ice^2 |e\mathcal{B}|}{2\varepsilon} \int \frac{d^3 k}{(2\pi)^3} \frac{(1 + 2\beta^2)(p_0 - k_0) \gamma^0 \gamma^1 \gamma^2}{[(p_0 - k_0)^2 - v_F^2 (\mathbf{p} - \mathbf{k})^2]^2 \sqrt{k_0^2 - c^2 \mathbf{k}^2}},\end{aligned} \quad (3.A.2)$$

where we used the properties of the γ -matrices, e.g., $\{\gamma^\mu, \gamma^\nu\} = 2g^{\mu\nu}$, and $d^3 k = dk_0 d^2 \mathbf{k}$.

Now, to calculate the integrals over the loop momentum k in Eq. (3.A.2), we define which one of the two parametrizations (Feynman's or Schwinger's) will be used. Here, we use Schwinger's parameterization as in Eq. (3.3.2). Nevertheless, if one chooses to use Feynman's parameters, like

$$\frac{1}{D_1^2 D_2^{1/2}} = \frac{3}{4} \int_0^1 dx \frac{x(1-x)^{-1/2}}{[D_1 x + (1-x)D_2]^{5/2}},$$

the same result is obtained. As we have shown in Sec. 3.3, the result should not depend on this choice.

Hence, plugging Schwinger's parameters in Eq. (3.A.2), we find

$$\begin{aligned}-i\Sigma^{(1)}(\bar{p}) &= \frac{i^{5/2} ce^2 |e\mathcal{B}| (1 + 2\beta^2)}{2\varepsilon \pi^{1/2} (2\pi)^3} \int_0^\infty d\xi \xi \int_0^\infty d\eta \eta^{-1/2} \\ &\times \int d^3 k \exp \left\{ i \left[\xi (p_0 - k_0)^2 - \xi v_F^2 (\mathbf{p} - \mathbf{k})^2 + \eta (k_0^2 - c^2 \mathbf{k}^2) \right] \right\} (p_0 - k_0) \gamma^0 \gamma^1 \gamma^2.\end{aligned}$$

The integrals over k are *Gaussian*, and to solve them we first introduce a regulator Λ^2 to avoid high-energy momentum contributions, e.g., $\exp(-k^2\Lambda^{-2})$. Then, we combine separately the terms proportional to k_0 and \mathbf{k} to complete the square for each of them as in Eq. (3.3.3). The integrals over k yield

$$\begin{aligned} I_k &= \int dk_0 \exp [i(\xi + \eta + i\Lambda^{-2})k_0^2] \int d^2\mathbf{k} \exp [-i(v_F^2\xi + c^2\eta + i\Lambda^{-2})\mathbf{k}^2] \\ &= \frac{\pi^{3/2}}{i^{5/2}c^2(\eta + \xi)^{1/2}(\eta + \beta^2\xi)}, \end{aligned} \quad (3.A.3)$$

where the limit of $\Lambda \rightarrow \infty$ was taken after the integration.

Therefore,

$$\begin{aligned} -i\Sigma^{(1)}(\bar{p}) &= \frac{e^2|e\mathcal{B}|(1 + 2\beta^2)p_0\gamma^0\gamma^1\gamma^2}{16\pi^2\epsilon c} \\ &\times \int_0^\infty d\xi \int_0^\infty d\eta \frac{\xi\eta^{1/2} \exp \left\{ i \left[p_0^2 \left(\frac{\eta\xi}{\eta+\xi} \right) - v_F^2 \mathbf{p}^2 \left(\frac{\eta\xi}{\eta+\beta^2\xi} \right) \right] \right\}}{(\eta + \xi)^{3/2}(\eta + \beta^2\xi)}, \end{aligned}$$

and for $\beta^2 \rightarrow 0$, we obtain the result given in Eq. (3.3.9).

3.B Renormalization-group calculations

Here, we show more details of the calculations concerning the RG equations. As usual, the scaling parameter μ is introduced through $\mu^{\epsilon/2}$, where ϵ will be taken to zero in the end. Hence, applying Eq. (3.4.3) in Eq. (3.4.2), with Σ given by Eq. (3.4.4), we find the following partial derivatives

$$\begin{aligned} \mu \frac{\partial \Gamma^{(2,0)}}{\partial \mu} &= e^2 \text{Res}^{(2,0)}, \\ \beta_e \frac{\partial \Gamma^{(2,0)}}{\partial e} &= \beta_e \left[2e \left(\tilde{f} + \ln \mu \tilde{R} \right) + 3e^2 f_{\mathcal{B}} \right], \\ \beta_c \frac{\partial \Gamma^{(2,0)}}{\partial c} &= \beta_c \left[e^2 \left(\frac{\partial \tilde{f}}{\partial c} + \ln \mu \frac{\partial \tilde{R}}{\partial c} \right) + e^3 \frac{\partial f_{\mathcal{B}}}{\partial c} \right], \\ \beta_{v_F} \frac{\partial \Gamma^{(2,0)}}{\partial v_F} &= \beta_{v_F} \left[e^2 \left(\frac{\partial \tilde{f}}{\partial v_F} + \ln \mu \frac{\partial \tilde{R}}{\partial v_F} \right) + e^3 \frac{\partial f_{\mathcal{B}}}{\partial v_F} \right] - i\beta_{v_F} \gamma^i p_i, \end{aligned}$$

where \tilde{f} and \tilde{R} stand for finite^(2,0) and Res^(2,0), respectively, and $f(\mathcal{B}) = f_{\mathcal{B}}$. Hence, Eq. (3.4.2) becomes

$$\begin{aligned} e^2 \tilde{R} + \beta_e \left[2e \left(\tilde{f} + \ln \mu \tilde{R} \right) + 3e^2 f_{\mathcal{B}} \right] + \beta_c e^3 \partial_c f_{\mathcal{B}} + \beta_c e^2 \left(\partial_c \tilde{f} + \ln \mu \partial_c \tilde{R} \right) \\ + \beta_{v_F} e^2 \left(\partial_{v_F} \tilde{f} + \ln \mu \partial_{v_F} \tilde{R} \right) + \beta_{v_F} e^3 \partial_{v_F} f_{\mathcal{B}} - i \beta_{v_F} \gamma^l p_l - 2\gamma_\psi \left[-i \left(\gamma^0 p_0 + v_F \gamma^l p_l \right) \right. \\ \left. + e^2 \left(\tilde{f} + \ln \mu \tilde{R} \right) + e^3 f_{\mathcal{B}} \right] = 0, \end{aligned} \quad (3.B.1)$$

where ∂_j is a partial derivative with respect of one of the parameters $j = c, v_F, e$. We expand each of the β_j -functions and γ_ψ in terms of e up to third-order, e.g.,

$$\beta_{v_F} = \beta_{v_F}^{(1)} e + \beta_{v_F}^{(2)} e^2 + \beta_{v_F}^{(3)} e^3 + \dots,$$

and we unite the elements that share the same dependence on the coupling constant e . In this manner, we obtain three equations, one for each different order in e .

a. Order of e

$$\begin{aligned} -i \gamma^l p_l \beta_{v_F}^{(1)} + 2i \gamma_\psi^{(1)} (\gamma^0 p_0 + v_F \gamma^l p_l) = 0, \\ \therefore \quad \gamma_\psi^{(1)} = 0, \text{ and } \beta_{v_F}^{(1)} = 0. \end{aligned}$$

b. Order of e^2

$$\begin{aligned} \tilde{R} - i \gamma^l p_l \beta_{v_F}^{(2)} + 2i \gamma_\psi^{(2)} (\gamma^0 p_0 + v_F \gamma^l p_l) = 0, \\ \gamma^l p_l \left[\mathcal{W}_2 - i \beta_{v_F}^{(2)} + 2i v_F \gamma_\psi^{(2)} \right] + \gamma^0 p_0 \left[\mathcal{W}_1 + 2i \gamma_\psi^{(2)} \right] = 0, \\ \therefore \quad \beta_{v_F}^{(2)} = -i (\mathcal{W}_2 - v_F \mathcal{W}_1) \quad \text{and} \quad \gamma_\psi^{(2)} = \frac{i}{2} \mathcal{W}_1. \end{aligned}$$

Here, we replaced \tilde{R} as in Eq. (3.4.5), and we used that $\beta_e^{(1)} = 0$, which can be obtained by doing the same procedure for the other two Γ -functions, i.e, $\Gamma^{(0,2)}$ and $\Gamma^{(2,1)}$. Note that \tilde{R} only contains the divergent part of the electron self-energy. In other words, it is sufficient to compute $\Sigma^{(0)}$ to find $\beta_{v_F}^{(2)}$, which is precisely the function associated to the renormalization of the Fermi velocity. This is a second-order effect in the coupling constant e , and the magnetic field neither adds an extra term, nor changes this renormalization. Moreover, within the renormalization-group scheme seen in Eq. (3.4.1), no finite contributions are encountered in this renormalization.

c. Order of e^3

$$2\beta_e^{(2)} \left(\tilde{f} + \ln \mu \tilde{R} \right) - i \beta_{v_F}^{(3)} \gamma^l p_l + 2i \gamma_\psi^{(3)} (\gamma^0 p_0 + v_F \gamma^l p_l) = 0,$$

where we used the results $\beta_j^{(1)} = \gamma_\psi^{(1)} = 0$. The magnetic field finite contribution would only be possible if $\beta_e^{(1)} \neq 0$. However, as the polarization tensor is finite in one-loop order, using dimensional regularization, its anomalous dimension is null, $\gamma_A^{(1)} = \gamma_A^{(2)} = 0$, and this implies that both $\beta_e^{(1)}$ and $\beta_e^{(2)}$ are zero. Since $\gamma_\psi^{(3)} = 0$, then $\beta_{v_F}^{(3)} = 0$. Therefore, neither the linear magnetic field nor the other finite contributions change the Fermi-velocity renormalization.

ON THE SPIN GYROMAGNETIC FACTOR IN GRAPHENE

The gyromagnetic factor is an important physical quantity relating the magnetic-dipole moment of a particle to its spin. The electron spin g -factor *in vacuo* is one of the best model-based theoretical predictions ever made, showing agreement with the measured value up to ten parts per trillion [17–20]. However, for electrons in a material the g -factor is modified with respect to its value *in vacuo* because of environment interactions. In this chapter, we show how interaction effects lead to a spin g -factor correction in graphene by considering the full electromagnetic interaction in the framework of PQED [45, 63–66]. We compare our theoretical prediction with experiments performed in graphene deposited on SiO₂ and SiC substrates, and find a very good agreement between them.

Note: This chapter is based in Ref. [56], where I contributed by performing all the calculations in the work.

4.1 Introduction

We have seen that both the measurement of the FQHE [4–6] and the experimental observation of the renormalization of the Fermi velocity [7–9] settled the importance of electron-electron interaction in graphene. In particular, we have shown in Chapter 3 that the reshaping of the Fermi velocity theoretically predicted in Refs. [10–15] does not change in the presence of weak magnetic fields.

Now, motivated by the relevance of electron-electron interactions in graphene, and by the fact that the Fermi velocity is much different than the speed of light

$v_F \ll c^1$, we investigate in this chapter the spin gyromagnetic factor in graphene. Within the *anisotropic* PQED framework, which contains a term that breaks Lorentz invariance in the quantum-field-theory formalism, we start by discussing how interaction effects may lead to corrections to the bare g -factor $g_s = 2$. We then calculate this correction and show that the enhanced g_s compares very well to the experimental data available in the literature [16, 21]. Our results set the importance of interactions in determining the g -factor in graphene in particular, and 2D relativistic condensed-matter systems in general.

4.2 Anisotropic pseudo-QED

The anisotropic version of the PQED is given by the Lagrangian

$$\begin{aligned} \mathcal{L} = & -\frac{1}{2}F_{\mu\nu}\frac{1}{\sqrt{\square}}F^{\mu\nu} + \bar{\psi}_\kappa(i\gamma^0\partial_0 + iv_F\gamma^i\partial_i - \Delta)\psi_\kappa - e\bar{\psi}_\kappa\left(\gamma^0A_0 + \frac{v_F}{c}\gamma^iA_i\right)\psi_\kappa \\ & + \frac{\zeta}{2}A_\mu\frac{\partial^\mu\partial^\nu}{\sqrt{\square}}A_\nu, \end{aligned} \quad (4.2.1)$$

where $F^{\mu\nu}$ is the usual field-intensity tensor of the U(1) gauge field A_μ , which intermediates the electromagnetic interaction in 2D (pseudo electromagnetic field), \square is the d'Alembertian, and $\bar{\psi}_\kappa = \psi_\kappa^\dagger\gamma^0$ is the Dirac spinor, with κ representing a sum over valleys (K and K'). Here, we use the Dirac basis for the γ -matrices and consider a 4×4 -spinor representation $\psi_\kappa^\dagger = (\psi_{A\downarrow}^*, \psi_{B\downarrow}^*, \psi_{A\uparrow}^*, \psi_{B\uparrow}^*)_\kappa$, with A and B denoting the sublattices in graphene and \uparrow, \downarrow the different spins. The parameter ζ is the gauge fixing (we adopt Feynman's gauge $\zeta = 1$), and Δ is a gap that may occur due to a sublattice asymmetry in case of graphene deposited on substrates (which also acts as an infrared regularization parameter) [68].

The Feynman's rules of the model yield the fermion propagator S_F ,

$$S_F(\bar{p}) = i\frac{\gamma^\mu\bar{p}_\mu + \Delta}{\bar{p}^2 - \Delta^2}, \quad (4.2.2)$$

where $\gamma^\mu = (\gamma^0, \gamma^i)$ are Dirac matrices, $\bar{p}^\mu = (p_0, v_F\mathbf{p})$ and $\bar{p}^2 = p_0^2 - v_F^2\mathbf{p}^2$. The photon propagator reads

$$G_{\mu\nu}(p) = \frac{-ic}{2\varepsilon\sqrt{p^2}}\left[g_{\mu\nu} - \left(1 - \frac{1}{\zeta}\right)\frac{p_\mu p_\nu}{p^2}\right], \quad (4.2.3)$$

¹Most of the theories found in the literature consider only static interactions because $v_F \ll c$. Dynamical effects, nevertheless, have proven to be important in some cases, by generating novel quantum topological states that would not arise in the static limit [67].

where p_μ is the four-momentum given by $p_\mu = (p_0, c\mathbf{p})$, with $p^2 = p_0^2 - c^2\mathbf{p}^2$. The interaction vertex is given by

$$\Gamma_0^\mu = -ie (\gamma^0, \beta \gamma^j), \quad (4.2.4)$$

where $\beta \equiv v_F/c$. The pole of the fermion propagator provides the energy dispersion relation $p_0 = E(\mathbf{p}) = \pm\sqrt{v_F^2\mathbf{p}^2 + \Delta^2}$. When $\Delta = 0$, we reproduce the tight-binding result for monolayer graphene.

The first term present in the Maxwell Lagrangian in Eq. (4.2.1) is non-local and renders the canonical dimension of the gauge field equal to one, in units of mass. The same holds for the Dirac field. Therefore, the coupling constant e is dimensionless in (2+1)D, and the theory is renormalizable, analogously to QED₃₊₁. Here, we will calculate the one-loop correction to the vertex diagram using the dimensional regularization procedure as a way to obtain finite Feynman amplitudes, which do not depend on the regulator [69, 70].

4.3 The electron (2+1)D vertex function

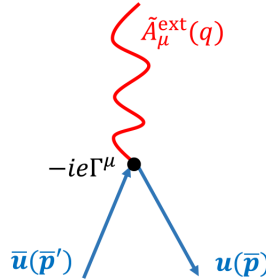


Figure 4.1: Tree-level diagram

We start by analyzing the scattering-matrix element \mathcal{M} for the scattering from an external field, represented by the tree-level diagram in Fig. 4.1, and written down as [71]

$$i\mathcal{M}(2\pi)\delta(p^0 - p^0) = -ie\bar{u}(\vec{p}')\Gamma^\mu u(\vec{p})\tilde{A}_\mu^{\text{ext}}(p' - p), \quad (4.3.1)$$

where \bar{u} and u are normalized solutions of the free Dirac equation [72], and $\tilde{A}_\mu^{\text{ext}}(\vec{p})$ is the Fourier transform of $A_\mu^{\text{ext}}(x)$, which is a classical external potential. By splitting the different vertex contributions in Eq. (4.3.1), we obtain

$$i\mathcal{M}(2\pi)\delta(p^0 - p^0) = -ie\bar{u}(\vec{p}')\Gamma^0 u(\vec{p})\tilde{\phi}^{\text{ext}}(q) + ie\beta\bar{u}(\vec{p}')\boldsymbol{\Gamma}u(\vec{p}) \cdot \tilde{\mathbf{A}}^{\text{ext}}(q), \quad (4.3.2)$$

with $p' - p = q$. Here, $\tilde{\phi}^{\text{ext}}$ and $\tilde{\mathbf{A}}^{\text{ext}}$ are the scalar and the vector potential, respectively. Lorentz invariance allows us to write the vertex Γ^μ as

$$\Gamma^\mu = \mathcal{Y}_1 \gamma^\mu + \mathcal{Y}_2 (\bar{p}'^\mu + \bar{p}^\mu) + \mathcal{Y}_3 (\bar{p}'^\mu - \bar{p}^\mu), \quad (4.3.3)$$

where \mathcal{Y}_i 's are scalar functions of the momentum and/or the fermionic mass. By applying the Ward identity $q_\mu \Gamma^\mu = 0$ in Eq. (4.3.3), we find that $\mathcal{Y}_3 = 0$. Therefore,

$$\Gamma^\mu = \mathcal{Y}_1 \gamma^\mu + \mathcal{Y}_2 (\bar{p}'^\mu + \bar{p}^\mu). \quad (4.3.4)$$

Now, using the Gordon identity, we rewrite Eq. (4.3.4) as

$$\bar{u}(\bar{p}') \Gamma^\mu u(\bar{p}) = \bar{u}(\bar{p}') \left[\gamma^\mu F_1(\bar{q}^2) + \frac{i\sigma^{\mu\nu} \bar{q}_\nu}{2\Delta} F_2(\bar{q}^2) \right] u(\bar{p}), \quad (4.3.5)$$

where F_1 and F_2 are form factors, and $\bar{q} = \bar{p}' - \bar{p}$. At the tree-level diagram, $F_1 = 1$ and $F_2 = 0$. Plugging the above result in Eq. (4.3.1), we have

$$i\mathcal{M}(2\pi)\delta(q_0) = -ie\bar{u}(\bar{p}') \left[\gamma^\mu F_1(\bar{q}^2) + \frac{i\sigma^{\mu\nu} \bar{q}_\nu}{2\Delta} F_2(\bar{q}^2) \right] u(\bar{p}) \tilde{A}_\mu^{\text{ext}}(q). \quad (4.3.6)$$

So far, we did not specify the spacetime dimension of the system studied. To understand better the problem in (2+1)D, let us follow the analysis performed in Ref. [71], but now for $\mu, \nu = 0, 1, 2$.

Focusing on the spatial component of the four-vector potential $A_\mu^{\text{ext}}(x) = (0, \mathbf{A}^{\text{ext}}(\mathbf{x}))$, or in the Fourier space $\tilde{A}_\mu^{\text{ext}}(\bar{q}) = (0, \tilde{\mathbf{A}}^{\text{ext}}(\mathbf{q}))$, one obtains

$$i\mathcal{M} = +ie\beta\bar{u}(\bar{p}') \left[\gamma^i F_1(\bar{q}^2) + \frac{i\sigma^{i\nu} \bar{q}_\nu}{2\Delta} F_2(\bar{q}^2) \right] u(\bar{p}) \tilde{\mathbf{A}}_{\text{ext}}^i(\mathbf{q}). \quad (4.3.7)$$

By performing a non-relativistic expansion of the spinor, i.e.

$$u(\bar{p}) = \begin{pmatrix} \sqrt{\bar{p} \cdot \bar{\sigma}} \xi \\ \sqrt{\bar{p} \cdot \bar{\sigma}} \xi \end{pmatrix} \approx \sqrt{\Delta} \begin{pmatrix} (1 - v_F \mathbf{p} \cdot \boldsymbol{\sigma} / 2\Delta) \xi \\ (1 + v_F \mathbf{p} \cdot \boldsymbol{\sigma} / 2\Delta) \xi \end{pmatrix},$$

with ξ a spinor in the spin space, $\sigma = (\mathbb{1}, \sigma^i)$ and $\bar{\sigma} = (\mathbb{1}, -\sigma^i)$, the first term in Eq. (4.3.7) yields

$$\begin{aligned} \bar{u}(\bar{p}') \gamma^i u(\bar{p}) &= 2\Delta v_F \xi^{\prime\dagger} \left(\frac{\mathbf{p}' \cdot \boldsymbol{\sigma}}{2\Delta} \sigma^i + \sigma^i \frac{\mathbf{p} \cdot \boldsymbol{\sigma}}{2\Delta} \right) \xi \\ &= 2\Delta v_F \xi^{\prime\dagger} \left[\frac{P^j \delta^{ji} \mathbb{1} - i\epsilon^{ijk} q^j \sigma^k}{2\Delta} \right] \xi, \end{aligned} \quad (4.3.8)$$

where $P^j = p'^j + p^j$. The first term in Eq. (4.3.8) is a contribution from the

operator $\mathbf{p} \cdot \mathbf{A} + \mathbf{A} \cdot \mathbf{p}$, while the second term is the magnetic-moment interaction. Notice that although in a strictly 2D system the momentum $p_z = 0$ (i.e. $j = 1, 2$), the set of Pauli matrices encounters the possibility of $k = 0, 1, 2$. Hence, for a non-vanishing magnetic moment interaction, there are two possibilities for the Levi-Civita, ϵ^{120} and ϵ^{210} , which leads to

$$\begin{aligned} & i(2\Delta\beta)\xi'^{\dagger} \left(\frac{2e}{2\Delta} \right) \frac{\sigma^0}{2} \xi(-i\epsilon^{ij0}v_Fq^j \tilde{\mathbf{A}}_{\text{ext}}^i(\mathbf{q})) = \\ & -i(2\Delta\beta)g_s\mu_B\xi'^{\dagger} \frac{\sigma^0}{2} \xi(-\nabla_{\perp} \cdot \mathbf{A}_{\text{ext}}(\mathbf{x})) = -i(2\Delta\beta)g_s\mu_B\mathcal{S}\mathcal{B}_{\perp}. \end{aligned} \quad (4.3.9)$$

Here, we used that $q_j \rightarrow -i\partial_j$ with $\nabla_{\perp} = (\partial_y, -\partial_x)$, $\mu_B = e/2\Delta$ is the Bohr magneton, \mathcal{S} is the electron's spin, \mathcal{B}_{\perp} is a magnetic field perpendicular to the electron's propagation and $g_s = 2$ (non-interacting case).

Proceeding with a similar analysis for the second term in Eq. (4.3.7), we obtain

$$\bar{u}(\vec{p}')\sigma^{i\nu}\bar{q}_{\nu}u(\vec{p}) = 2\Delta\xi'^{\dagger}\epsilon^{ij0}\sigma_0v_Fq_j\xi. \quad (4.3.10)$$

Now, by rewriting the contribution from Eq. (4.3.10) as the one in Eq. (4.3.9) and replacing both results together with Eq. (4.3.8) into Eq. (4.3.7), we obtain

$$i\mathcal{M} = i(2\Delta\beta)\xi'^{\dagger} \left(\frac{ev_F P^i \mathbf{1}}{2\Delta} \right) F_1 \xi \cdot \tilde{\mathbf{A}}_{\text{ext}}^i(\mathbf{q}) - i(2\Delta\beta)g_s(F_1 + F_2)\mu_B\mathcal{S}\mathcal{B}_{\perp}. \quad (4.3.11)$$

In the second term of Eq. (4.3.11), we observe how interaction effects can change the value of the spin g -factor, leading to a corrected g_s^* ($F_1 = 1$),

$$g_s^* \equiv 2 + 2F_2 = 2 + \mathcal{O}(\alpha). \quad (4.3.12)$$

In the following section, we calculate the value of this correction, i.e. the form factor F_2 .

4.4 Form factor calculation

Our aim in this section is to compute the one-loop correction to the electron's gyromagnetic factor g_s using the anisotropic PQED. For this, it is only necessary to calculate the finite part of the spatial component of the vertex represented in Fig. 4.2. According to Feynman's rules, the vertex diagram is given by

$$i\mathcal{M} = +ie\beta\bar{u} \int \frac{d^3k}{(2\pi)^3} \left\{ \Gamma_0^{\alpha} S_F(\vec{k} + \vec{p}') \gamma^i S_F(\vec{k} + \vec{p}) \Gamma_0^{\beta} G_{\alpha\beta}(k) \right\} u \tilde{\mathbf{A}}_{\text{cl}}^i, \quad (4.4.1)$$

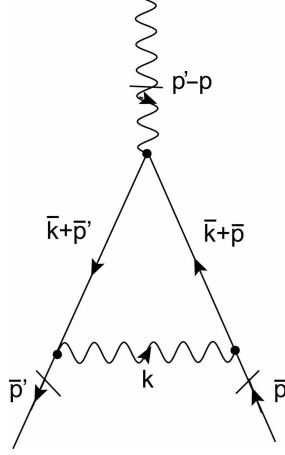


Figure 4.2: One-loop vertex correction.

with $\mathcal{M} = \Omega^i \tilde{\mathbf{A}}_{\text{cl}}^i$, and

$$\Omega^i = -\frac{ie^3 v_F}{2\varepsilon} \int \frac{d^3 k}{(2\pi)^3} \bar{u} \left\{ \frac{\gamma^\alpha [\gamma^\lambda (\bar{k}_\lambda + \bar{p}'_\lambda) + \Delta] \gamma^i [\gamma^\rho (\bar{k}_\rho + \bar{p}_\rho) + \Delta] \gamma_\alpha}{[(\bar{k} + \bar{p}')^2 - \Delta^2] [(\bar{k} + \bar{p})^2 - \Delta^2] \sqrt{k_0^2 - c^2 \vec{k}^2}} \right\} u. \quad (4.4.2)$$

To solve Eq. (4.4.2) and find the correction to the bare g -factor, first we rewrite the numerator of the integrand by using the properties of gamma matrices and the Dirac equations for u and \bar{u} . Then, we parametrize the denominator in order to obtain a single function of the momentum k , thus simplifying the integrals. By evaluating the integrals over both k_0 and \mathbf{k} separately, and focusing on the relevant terms to generate the anomalous gyromagnetic factor (see Sec. 4.A for details of the calculations), we find

$$\Omega_{gy}^i = -ie\beta\bar{u} \left(\frac{i}{2\Delta} F_2 v_F \sigma^{i\nu} q_\nu \right) u. \quad (4.4.3)$$

F_2 in Eq. (4.4.3) is the form factor discussed in Sec. 4.3, and is given by

$$F_2(q^2 \rightarrow 0) = -\frac{\alpha\beta^3 \bar{R}(\beta)}{2\pi}, \quad (4.4.4)$$

where

$$\bar{R}(\beta) = \frac{\beta\sqrt{\beta^2 - 1} + (1 - 6\beta^2 + 4\beta^4) \coth^{-1} \left(\beta/\sqrt{\beta^2 - 1} \right)}{\beta^3 (-1 + \beta^2)^{3/2}}.$$

For $\beta \ll 1$ we obtain $\beta^3 \bar{R}(\beta) \approx -(\pi/2)$, and the correction for the spin g_s -factor reads

$$F_2 = \Delta g_s = \frac{\alpha}{4}, \quad (4.4.5)$$

whereas for $\beta \approx 1$ (isotropic or fully relativistic limit) the correction is given by

$$\Delta g_s = -\frac{4\alpha}{3\pi}. \quad (4.4.6)$$

Although $F_2 = 0$ at the tree-level, it acquires a finite value at one-loop. The results (4.4.5) and (4.4.6) show the relevance of using the anisotropic description of PQED. The isotropic model leads to a correction with opposite sign, which decreases the value of the g -factor. Besides, the isotropic and the anisotropic theories describe very different physical regimes.

Notice, however, that there is a subtlety in the limit $\beta \rightarrow 0$. If one sets $\beta \approx 0$ from the start, the spatial-component contribution to the scattering-matrix element for the scattering from an external field is null (see Eq. (4.3.2)). This means that there would be no response to an applied external magnetic field. On the other hand, if one keeps β and performs the calculations (taking the limit afterwards), as we showed here, one finds a correction to the g -factor that is independent of the ratio v_F/c between the velocities. This is in agreement with the fact that experiments on the g -factor in graphene indicate an enhancement of its bare value $g = 2$.

4.5 Comparison with experiments

Even though the gyromagnetic factor is an intrinsic property of the electron in a certain medium, usually it is experimentally determined by applying a magnetic field \mathcal{B} perpendicularly to a sample and measuring the Zeeman gap $\Delta_z = g_s \mu_B \mathcal{B}$. We have shown in Sec. 4.3 how interaction effects lead to a correction to the bare value $g_s = 2$ of the gyromagnetic factor, and we calculated this correction in Sec. 4.4. Now, we proceed to compare our theoretical result to the experiments realized in graphene.

4.5.1 Graphene on SiO₂

To experimentally probe the enhancement of the gyromagnetic factor due to electron-electron interactions, one needs relatively strong magnetic fields, which lead to orbital quantization. As a result, the enhanced g -factor could exhibit a

dependence on the Landau-level index \mathcal{N} or on the applied \mathcal{B} -field. In metal-oxide-semiconductors (MOS), this dependence has been theoretically evaluated in Ref. [73], where the authors discuss a theory of oscillatory g -factor. This oscillatory behavior has been experimentally observed in GaAs/AlGaAs structures [74]. Recently, an oscillatory g -factor enhancement has been also proposed to occur in the case of graphene at strong magnetic fields [75]. However, measurements of the spin g -factor performed by Kurganova et al. for graphene grown on a SiO₂ substrate for the different values of the magnetic field, $\mathcal{B} = 5 - 7$ T, and Landau levels $\mathcal{N} = 2 - 10$, did not observe the predicted behavior [16]. Instead, the authors found that the enhancement of the g -factor in graphene in the strong \mathcal{B} -field regime is *independent* of the Landau level and is *constant* for all extracted data – exactly as in the case of weak magnetic fields. Their result is compatible with the regime of Gaussian-shaped Landau levels with broadening $\Gamma > g^* \mu_B \mathcal{B}$ [16]. Therefore, the computation of the spin splitting accounting for the dynamical electromagnetic interaction performed in Sec. 4.4, in the weak-field regime, is appropriate to describe the experiment.

By evaluating the corrected g -factor g_s^* multiplied by a dimensionless parameter, i. e. by the cyclotron mass m_c in units of the electron mass m_e , we obtain the following equivalence

$$\frac{m_c(n)g_s^*(n)}{m_e} = g_s^*(n) \frac{\hbar\sqrt{\pi n}}{v_F(n)m_e}. \quad (4.5.1)$$

This expression relates the cyclotron mass m_c to the charge carrier concentration n , and to the renormalized Fermi velocity [10]

$$v_F(n) = v_F(n_0) \left[1 - \frac{\alpha_0}{8\varepsilon_G(n)} \ln \left(\frac{n}{n_0} \right) \right]. \quad (4.5.2)$$

Here, $\alpha_0 = e^2/4\pi\varepsilon_0\hbar v_F(n_0)$, the vacuum permittivity $\varepsilon_0 = 1$, and $\varepsilon_G(n)$ is the dielectric constant, which was theoretically and empirically [7] found to depend on the carrier density n (see Ref. [43] for a thorough discussion about the dielectric constant in graphene).

It is known that the logarithm in the renormalized Fermi velocity v_F in graphene arises due to electron-electron interactions. For *undoped* graphene, via renormalization-group methods one finds that v_F depends on the smallest energy scale of the theory at which the RG flow is suppressed, namely the doping energy $\propto n$. If one considers *doped* graphene, this logarithmic dependence is not altered [76], but the effective interaction parameter is modified, i.e. $\alpha \rightarrow \alpha^* e^2/(4\pi\varepsilon_0\varepsilon_G(n)\hbar v_F(n))$. We have accounted for this effect by considering a dielectric function that depends on n , $\varepsilon_G(n)$ and using Eq. (4.5.2) for v_F .

The parameter g_s^* in Eq. (4.5.1) is the effective g_s -factor, which, in the experimental work, is taken to be the constant parameter that best fits the experimental points [16]. Recalling that the bare g_s -factor in graphene is $g_s = 2$, and replacing Eqs. (4.4.5) and (4.5.2) into Eq. (4.5.1), we obtain the corrected g_s -factor $g_s^* = 2 + 2\Delta g_s$,

$$\begin{aligned} \frac{m_c(n)g_s^*(n)}{m_e} &= \left(2 + \frac{\alpha}{2}\right) \frac{\hbar\sqrt{\pi n}}{m_e v_F^0} \frac{1}{\left[1 + \frac{\alpha_0}{8\varepsilon_G} \ln\left(\frac{n_0}{n}\right)\right]} \\ &= \frac{2}{\left[1 + \frac{\alpha_0}{8\varepsilon_G} \ln\left(\frac{n_0}{n}\right)\right]} \frac{\hbar\sqrt{\pi n}}{m_e v_F^0} \\ &+ \frac{e^2}{8\pi\hbar\varepsilon_0\varepsilon_G v_F^0 \left[1 + \frac{\alpha_0}{8\varepsilon_G} \ln\left(\frac{n_0}{n}\right)\right]^2} \frac{\hbar\sqrt{\pi n}}{m_e v_F^0}. \end{aligned} \quad (4.5.3)$$

Note that screening is taken into account in α and in $v_F(n)$. Choosing the reference value of n_0 around the values of n that we want to describe, and neglecting corrections of order $(\alpha_0/\varepsilon_G)^2$, we may write

$$\left[1 + \frac{\alpha_0}{8\varepsilon_G} \ln\left(\frac{n_0}{n}\right)\right]^2 \approx 1 + \frac{2\alpha_0}{8\varepsilon_G} \ln\left(\frac{n_0}{n}\right)$$

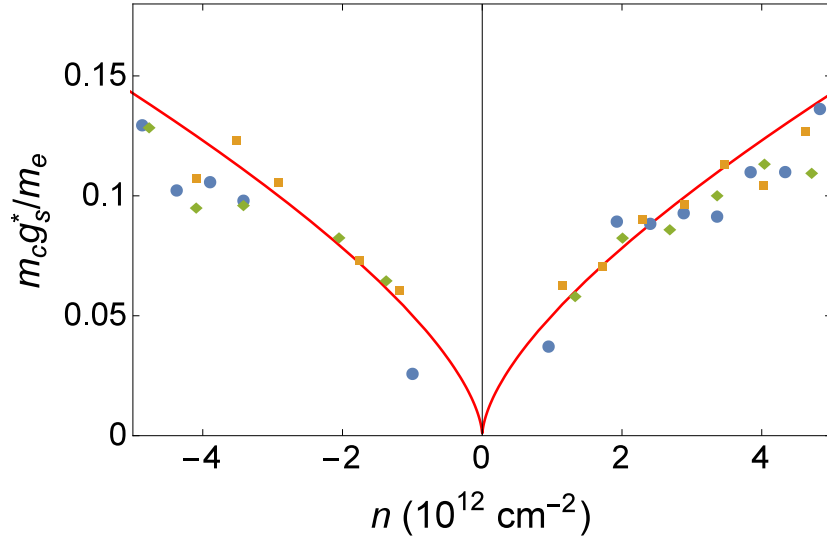


Figure 4.3: **g_s -factor enhanced due to electron-electron interactions.** At high densities, the theoretical red curve is given by Eq. (4.4.5), together with the renormalized value of $v_F(n)$ given by Eq. (4.5.2), and the reference value $v_F^0 = 1 \times 10^6$ m/s. Here, $\alpha = 0.9$ (i.e. $\varepsilon_G = 2.44$), which is the bare fine structure constant for graphene on SiO₂ [43].

to obtain

$$\frac{m_c g_s^*}{m_e} = \left\{ \frac{2}{\left[1 + \frac{\alpha_0}{8\varepsilon_G} \ln\left(\frac{n_0}{n}\right)\right]} \frac{\alpha_0}{2\varepsilon_G \left[1 + \frac{2\alpha_0}{8\varepsilon_G} \ln\left(\frac{n_0}{n}\right)\right]} \right\} \frac{\hbar\sqrt{\pi n}}{m_e v_F^0}. \quad (4.5.4)$$

In Fig. 4.3, we plot Eq. (4.5.4) for the value of $\alpha_0^* = \alpha_0/\varepsilon_G = 0.9$ (i.e. $\varepsilon_G = 2.44$), as given in Ref. [43] for graphene on SiO₂ [77]. The theoretical curve exhibits a very good agreement with the experimental data, indicating that interaction effects are able to capture the behavior of the g -factor in this material. This is the main result of this subsection. Notice that there are *no* fitting parameters in Fig. 4.3.

We proceed by investigating how the parameters in the theory, such as dielectric constant ε_G and bare Fermi velocity v_F^0 , modify the curve obtained in Fig. 4.3. For *ad hoc* values of the dielectric constant $\varepsilon_G = 3$ (black) and 5 (green), we plot Eq. (4.5.4) in Fig. 4.4. Upon increasing ε_G , the curve bends down for large carrier concentration values. The light-blue curve, corresponding to the bare value of the g -factor $g_s = 2$ clearly cannot describe the observed data, thus confirming the relevance of interactions in the description of the spin g -factor.

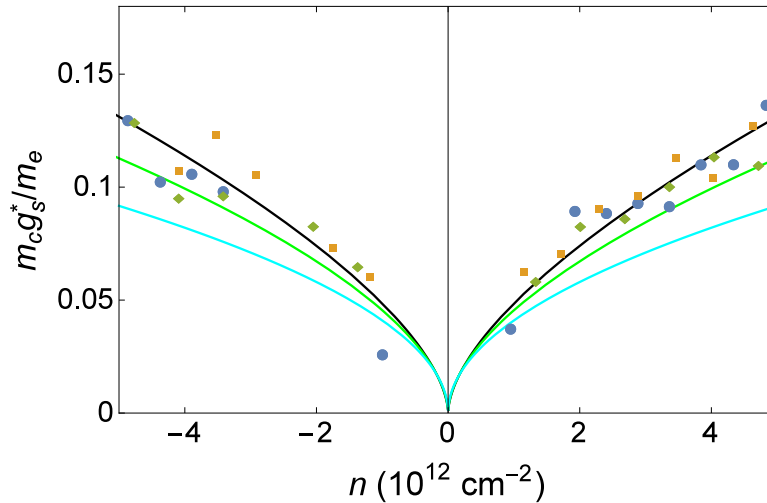


Figure 4.4: **Dependence of the g_s -factor on the dielectric constant ε_G .** The black and green solid curves correspond to different values of the dielectric constant, chosen *ad hoc* to be $\varepsilon_G = 3$ and 5, respectively. The light-blue solid curve denotes the bare $g_s = 2$ factor [16]. All the theoretical curves are given by Eq. (4.4.5), together with the renormalized value of $v_F(n)$ given by Eq. (4.5.2), and the reference value $v_F^0 = 1 \times 10^6$ m/s.

After having verified the trend of the g_s -factor renormalization upon varying the dielectric constant ε_G , as shown in Fig. 4.4, we compare the behavior of g_s^* upon fixing ε_G and varying the reference point v_F^0 , which arises within the RG

procedure. The dependence on v_F^0 may be observed in Fig. 4.5 (a), for the range of values compatible with the findings of Ref. [7].

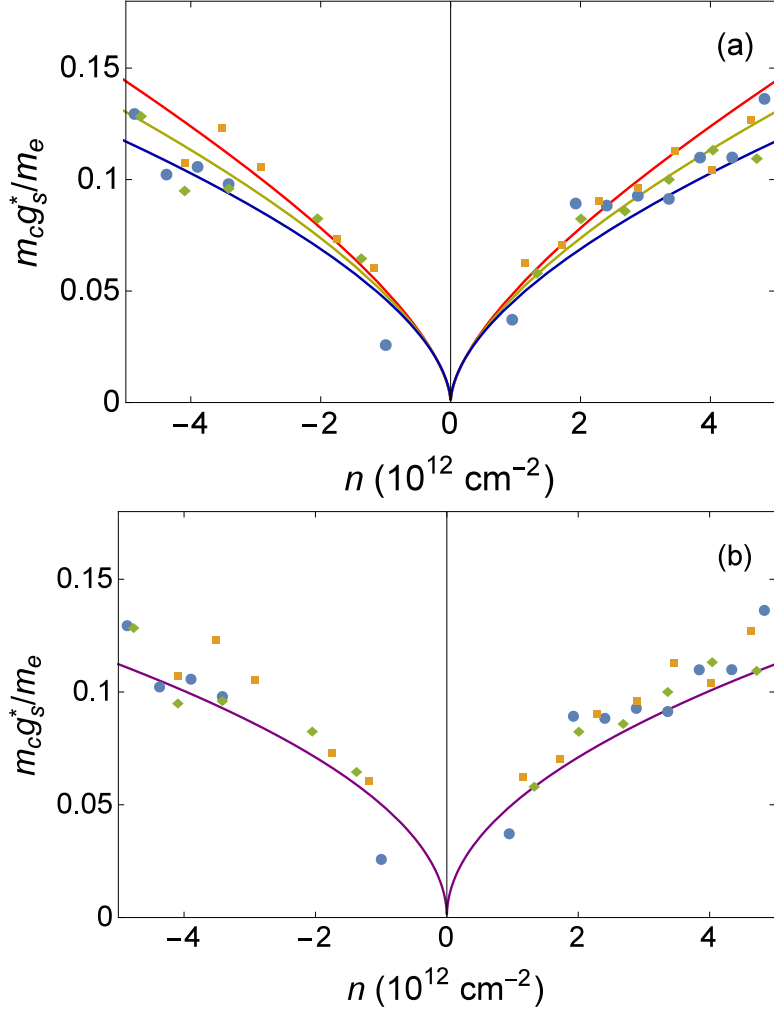


Figure 4.5: **Dependence of the g_s -factor on the reference value v_F^0 .** (a) The red curve is the same as in Fig. 4.3, for $v_F^0 = 1 \times 10^6 \text{ m/s}$, the yellow and blue curves are given by Eq. (4.5.4) with $v_F^0 = 1.25 \times 10^6 \text{ m/s}$ and $v_F^0 = 1.75 \times 10^6 \text{ m/s}$, respectively. We use $\varepsilon_G = 2.44$ for the three curves. (b) The purple curve is obtained from Eq. (4.4.5) for a non-renormalized $v_F^0 = 1 \times 10^6 \text{ m/s}$ and $\varepsilon_G = 2.44$, which results in a spin g -factor $g_s^* \approx 2.45$.

To complete the analysis, we also compare the value expected for the renormalization of the g_s -factor for the case of a non-renormalized Fermi velocity. In this case, by using a dielectric constant $\varepsilon_G = 2.44$, we obtain the value $g_s^* \approx 2.45$, which is represented by the purple curve in Fig. 4.5 (b). We can clearly observe the difference between the curves of Figs. 4.3 and 4.5 (b), where in the first we used a renormalized Fermi velocity, while in the second not.

4.5.2 Graphene on SiC(111)

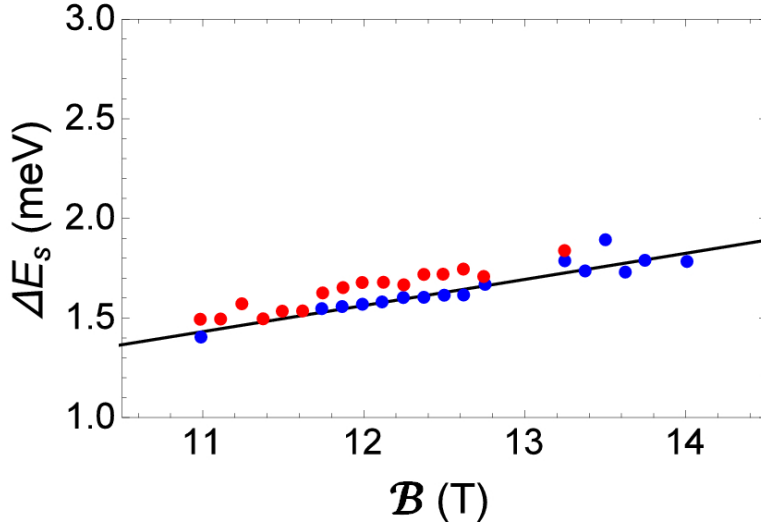


Figure 4.6: **Spin g -factor in graphene grown on SiC.** Comparison between theory and experiments for the spin g -factor. In the experiments, there is an asymmetry between the valleys, indicated by the red and blue points. They lead to a spin g -factor of $g_{s,K}^* = 2.23 \pm 0.01$ and $g_{s,K'}^* = 2.36 \pm 0.01$, respectively [21]. The black-solid line, which provides a good agreement with the experimental data, is obtained by using Eq. (4.4.5) and the fitting parameter $\alpha_0^* = 0.51$, since the precise value of the dielectric constant is unknown. The reference value for the magnetic field in the RG equations for the renormalized Fermi velocity used here is $\mathcal{B}_0 = 14$ T.

Measurements of the spin g -factor were performed also in graphene on SiC [21], where the top layer of multilayer epitaxial graphene grown on SiC was investigated by high-resolution scanning tunneling spectroscopy. At ultra-low temperatures, in extremely clean samples, these spin degeneracies may be lifted and the authors reported a small correction to the bare spin g -factor $\Delta g_s^* \approx 0.23 - 0.36$. These values $g_{s,K}^* = 2.23$ and $g_{s,K'}^* = 2.36$ (there is a small difference in the value measured for each of the valleys) are also comparable to the one obtained by Kurganova et al. [16] for graphene grown on SiO₂, $g_s^* = 2.7 \pm 0.2$.

We now confront these data to our results obtained within the PQED. In this experiment, the Zeeman splitting was measured, which is given by

$$\Delta E_s = g_s^*(\mathcal{B})\mu_B\mathcal{B}. \quad (4.5.5)$$

Inserting the value found for $g_s^* = 2 + 2\Delta g_s$ with Δg_s given by Eqs. (4.4.5) and (4.5.2), we obtain [78]

$$\Delta E_s = \left\{ 2 + \frac{\alpha_0}{2\varepsilon_G \left[1 + \frac{\alpha_0}{8\varepsilon_G} \ln \left(\frac{B_0}{B} \right) \right]} \right\} \mu_B \mathcal{B}. \quad (4.5.6)$$

We can observe in Ref. [21] that the experimentally detected spin-splitting does not change much when increasing the magnetic field from 11 to 14 T. We plot Eq. (4.5.6) for the spin-splitting in Fig. 4.6 using ε_G as a fitting parameter. By using $v_F^0 = 1.08 \times 10^6$ m/s [21], we find that $\varepsilon_G \approx 4$ for this sample, which falls within the range of values discussed in Ref. [79] for monolayer graphene on SiC.

4.6 Conclusions

In this chapter, we have investigated the corrections to the spin gyromagnetic factor in graphene that are generated due to electronic interactions. The calculations were performed in the framework of the anisotropic PQED, which is a theory that takes into account the full electromagnetic interaction and breaks Lorentz symmetry by considering two different velocities: c for the photons and v_F for the electrons. With these two ingredients, we have obtained an explicit expression for the spin g -factor correction, which has allowed us to compare our theoretical findings with experiments on graphene deposited on SiO₂ and on SiC.

The outcome of the comparison indicates that the renormalization of the Fermi velocity is very important to better describe the experiments. By combining this renormalization effect and choosing the dielectric constant according to the substrate, we have shown in Fig. 4.3 a very good agreement between our theoretical results and the experimental data.

Our work confirms the importance of electronic interactions in the description of graphene, and indicates that the PQED formalism is able to capture its signatures in great detail.

4.A Form factor detailed calculation

Here, we present the details of the calculation of Sec. 4.4. By using the anticommutation of the gamma matrices and the Dirac equations in momentum space $\bar{u}(\vec{p}')\gamma^\lambda\bar{p}'_\lambda = \bar{u}(\vec{p}')\Delta$ and $\gamma^\lambda\bar{p}_\lambda u(\vec{p}) = \Delta u(\vec{p})$, we can rewrite Eq. (4.4.2) of the main

text as

$$i\Omega^i = \frac{3e^3v_F}{8\varepsilon} \int_0^1 dx \int_0^{1-x} dy (1-x-y)^{-1/2} \times \int \frac{d^2k}{(2\pi)^2} \int_{-\infty}^{\infty} \frac{dk_0}{(2\pi)} \frac{\bar{u}(\bar{p}') [k_0^2 \gamma^i + \mathcal{I}_1^i + \mathcal{I}_2^i] u(\bar{p})}{(k_0^2 - \varsigma)^{5/2}}. \quad (4.A.1)$$

In the equation above, we used the parametric integral

$$\left\{ [(\bar{k} + \bar{p}')^2 - \Delta^2] [(\bar{k} + \bar{p})^2 - \Delta^2] \sqrt{k^2} \right\}^{-1} = \frac{3}{4} \int_0^1 dx \int_0^{1-x} dy \frac{(1-x-y)^{-1/2}}{[(k_0 + w_0)^2 - \varsigma]^{5/2}},$$

where

$$\varsigma = -\Upsilon (\mathbf{k}^2 - v_F^2 \Upsilon^{-1} \mathbf{w})^2 + w_0^2 + \Upsilon^{-1} v_F^4 \mathbf{w}^2,$$

with $\Upsilon = [-v_F^2(x+y) - c^2(1-x-y)]$, $w_0 = (p'_0 x + p_0 y)$ and $\mathbf{w} = (\mathbf{p}'x + \mathbf{p}y)$. We performed also the displacement $k_0 \rightarrow k_0 - w_0$, such that the terms in the numerator of Eq. (4.A.1) become

$$\begin{aligned} \mathcal{I}_1^i &\rightarrow [w_0^2 - 2w_0(p'_0 + p_0) + 4p'_0 p_0] \gamma^i + 2\gamma^i p'_0 \gamma^0 v_F \boldsymbol{\gamma} \cdot \mathbf{k} - 2p_0 \gamma^0 v_F \boldsymbol{\gamma} \cdot \mathbf{k} \gamma^i \\ &\quad - 2v_F k^i w_0 \gamma^0 + 2v_F^2 k^i \mathbf{k} \cdot \boldsymbol{\gamma} + (1/2)v_F^2 \mathbf{k}^2 \gamma^i \end{aligned}$$

and

$$\begin{aligned} \mathcal{I}_2^i \beta^{-2} &\rightarrow -4v_F^2 \gamma^i \{ (1-v_F) \mathbf{k}^2 + \mathbf{k} \cdot (\mathbf{p}' + \mathbf{p}) + \mathbf{p}' \cdot \mathbf{p} \} + 4v_F p'^i w_0 \gamma^0 + 4v_F k^i w_0 \gamma^0 \\ &\quad + 2v_F (\mathbf{p}' + \mathbf{p}) \cdot \boldsymbol{\gamma} \gamma^i w_0 \gamma^0 + 2v_F (p_0 - p'_0) \gamma^0 \boldsymbol{\gamma} \cdot \mathbf{k} \gamma^i + 4v_F (\Delta - p'_0 \gamma^0) k^i \\ &\quad + 4v_F^2 (p^i + p'^i) \boldsymbol{\gamma} \cdot \mathbf{k}, \end{aligned}$$

where we eliminated the odd terms in k_0 .

As a next step, we try to simplify the lengthy expressions. Since we are interested in obtaining the gyromagnetic factor, we will disregard the terms proportional to γ^i . After solving the integral over k_0 , we find

$$i\Omega_{gy}^i = \frac{3e^3v_F}{16\pi\varepsilon} \int_0^1 dx \int_0^{1-x} dy (1-x-y)^{-1/2} \times \int \frac{d^2\mathbf{k}}{(2\pi)^2} \frac{\bar{u}(\bar{p}') \left[\frac{4}{3} (-2v_F^3 \Upsilon^{-1} w^i w_0 \gamma^0 + 2v_F^6 \Upsilon^{-2} w^i \boldsymbol{\gamma} \cdot \mathbf{w}) + \beta^2 \mathcal{I}_3^i \right] u(\bar{p})}{\Upsilon^2 [(k^2 - v_F^2 \Upsilon^{-1} \mathbf{w})^2 - \tilde{\varsigma}]^{5/2}},$$

where $\mathcal{I}_3^i = 4\Delta v_F^3 \Upsilon^{-1} w^i + 4v_F^4 \Upsilon^{-1} (p^i + p'^i) \boldsymbol{\gamma} \cdot \mathbf{w}$ and $\tilde{\varsigma} = (w_0^2 + \Upsilon^{-1} v_F^4 \mathbf{w}^2) \Upsilon^{-1}$. Displacing $\mathbf{k} \rightarrow \mathbf{k} + v_F^2 \Upsilon^{-1} \mathbf{w}$, we find, after solving the integrals over \mathbf{k} ,

$$i\Omega_{gy}^i = -\frac{e^3v_F}{16\pi^2\varepsilon} \int_0^1 dx \int_0^{1-x} dy (1-x-y)^{-1/2} \left(\frac{2v_F^6 \Upsilon^{-2} w^i \boldsymbol{\gamma} \cdot \mathbf{w} + \beta^2 \mathcal{I}_3^i}{\Upsilon^2 \tilde{\varsigma}} \right),$$

where we considered $p_0 = p'_0 = 0$. Therefore, working on mass-shell, we can use that $v_f \gamma^j p_j = \Delta$. By using that $2p^i = P^i + q^i$ and $2p^i = P^i - q^i$, we can write $2v_F^6 \Upsilon^{-2} w^i \boldsymbol{\gamma} \cdot \mathbf{w} \rightarrow -\Delta v_F^5 \Upsilon^{-2} P^i (x+y)^2$ and $\mathcal{I}_3^i \rightarrow -2\Delta v_F^3 \Upsilon^{-1} P^i (x+y)$. Now, we can use the Gordon identity

$$\bar{u} P^i u = 2\Delta \bar{u} \gamma^i u - i \bar{u} \sigma^{i\nu} q_\nu u,$$

and write

$$\Omega_{gy}^i = -ie\beta \bar{u} \left(\frac{i}{2\Delta} F_2 v_F \sigma^{i\nu} q_\nu \right) u.$$

Hence, the form factor F_2 is identified as

$$F_2 = -\frac{\alpha\beta}{2\pi} \int_0^1 dx \int_0^{1-x} dy (1-x-y)^{-1/2} \left\{ \frac{\Delta^2 v_F^2 \left[2(x+y) - \frac{(x+y)^2}{\beta^2(x+y)+(1-x-y)} \right]}{\Upsilon v_F^2 (\mathbf{p}'x + \mathbf{p}y)^2} \right\}. \quad (4.A.2)$$

By rewriting the denominator of Eq. (4.A.2) as

$$v_F^2 (\mathbf{p}'x + \mathbf{p}y)^2 = -\Delta^2 (x+y)^2 + q^2 xy,$$

with $q^2 = (p' - p)^2$ and using that $q^2 \rightarrow 0$, we obtain

$$F_2 = -\frac{\alpha\beta^3 \bar{R}(\beta)}{2\pi}, \quad (4.A.3)$$

with

$$\begin{aligned} \bar{R}(\beta) &= \int_0^1 dx \int_0^{1-x} dy \frac{2(1-x-y)^{-1/2}}{(x+y)[\beta^2(x+y) + (1-x-y)]} \\ &- \int_0^1 dx \int_0^{1-x} dy \frac{(1-x-y)^{-1/2}}{[\beta^2(x+y) + (1-x-y)]^2}. \end{aligned} \quad (4.A.4)$$

In the limit of $v_F = c = 1$, we find

$$\int_0^1 dx \int_0^{1-x} dy \frac{(1-x-y)^{-1/2} (2-x-y)}{(x+y)} = \frac{8}{3},$$

which is exactly what is obtained in the isotropic model.

On the other hand, if we solve the integrals in Eq. (4.A.4), we find

$$\bar{R}(\beta) = \frac{\beta \sqrt{\beta^2 - 1} + (1 - 6\beta^2 + 4\beta^4) \coth^{-1} \left(\beta / \sqrt{\beta^2 - 1} \right)}{\beta^3 (-1 + \beta^2)^{3/2}}. \quad (4.A.5)$$

PART II: TOPOLOGICAL INSULATORS
AND INTERACTIONS

EXCITONIC GAP GENERATION IN THIN-FILM TOPOLOGICAL INSULATORS

In this chapter, we analyze the excitonic gap generation in the strong-coupling regime of thin films of 3D time-reversal-invariant TIs. We start by writing down the effective gauge theory in (2+1)D from the projection of the (3+1)D QED. Within this method, we obtain a short-range interaction, which has the form of a Thirring-like term, and a long-range one. The interaction between the two surface states of the material induces an excitonic gap. By using the large- N approximation in the strong-coupling limit, we find that there is a dynamical mass generation for the excitonic states that preserves time-reversal symmetry and is related to the dynamical chiral-symmetry breaking of our model. This symmetry breaking occurs only for values of the fermion-flavor number smaller than $N_c \approx 11.8$. Our results show that the inclusion of the full dynamical interaction strongly modifies the critical number of flavors for the occurrence of exciton condensation, and therefore, cannot be neglected.

Note: This chapter is based in Ref. [80], where I contributed by performing all the calculations of the work.

5.1 Introduction

Topological materials are, nowadays, a rich and well developed research field in condensed-matter physics. The study of 2D topological systems started in the early 80's, with the experimental discovery of the IQHE in GaAs [34]. Thereafter, the deep relation between this novel phase and the topological invariant

induced by a non-trivial Berry phase was theoretically unveiled [35]. An essential feature of these quantum states is that time-reversal symmetry is broken in the bulk. However, the recent discovery of 2D TIs [22, 24, 28, 81] has opened the way to the exploration and classification of a vast number of novel materials, also in higher dimensions. In 3D, similar versions of 2D TIs have been firstly theoretically formulated [25] and then experimentally discovered [26, 27]. These systems support surface gapless modes, topologically protected by the non-trivial topological number in the gapped bulk.

Although the free-fermion topological phases have been completely classified for all dimensions in terms of their symmetries [29, 31], much less is known about the complete classification and characterization of interacting systems, where a variety of quantum phenomena and quasi-particles emerge in the low-energy regime. This is the case of anyons in fractional quantum Hall states [82–84] and fractional TIs [85, 86], which carry fractional electric charge and spin, Cooper pairs (bound states of spin-up and spin-down electrons) in topological superconductors [87], and excitons, i.e. particle-hole bound states in bilayer systems [88–92]. At the microscopic level, Hubbard-like Hamiltonians have been employed in the study of exciton condensation in monolayer [93] and bilayer graphene [94], bilayer quantum Hall systems [88, 95, 96] and in 3D thin-film TIs in the class AII [97–99]. In the latter case, the electron-hole pairs residing on the surface states can condense to form a topological exciton condensate. This kind of condensation can be seen as an electronic superfluid with dissipationless electronic transport and could enable ultra-low-power and energy-efficient devices, as already proposed in Ref. [100]. At a theoretical level, mean-field theory studies show the presence of an excitonic gap induced by the short-range part of the Coulomb interaction between the surface states [97].

Here, we propose a precise and self-consistent derivation of the gauge theory describing the short-range interaction in thin films of TIs. In these materials, the free-surface states are defined in terms of massless Dirac fermions and the corresponding interactions are encoded in QED. Our theoretical model is based on the fact that the massless Dirac fermions are confined on the 2D surfaces, while the virtual photons that mediate their quantum electromagnetic interactions are free to propagate in the 3D surrounding space. This approach has been already successfully employed in the study of several quantum systems, such as graphene [50, 67], transition-metal dichalcogenides [101], and the edge modes of 2D TIs [102]. The local part of our effective field theory is given by a generalized (2+1)D Thirring model, which has important applications in both condensed-matter and particle physics [103–106], and represents one the main results of this chapter. Importantly, our approach fixes uniquely the value of its coupling constant, which

turns out to be proportional to the electric charge and the width of our thin-film TI.



Figure 5.1: The surfaces of a 3D TI separated by a distance d .

Moreover, if on one hand our work reproduces the effective local Hubbard-like model proposed in Ref. [97], on the other hand it does not require any mean-field theory approximation for the identification of the exciton mass gap. By solving the Schwinger-Dyson equation [17] for the (2+1)D effective field theory in the strong-coupling regime, we show that the mass generation in the exciton condensation is induced dynamically. The dynamical mass generation is due to the breaking of the chiral symmetry [107–110], and represents a non-perturbative phenomenon, beyond the standard mean-field theory.

5.2 The model

We start our analysis with the description of two gapless surface states in 3D thin-film TIs in class AII. They support an odd number of topologically protected helical massless Dirac fermions, which are described by a (2+1)D Dirac theory. We then consider the interactions in and between the two surfaces by including a quantum dynamical U(1) gauge field coupled to the Dirac fermions. This is encoded in the standard QED by introducing a minimal coupling between the gauge potential A_μ and the fermionic current J_μ . Importantly, while the massless fermions are confined on the surfaces of the material, the virtual photons that carry the electromagnetic interaction are free to propagate in the 3D space. This is the crucial assumption that will allow us to derive an effective (2+1)D projected theory. Thus, for simplicity, we consider a single Dirac fermion per surface, such that our system is described by the following QED-like action

$$S = i\hbar \int d^3r (\bar{\psi}_t \sigma^\mu \partial_\mu \psi_t + \bar{\psi}_b \bar{\sigma}^\mu \partial_\mu \psi_b) - \int d^4r \left(\frac{\varepsilon_0 c}{4} F_{\alpha\beta} F^{\alpha\beta} + e J_{3+1}^\alpha A_\alpha \right), \quad (5.2.1)$$

where ψ_b and ψ_t denote two-component fermionic fields with $\bar{\psi}_i = \psi_i^\dagger \sigma^0$, which are constrained to propagate on the *top* (t) and *bottom* (b) surfaces of the TI,

respectively. Here, σ^μ are 2×2 Pauli matrices with $\mu = 0, 1, 2$, and we adopt $\bar{\sigma}^\mu = -\sigma^\mu$, meaning that the two fermions have opposite helicity. The differential elements are given by $d^3r = v_F dx dy dt$ and $d^4r = c dx dy dz dt$, with v_F and c the Fermi velocity and the speed of light, respectively. The coupling constant between the matter current and the gauge field e is the electric charge carried by each fermion. ε_0 is the vacuum dielectric constant, $F_{\alpha\beta} = \partial_\alpha A_\beta - \partial_\beta A_\alpha$ is the field-strength tensor, $J_{3+1}^\alpha = j_t^\alpha + j_b^\alpha = \bar{\psi}_t \sigma^\alpha \psi_t + \bar{\psi}_b \bar{\sigma}^\alpha \psi_b$, and $\alpha, \beta = 0, 1, 2, 3$.

We will focus on the interaction between the two fermionic species $\psi_{t,b}$, which in our context represent quasi-particles and quasi-holes confined on two different surfaces. As illustrated in Fig. 5.1, the surfaces of the 3D TI are separated by a distance d , which is the width of the thin-film, and we describe the surface Dirac fermions by imposing the following constraints on the matter current

$$j_{t,b}^\alpha(t, x, y, z) = \begin{cases} j_t^\alpha(t, x, y) \delta(z - d/2), \\ j_b^\alpha(t, x, y) \delta(z + d/2). \end{cases} \quad (5.2.2)$$

Because the fermions interact with a dynamical quantum electromagnetic field, we can integrate out the gauge field to obtain the effective non-local interaction term

$$S_{\text{int}}^{\text{eff}} = -\frac{e^2}{2} \int d^4r d^4r' J_{3+1}^\alpha(r) \frac{1}{(-\square)} J_\alpha^{3+1}(r'). \quad (5.2.3)$$

By imposing the constraints given in Eq. (5.2.2) we are effectively describing the system as a single surface living in the middle of the thin-film. Hence, Eq. (5.2.3) becomes

$$S_{\text{int}}^{\text{eff}} = -\frac{e^2}{2} \int d^3r d^3r' j_\kappa^\mu(r) V_{\kappa\rho}(r - r') j_\mu^\rho(r'), \quad (5.2.4)$$

where $V_{\kappa\rho}(r - r') = [1/(-\square)]_{\xi_{\kappa\rho}}$, $\kappa, \rho = t, b$ and $\xi_{\kappa\rho}$ represents the different values at which the Green's function has to be evaluated.

Although the system from now on may be treated as an effectively 2D surface, the information about the thin-film width d is carried within the projection. As known in the literature [98, 99, 111], the exciton condensation in thin-films may only occur when the inter-surface distance d is smaller than an in-plane characteristic distance a , i.e. $d/a < 1$. We introduce this minimal in-plane distance a in our model by shifting the coordinates of the quasiparticles as follows: $r \rightarrow r - a/2$ and $r' \rightarrow r' + a/2$. In this way, Eq. (5.2.4) becomes

$$S_{\text{int}}^{\text{eff}} = -\frac{e^2}{2} \int d^3r d^3r' j_\kappa^\mu(r - a/2) V_{\kappa\rho}(r - r' - a) j_\mu^\rho(r' + a/2), \quad (5.2.5)$$

and now the effective interaction carries the information about the length a .

The explicit values of $\xi_{\kappa\rho}$ are

$$\begin{aligned}\xi_{tt} : z = z' = d/2, \quad \xi_{tb} : z = d/2 \text{ and } z' = -d/2, \\ \xi_{bt} : z' = d/2 \text{ and } z = -d/2, \quad \xi_{bb} : z = z' = -d/2,\end{aligned}$$

where, after the projection, the top and bottom components represent two different flavors in the effective middle plane. For both ξ_{tt} and ξ_{bb} , we obtain similar results as found in Ref. [45], namely

$$\left[\frac{1}{(-\square)} \right]_{\xi_{ii}} = \frac{1}{2} \int \frac{d^3k}{(2\pi)^3} \frac{e^{ik \cdot (r-r'-a)}}{\sqrt{k^2}} = \frac{1}{4\pi^2(|r-r'-a|^2 + a^2)}, \quad (5.2.6)$$

where a settles a minimum distance between the quasiparticles, implying a cutoff on the momenta $k_{\max} = 1/a$. The terms ξ_{tb} and ξ_{bt} yield

$$\left[\frac{1}{(-\square)} \right]_{\xi_{ij}} = \frac{1}{2} \int \frac{d^3k}{(2\pi)^3} \frac{e^{-d\sqrt{k^2}} e^{ik \cdot (r-r'-a)}}{\sqrt{k^2}}. \quad (5.2.7)$$

Now, by considering that $d|k| < 1$ [99, 111, 112], we expand the exponential $\exp(-d|k|) \approx 1 - d|k|$ and perform the integration over k to find

$$\left[\frac{1}{(-\square)} \right]_{\xi_{ij}} \approx \frac{1}{4\pi^2(|r-r'-a|^2 + a^2)} - \frac{d}{2} \delta^3(r-r'-a). \quad (5.2.8)$$

Here, we used the approximation

$$\int \frac{d^3k}{(2\pi)^3} e^{ik \cdot (r-r'-a)} \approx \delta^3(r-r'-a). \quad (5.2.9)$$

We can finally summarize the results for the effective interaction $V_{\kappa\rho}$ after the projection,

$$\begin{aligned}V_{tt} = V_{bb} &= \frac{1}{4\pi^2|r-r'-a|^2}, \\ V_{tb} = V_{bt} &\approx \frac{1}{4\pi^2|r-r'-a|^2} - \frac{d}{2} \delta(r-r'-a).\end{aligned}$$

where we neglected terms proportional to $a^2 \approx 0$. By plugging back the interactions above into Eq. (5.2.5), we may write down $S_{\text{int}}^{\text{eff}}$ as a long and a short-range contribution (see Sec. 5.A for details).

5.3 Single-surface description

The aim of this section is to describe a two-surface system in terms of a single effective surface with two species of fermions. Our (2+1)D effective action after the projection is given by

$$S^{\text{eff}} = i\hbar \int d^3r (\bar{\psi}_t \sigma^\mu \partial_\mu \psi_t - \bar{\psi}_b \sigma^\mu \partial_\mu \psi_b) - \frac{e^2}{2\varepsilon_0 c} \int d^3r' \int d^3r j_\kappa^\mu V_{\kappa\rho} j_\mu^\rho, \quad (5.3.1)$$

where $\kappa, \rho = t, b$ represent the different surfaces. Now, we can rewrite the action (5.3.1) in terms of a single spinor $\Psi = (\psi_t \ \psi_b)^\top$. For the kinetic part, we obtain

$$\begin{aligned} \bar{\psi}_t \sigma^\mu \partial_\mu \psi_t - \bar{\psi}_b \sigma^\mu \partial_\mu \psi_b &= (\bar{\psi}_t \ \bar{\psi}_b) \begin{pmatrix} \sigma^\mu \partial_\mu & 0 \\ 0 & -\sigma^\mu \partial_\mu \end{pmatrix} \begin{pmatrix} \psi_t \\ \psi_b \end{pmatrix} = \bar{\Psi} \sigma^0 \otimes \sigma^\mu \partial_\mu \Psi \\ &= \bar{\Psi} \gamma^\mu \partial_\mu \Psi, \end{aligned} \quad (5.3.2)$$

where $\gamma^\mu \equiv \sigma^0 \otimes \sigma^\mu$. The 4×4 γ -matrices are defined as [106]

$$\gamma^\mu = \begin{pmatrix} \sigma^\mu & 0 \\ 0 & -\sigma^\mu \end{pmatrix},$$

with

$$\gamma^0 = \begin{pmatrix} \sigma^0 & 0 \\ 0 & -\sigma^0 \end{pmatrix}, \quad \gamma^\tau = i \begin{pmatrix} \sigma^\tau & 0 \\ 0 & -\sigma^\tau \end{pmatrix}.$$

and $\tau = 1, 2$. The fermionic currents can be written in terms of the new spinors

$$\begin{aligned} j_t^\mu &= (\bar{\psi}_t \ \bar{\psi}_b) \begin{pmatrix} \sigma^\mu & 0 \\ 0 & 0 \end{pmatrix} \begin{pmatrix} \psi_t \\ \psi_b \end{pmatrix} = \frac{1}{2} \bar{\Psi} (\mathbf{1} + \sigma^0) \otimes \sigma^\mu \Psi \\ &= \frac{1}{2} (\bar{\Psi} \gamma^\mu \Psi - i \bar{\Psi} \gamma^\mu \gamma^3 \gamma^5 \Psi), \end{aligned} \quad (5.3.3)$$

$$\begin{aligned} j_b^\mu &= (\bar{\psi}_t \ \bar{\psi}_b) \begin{pmatrix} 0 & 0 \\ 0 & \bar{\sigma}^\mu \end{pmatrix} \begin{pmatrix} \psi_t \\ \psi_b \end{pmatrix} = \frac{1}{2} \bar{\Psi} (\mathbf{1} - \sigma^0) \otimes \bar{\sigma}^\mu \Psi \\ &= \frac{1}{2} (\bar{\Psi} \gamma^\mu \Psi + i \bar{\Psi} \gamma^\mu \gamma^3 \gamma^5 \Psi), \end{aligned} \quad (5.3.4)$$

where $\mathbf{1} \otimes \sigma^\mu = -i \gamma^\mu \gamma^3 \gamma^5$, with

$$\gamma^3 = i \begin{pmatrix} 0 & \mathbf{1} \\ -\mathbf{1} & 0 \end{pmatrix}, \quad \gamma^5 = i \gamma^0 \gamma^1 \gamma^2 \gamma^3 = \begin{pmatrix} 0 & \mathbf{1} \\ \mathbf{1} & 0 \end{pmatrix}.$$

Once we have expressed all contributions to the effective action (5.3.1) in terms of four-component spinors $\bar{\Psi}$ and Ψ , we can write down the following single-surface action (see Sec. 5.B for details)

$$S^{\text{eff}}[\bar{\Psi}, \Psi] = -\frac{e^2}{2\varepsilon_0 c} \int d^3 r' \int d^3 r \mathcal{J}^\mu \frac{1}{4\pi^2 |r - r'|^2} \mathcal{J}_\mu + \hbar \int d^3 r \left[i\bar{\Psi} \gamma^\mu \partial_\mu \Psi + \frac{e^2 d}{8\hbar \varepsilon_0 c} (\mathcal{J}^\mu \mathcal{J}_\mu + \mathcal{J}_{35}^\mu \mathcal{J}_\mu^{35}) \right], \quad (5.3.5)$$

where $\mathcal{J}^\mu \equiv \bar{\Psi} \gamma^\mu \Psi$ and $\mathcal{J}_{35}^\mu \equiv \bar{\Psi} \gamma^\mu \gamma^3 \gamma^5 \Psi$.

5.4 Dynamical gap generation

In the previous section, we derived an effective single-surface interacting model (see Eq. (5.3.5)), which involves both a short- and a long-range interaction. The former corresponds to a generalized Thirring model [105, 109], while the latter is similar to the non-local field theory studied in Refs. [50, 101, 110]. These kind of interactions have been already studied separately in the context of dynamical mass generation in Refs. [107–110]. This mechanism is relevant in interacting quantum-field theories and is related to the dynamical breaking of a classical symmetry due to quantum effects. In fact, all the three interaction terms in our effective action (5.3.5) are invariant under chiral symmetry, which is dynamically broken at the quantum level. In the first part of this section, we will focus on the short-range interactions $\mathcal{J}^\mu \mathcal{J}_\mu + \mathcal{J}_{35}^\mu \mathcal{J}_\mu^{35}$. By following the approach developed in Ref. [107], we will show that in the strong-coupling regime both Thirring-like terms yield the same mass generation, and their combined action leads to a larger critical number of fermion flavors N_c , as compared to a single Thirring term. At last, we will add the long-range interaction and show that the excitonic gap is then enhanced, in agreement with the results found in Refs. [93, 113] for the case of Gross-Neveu theory.

5.4.1 Short-range interactions

Firstly, let us focus on the dynamical mass generated due to the Thirring-like interactions of Eq. (5.3.5). In the large- N approximation, we can write down the effective Lagrangian as

$$\mathcal{L}^{\text{eff}}[\bar{\Psi}, \Psi] = i\hbar \bar{\Psi}_a \gamma^\mu \partial_\mu \Psi_a + \frac{\tau_N}{2N} (\bar{\Psi}_a \gamma^\mu \gamma^3 \gamma^5 \Psi_a \bar{\Psi}_{\bar{a}} \gamma_\mu \gamma^3 \gamma^5 \Psi_{\bar{a}} + \bar{\Psi}_a \gamma^\mu \Psi_a \bar{\Psi}_{\bar{a}} \gamma_\mu \Psi_{\bar{a}}),$$

where $\tau_N = e^2 d N / 4\varepsilon_0 c$. Here the indexes a, \bar{a} denote a sum over N fermion flavors. Through a Hubbard-Stratonovich transformation, we introduce two auxiliary

vector fields W_n^μ ($n = 1, 2$) and two scalar fields ϕ_n in a way to preserve gauge symmetry. Thus, we obtain

$$\mathcal{L}^{\text{eff}}[\bar{\Psi}, \Psi, W^1, W^2, \phi^1, \phi^2] = i\hbar\bar{\Psi}_a\gamma^\mu\tilde{D}_\mu\Psi_a - \sum_{n=1,2} \frac{1}{2\tau_N} \left(W_n^\mu - \sqrt{N}\partial^\mu\phi_n\right)^2 \quad (5.4.1)$$

where $\tilde{D}_\mu = \partial_\mu - (i/\sqrt{N})\gamma^3\gamma^5W_\mu^1 - (i/\sqrt{N})W_\mu^2$. By following a similar procedure as adopted in Ref. [107], we introduce a non-local gauge-fixing term of the form

$$-\frac{1}{2} \left[\partial_\mu W^\mu + \sqrt{N} \frac{\zeta(\partial^2)}{\tau_N} \phi \right] \frac{1}{\zeta(\partial^2)} \left[\partial_\nu W^\nu + \sqrt{N} \frac{\zeta(\partial^2)}{\tau_N} \phi \right]$$

for each gauge field W_n^μ in the Lagrangian (5.4.1). As a result, we obtain

$$\begin{aligned} \mathcal{L}^{\text{eff}}[\psi, \bar{\psi}, W^1, W^2] + \mathcal{L}^{\text{eff}}[\phi^1, \phi^2] &= i\hbar\bar{\Psi}_a\gamma^\mu\tilde{D}_\mu\Psi_a - \frac{1}{2\tau_N}W_\mu^nW_n^\mu \\ &- \frac{1}{2}\partial_\mu W_n^\mu \frac{1}{\zeta(\partial^2)}\partial_\nu W_n^\nu - \frac{1}{2\tau_N} [\zeta(\partial^2)\phi_n] \phi_n - \frac{1}{2}\partial_\mu\phi_n\partial^\mu\phi_n, \end{aligned} \quad (5.4.2)$$

where the gauge-fixing term decoupled the ϕ -boson fields, which have also been rescaled as $\sqrt{N/\tau_N}\phi_n \rightarrow \phi_n$. The double index n indicates a summation over the fields. Notice in Eq. (5.4.2) that only the strong-coupling regime $\tau_N \rightarrow \infty$ preserves gauge symmetry, leading to a massless gauge boson. We shall return to this point later in the Schwinger-Dyson analysis.

Once we have obtained the gauge theory in Eq. (5.4.2), we proceed by defining the Feynman rules needed for calculating the mass generation. The full fermion propagator reads

$$S_F(p) = \frac{i}{C_\Psi(-p^2)\gamma^\mu p_\mu - C_m(-p^2)}, \quad (5.4.3)$$

where C_Ψ represents a correction to the fermion-field wave function, and C_m is the order parameter of the chiral symmetry, which preserves parity in (2+1)D. The Schwinger-Dyson equation for the fermion two-point function is given by

$$S_F^{-1}(p) = S_{F,0}^{-1}(p) - i\Sigma(p), \quad (5.4.4)$$

where $S_{F,0} = i/\gamma^\mu p_\mu$ is the free-fermion propagator. The self-energy Σ contains the contribution from both types of local interaction, and it is determined by

$$\begin{aligned} -i\Sigma &= -\frac{1}{N} \int \frac{d^3k}{(2\pi)^3} \gamma^\mu \gamma^3 \gamma^5 S_F(k) \Gamma^\nu \gamma^3 \gamma^5 G_{\mu\nu}^1(p-k) \\ &- \frac{1}{N} \int \frac{d^3k}{(2\pi)^3} \gamma^\mu S_F(k) \Gamma^\nu G_{\mu\nu}^2(p-k). \end{aligned} \quad (5.4.5)$$

Γ^ν and $G_{\mu\nu}^n$ are the full-vertex function and the full gauge-boson propagators, respectively. Here, we will adopt the bare-vertex approximation, i.e. $\Gamma^\nu = \gamma^\nu$. The explicit expression for the full gauge-boson propagator reads

$$G_{\mu\nu}^n(k) = iG_0^n(-k^2) \left(g_{\mu\nu} - \eta(-k^2) \frac{k_\mu k_\nu}{k^2} \right), \quad (5.4.6)$$

where $G_0^1 = 1/(g^{-1} - \Pi)$, $G_0^2 = 1/(g^{-1} + \Pi)$, and η is a non-trivial function of the momentum related to the non-local gauge approximation [107]. The function $\Pi(-k^2)$ emerges from the one-loop polarization tensor, inducing dynamics to the gauge fields W_μ^n through interaction effects.

In the strong-coupling regime ($\tau_N \rightarrow \infty$), both contributions in Eq. (5.4.5) reduce to a single term. By replacing the respective Γ^ν and $G_{\mu\nu}^n$ functions into Eq. (5.4.5) and using that $[\gamma^\mu, \gamma^3 \gamma^5] = 0$, we obtain

$$\begin{aligned} [C_\Psi(p^2) - 1] \gamma^\mu p_\mu - C_m(p^2) = \\ \frac{2}{N} \int \frac{d^3 k}{(2\pi)^3} \frac{\gamma^\mu (C_\Psi \gamma^\alpha k_\alpha + C_m) \gamma^\nu}{(C_\Psi^2 k^2 + C_m^2) \Pi(q^2)} \left(g_{\mu\nu} - \eta \frac{q_\mu q_\nu}{q^2} \right), \end{aligned} \quad (5.4.7)$$

where $q = p - k$. We also performed a transformation to the Euclidean space ($k_0 \rightarrow ik_0^E$).

By taking the trace over γ -matrices in Eq. (5.4.7), we obtain two coupled equations: one related to the renormalization of the fermion wavefunction and another related to the generation of the fermionic mass. Within the non-local gauge-fixing picture, the fermion wavefunction is not renormalized. This means that $C_\Psi(p^2) = 1$, and it leads to both

$$0 = \frac{2}{N p^2} \int \frac{d^3 k}{(2\pi)^3} \frac{1}{(k^2 + C_m^2) \Pi} \left[(\eta - 1) p \cdot k - 2\eta \frac{(k \cdot q)(p \cdot q)}{q^2} \right], \quad (5.4.8)$$

and

$$C_m = \frac{2}{N} \int \frac{d^3 k}{(2\pi)^3} \frac{C_m (3 - \eta)}{(k^2 + C_m^2) \Pi}, \quad (5.4.9)$$

where Eq. (5.4.8) is used to determine $\eta(q^2)$. After some calculations, one finds that in the massless gauge boson limit $\tau_N \rightarrow \infty$, $\eta = 1/3$ is a constant (see Sec. 5.C for details). Within the Schwinger-Dyson equations, this limit is only defined for a nonzero polarization-tensor contribution, i.e. $\Pi(q^2) \neq 0$, as seen in Eq. (5.4.9). Hence, the *quenched* approximation $\Pi(q^2) = 0$ sometimes used in the literature [110] to simplify calculations can only be used here in the case of a massive gauge boson.

We proceed with the computation by considering the massless gauge boson limit with $\eta = 1/3$, which yields

$$C_m = \frac{128}{3N} \int \frac{d^3k}{(2\pi)^3} \frac{C_m}{(k^2 + C_m^2) \sqrt{(p-k)^2}}, \quad (5.4.10)$$

where we used $\Pi(q^2) = \sqrt{q^2}/8$. The integrals over k in Eq. (5.4.10) are performed in spherical coordinates. We first integrate over the solid angle, and then split the remaining integral over positive values of k into two regions,

$$C_m = \frac{64}{3\pi^2 N} \left\{ \int_0^p dk \frac{k^2 C_m(k^2)}{k^2 + C_m^2(k^2)} \frac{1}{|p|} + \int_p^\Lambda dk \frac{k^2 C_m(k^2)}{k^2 + C_m^2(k^2)} \frac{1}{|k|} \right\}, \quad (5.4.11)$$

where the virtual-momentum k is, respectively, less or greater than the external momentum p . Here, Λ is a cutoff and $p = |p|$. Now, we transform the integral Eq. (5.4.11) into a differential equation, and by considering $p^2 + C_m^2(p^2) \approx p^2$, we obtain

$$p^2 \frac{d^2 C_m}{dp^2} + 2p \frac{dC_m}{dp} + \frac{64}{3\pi^2 N} C_m = 0. \quad (5.4.12)$$

The solution of Eq. (5.4.12) reads

$$C_m(p) = \sqrt{\frac{m}{p}} \left[C_1 \cos \left(\lambda \ln \frac{p}{m} \right) + i C_2 \sin \left(\lambda \ln \frac{p}{m} \right) \right], \quad (5.4.13)$$

where we have introduced the infrared parameter m such that the ratio p/m is dimensionless and the solution obeys the normalization condition $C_m(p = m) = m$. C_1 and C_2 are coefficients to be determined according to the ultraviolet (UV) and infrared (IR) boundary conditions. The parameter λ indicates the behavior of the solutions of Eq. (5.4.12), and it is given by

$$\lambda = \frac{1}{2} \sqrt{\frac{256}{3\pi^2 N} - 1}. \quad (5.4.14)$$

We see in Eq. (5.4.14) that there is a critical value $N_c = 256/3\pi^2 \approx 8.6$ determining the point at which the solution changes from oscillatory to exponential. This critical number is twice the one in QED₂₊₁ with a non-local gauge fixing. For values of $N > 256/3\pi^2$, the solutions in Eq. (5.4.13) are real exponentials, with a contribution that increases in the UV limit. Hence, the only possible solution in this regime is $C_m(p) = 0$ (trivial solution; no mass generation) [114]. For $N < 256/3\pi^2$, we obtain the oscillatory solutions (5.4.13). This implies that $C_m(p) \neq 0$, and consequently, the chiral symmetry has been broken by the dynamical generation of a

fermion mass.

The IR and UV boundary conditions are, respectively,

$$\left[\frac{dC_m(p)}{dp} \right]_{p=m} = 0, \text{ and } \left[p \frac{dC_m(p)}{dp} + C_m(p) \right]_{p=\Lambda} = 0. \quad (5.4.15)$$

The IR condition yields a relation between the coefficients C_1 and C_2 , $C_1 = 2i\lambda C_2$. By using this result in the UV condition, we obtain an expression for m

$$m = \Lambda \exp \left[-\frac{1}{\lambda} \arctan \left(\frac{4\lambda}{4\lambda^2 - 1} \right) \right]. \quad (5.4.16)$$

The solution (5.4.13) can be rewritten as

$$C_m(p) = m \mathcal{F} \left(\frac{p}{m}, \lambda \right), \quad (5.4.17)$$

with

$$\mathcal{F} \left(\frac{p}{m}, \lambda \right) = \sqrt{\frac{m}{p}} \left[\cos \left(\lambda \ln \frac{p}{m} \right) + \frac{1}{2\lambda} \sin \left(\lambda \ln \frac{p}{m} \right) \right].$$

So far, we have shown that the Thirring-like interactions derived within the dimensional-reduction method break the chiral symmetry and generate a mass in the fermionic sector with a critical number N_c that is twice the value of the standard Thirring model derived in Ref. [107]. This makes sense in the strong-coupling regime because the contributions of both Thirring-like interactions sum up, yielding the multiplicative factor 2 in Eq. (5.4.7).

5.4.2 Long-range interaction

At last, we investigate the effect of the long-range interaction in the strong-coupling regime. First, we rewrite the long-range interaction of Eq. (5.3.5) in terms of a gauge theory, e.g.

$$\mathcal{U}^{\mu\nu} \frac{1}{\sqrt{\square}} \mathcal{U}_{\mu\nu} + \bar{\tau}_N h_\mu \mathcal{J}^\mu, \quad (5.4.18)$$

where $\mathcal{U}_{\mu\nu} = \partial_\mu h_\nu - \partial_\nu h_\mu$ and $\bar{\tau}_N$ is the coupling constant. This non-local gauge theory is similar to the one studied in Ref. [110], where the authors also showed the breaking of chiral symmetry.

By adding the contribution of the long-range interaction to $\Sigma(p)$ and following a standard procedure, we obtain a differential equation similar to Eq. (5.4.12), but with a different coefficient multiplying the function $C_m(p)$. In other words, we

obtain a different parameter λ , namely

$$\lambda' = \frac{1}{2} \sqrt{\frac{4}{N} \left(\frac{64}{3\pi^2} + \frac{8}{\pi^2} \right)} - 1, \quad (5.4.19)$$

where $32/N\pi^2$ is the long-range contribution. The new parameter λ' leads to a critical number $N_c = 352/3\pi^2 \approx 11.8$. Thus, the difference between the effect caused by the short- and the long-range interaction is mainly associated to the critical number of fermions (or critical coupling) below which the symmetry is dynamically broken.

Our results show that the short-range interaction yields the major contribution to the dynamical mass generation when compared to the long-range one. However, both interaction effects add up in a way to increase the value of the critical fermion flavor N_c for the occurrence of exciton condensation. This dynamical mechanism is driven mainly by the presence of *electronic interactions* between the surfaces of 3D TI thin-films, and is robust only when the surfaces are strongly interacting. The resulting gap is *time-reversal invariant* and represents a signature of excitonic bound states.

5.4.3 Application: Bi₂Se₃ thin-film

Here, we apply our dynamical gap generation results to Bi₂Se₃ thin films. This material is one of the most investigated 3D TIs [27, 115], together with Bi₂Te₃ [116]. Experimentally, the size of the gap depends on the material, on the thickness of the film, and on the substrate where the material is grown. In particular, the width of the sample drives the transition from a trivial insulator to a spin Hall insulator, up to the limit in which the material presents the characteristics of a true 3D TI. This transition has been theoretically and experimentally investigated in Ref. [27].

In our manuscript, to describe these thin films, we adopted the regime where the distance between the surfaces d – the width of the 3D TI – is smaller than the in-plane average separation a between electrons and holes. In general, one would not expect interactions between the surfaces of a 3D TI because of the high values of the bulk dielectric constant. However, the bulk dielectric constant depends on the thickness of the material and decreases for thinner samples [117, 118]. In this limit, the effect of electronic interactions becomes relevant. As we have shown, in the strong coupling regime there is a gap generation in each of the surfaces.

Within these assumptions, by using Eq. (5.4.16) we are able to estimate the excitonic gap generated at zero temperature. This estimative depends on the material and dielectric constant of the substrate via the cutoff Λ , which in the case

of Bi_2Se_3 , for a single Dirac mode ($N = 1$), is 0.1 eV [99]. By considering these parameters, we theoretically estimate $\lambda \simeq 1.65$ and determine the maximum value for the gap, $m \approx 0.07$ eV, arising from the electronic interactions. Interestingly, this value agrees with the gap measured through ARPES for a thin-film thickness of 4 nm in Bi_2Se_3 [27].

5.5 Conclusions

It was theoretically proposed that the excitonic bound states at zero magnetic field may have important technological applications such as for dispersionless switching devices [119], or in the design of topologically protected qubits [120], or in heat exchangers [100]. It is also well known that TI-based electronic devices are attractive as platforms for spintronic applications. In this chapter, we provide further theoretical support for exciton condensation in thin-film 3D TIs by investigating the influence of electromagnetic interactions in these systems.

We started by considering that the photons propagate through the 3D surrounding space where the material is immersed, while the mobile electrons propagate on the two 2D surfaces of the 3D TI. Upon projecting the photon dynamics to these two 2D surfaces, we found the effective intra- and inter-surfaces interaction in the system. The problem was then mapped into a single surface one, in which the top and bottom layers appear as flavors of a single fermionic spinor. Within a single-surface picture, we showed that the fermions interact via two effective short-range and one long-range interaction terms. By using a Hubbard-Stratonovich transformation, we introduced the corresponding effective gauge theory and analyzed the dynamical gap generation through the Schwinger-Dyson equation. This gap term is time-reversal invariant and is associated to the chiral symmetry breaking.

Our results indicate that the combined effect of short- and long-range interactions that emerge from projecting QED enhance the value of the critical fermion flavor number N_c in comparison to models that only include short- or long-range interaction. They also confirm the existence and robustness of excitonic bound states in thin-film TIs in the non-perturbative regime. Notice that these results are achieved in the strongly-coupling regime, which is usually difficult to access with analytic techniques due to the failure of the standard perturbation-theory approach.

The method used here can be extended to multi-layer systems, which involve a larger number of fermion species. This will allow one to analyze the chiral-symmetry breaking and dynamical mass generation in experimentally available samples of multi-layered Dirac materials. At present, the multi-layer samples are of

higher quality than the corresponding single-layer ones, and it is therefore essential that theoretical investigation tackle those more complex, multi-flavor systems. Furthermore, the same method can be used to study lower-dimensional excitonic bound states, which have been recently proposed in two parallel nanowires [121].

5.A Effective interactions after projection

After the projection, we obtain the following interaction terms

$$\begin{aligned} V_{tt} = V_{bb} &= \frac{1}{4\pi^2|r-r'-a|^2}, \\ V_{tb} = V_{bt} &\approx \frac{1}{4\pi^2|r-r'-a|^2} - \frac{d}{2}\delta(r-r'-a). \end{aligned}$$

where $a^2 \approx 0$. By plugging back these results into Eq. (5.2.5), we find

$$\begin{aligned} S_{\text{int}}^{\text{eff}} &= -\frac{e^2}{2} \int d^3r d^3r' j_{t,b}^\mu(r-a/2) \frac{1}{4\pi^2|r-r'-a|^2} j_\mu^{t,b}(r'+a/2) \\ &\quad - \frac{e^2}{2} \int d^3r d^3r' j_{t,b}^\mu(r-a/2) \left[\frac{1}{4\pi^2|r-r'-a|^2} - \frac{d}{2}\delta(r-r'-a) \right] j_\mu^{b,t}(r'+a/2) \\ &= -\frac{e^2}{2} \underbrace{\int d^3r d^3r' j_{t,b}^\mu(r-a/2) \frac{1}{4\pi^2|r-r'-a|^2} j_\mu^{t,b}(r'+a/2)}_{r \rightarrow r+a/2; r' \rightarrow r'-a/2} \\ &\quad - \frac{e^2}{2} \underbrace{\int d^3r d^3r' j_{t,b}^\mu(r-a/2) \frac{1}{4\pi^2|r-r'-a|^2} j_\mu^{b,t}(r'+a/2)}_{r \rightarrow r+a/2; r' \rightarrow r'-a/2} \\ &\quad + \frac{e^2 d}{4} \underbrace{\int d^3r j_{t,b}^\mu(r+a/2) j_\mu^{b,t}(r+a/2)}_{r \rightarrow r-a/2} \\ &= -\frac{e^2}{2} \int d^3r d^3r' j_{t,b}^\mu(r) \frac{1}{4\pi^2|r-r'|^2} j_\mu^{t,b}(r') \\ &\quad - \frac{e^2}{2} \int d^3r d^3r' j_{t,b}^\mu(r) \frac{1}{4\pi^2|r-r'|^2} j_\mu^{b,t}(r') + \frac{e^2 d}{4} \int d^3r j_{t,b}^\mu(r) j_\mu^{b,t}(r). \quad (5.A.1) \end{aligned}$$

5.B Derivation of interactions in Eq. (5.3.5)

Here, we show how to obtain the interaction terms of Eq. (5.3.5) by computing the contribution $j_k^\mu V_{\kappa\rho} j_\mu^\rho$ from Eq. (5.3.1). First, we write down explicitly the elements of this sum,

$$j_\kappa^\mu V_{\kappa\rho} j_\mu^\rho = j_t^\mu V_{tt} j_\mu^t + j_b^\mu V_{tt} j_\mu^b + j_t^\mu V_{tb} j_\mu^b + j_b^\mu V_{tb} j_\mu^t, \quad (5.B.1)$$

where we used that $V_{tt} = V_{bb}$ and $V_{tb} = V_{bt}$, as shown in Sec. 5.2. Notice that there is no sum over t or b , the indexes only label the different flavors. With the fermionic currents defined in Eqs. (5.3.3) and (5.3.4), i.e.

$$\begin{aligned} j_t^\mu &= \frac{1}{2} (\bar{\Psi} \gamma^\mu \Psi - i \bar{\Psi} \gamma^\mu \gamma^3 \gamma^5 \Psi), \\ j_b^\mu &= \frac{1}{2} (\bar{\Psi} \gamma^\mu \Psi + i \bar{\Psi} \gamma^\mu \gamma^3 \gamma^5 \Psi), \end{aligned}$$

we compute individually each of the elements in Eq. (5.B.1),

$$\begin{aligned} j_t^\mu V_{tt} j_\mu^t &= \frac{1}{4} (\bar{\Psi} \gamma^\mu \Psi - i \bar{\Psi} \gamma^\mu \gamma^3 \gamma^5 \Psi) V_{tt} (\bar{\Psi} \gamma_\mu \Psi - i \bar{\Psi} \gamma_\mu \gamma^3 \gamma^5 \Psi) \\ &= \frac{1}{4} (\bar{\Psi} \gamma^\mu \Psi V_{tt} \bar{\Psi} \gamma_\mu \Psi - i \bar{\Psi} \gamma^\mu \Psi V_{tt} \bar{\Psi} \gamma_\mu \gamma^3 \gamma^5 \Psi - i \bar{\Psi} \gamma^\mu \gamma^3 \gamma^5 \Psi V_{tt} \bar{\Psi} \gamma_\mu \gamma^3 \gamma^5 \Psi \\ &\quad - \bar{\Psi} \gamma^\mu \gamma^3 \gamma^5 \Psi V_{tt} \bar{\Psi} \gamma_\mu \gamma^3 \gamma^5 \Psi), \end{aligned} \tag{5.B.2}$$

$$\begin{aligned} j_b^\mu V_{tt} j_\mu^b &= \frac{1}{4} (\bar{\Psi} \gamma^\mu \Psi + i \bar{\Psi} \gamma^\mu \gamma^3 \gamma^5 \Psi) V_{tt} (\bar{\Psi} \gamma_\mu \Psi + i \bar{\Psi} \gamma_\mu \gamma^3 \gamma^5 \Psi) \\ &= \frac{1}{4} (\bar{\Psi} \gamma^\mu \Psi V_{tt} \bar{\Psi} \gamma_\mu \Psi + i \bar{\Psi} \gamma^\mu \Psi V_{tt} \bar{\Psi} \gamma_\mu \gamma^3 \gamma^5 \Psi + i \bar{\Psi} \gamma^\mu \gamma^3 \gamma^5 \Psi V_{tt} \bar{\Psi} \gamma_\mu \gamma^3 \gamma^5 \Psi \\ &\quad - \bar{\Psi} \gamma^\mu \gamma^3 \gamma^5 \Psi V_{tt} \bar{\Psi} \gamma_\mu \gamma^3 \gamma^5 \Psi), \end{aligned} \tag{5.B.3}$$

$$\begin{aligned} j_t^\mu V_{tb} j_\mu^b &= \frac{1}{4} (\bar{\Psi} \gamma^\mu \Psi - i \bar{\Psi} \gamma^\mu \gamma^3 \gamma^5 \Psi) V_{tb} (\bar{\Psi} \gamma_\mu \Psi + i \bar{\Psi} \gamma_\mu \gamma^3 \gamma^5 \Psi) \\ &= \frac{1}{4} (\bar{\Psi} \gamma^\mu \Psi V_{tb} \bar{\Psi} \gamma_\mu \Psi + i \bar{\Psi} \gamma^\mu \Psi V_{tb} \bar{\Psi} \gamma_\mu \gamma^3 \gamma^5 \Psi - i \bar{\Psi} \gamma^\mu \gamma^3 \gamma^5 \Psi V_{tb} \bar{\Psi} \gamma_\mu \Psi \\ &\quad + \bar{\Psi} \gamma^\mu \gamma^3 \gamma^5 \Psi V_{tb} \bar{\Psi} \gamma_\mu \gamma^3 \gamma^5 \Psi), \end{aligned} \tag{5.B.4}$$

$$\begin{aligned} j_b^\mu V_{tb} j_\mu^t &= \frac{1}{4} (\bar{\Psi} \gamma^\mu \Psi + i \bar{\Psi} \gamma^\mu \gamma^3 \gamma^5 \Psi) V_{tb} (\bar{\Psi} \gamma_\mu \Psi - i \bar{\Psi} \gamma_\mu \gamma^3 \gamma^5 \Psi) \\ &= \frac{1}{4} (\bar{\Psi} \gamma^\mu \Psi V_{tb} \bar{\Psi} \gamma_\mu \Psi - i \bar{\Psi} \gamma^\mu \Psi V_{tb} \bar{\Psi} \gamma_\mu \gamma^3 \gamma^5 \Psi + i \bar{\Psi} \gamma^\mu \gamma^3 \gamma^5 \Psi V_{tb} \bar{\Psi} \gamma_\mu \Psi \\ &\quad + \bar{\Psi} \gamma^\mu \gamma^3 \gamma^5 \Psi V_{tb} \bar{\Psi} \gamma_\mu \gamma^3 \gamma^5 \Psi). \end{aligned} \tag{5.B.5}$$

Now, by summing the results of Eqs. (5.B.2), (5.B.3), (5.B.4) and (5.B.5), we obtain

$$\begin{aligned} j_\kappa^\mu V_{\kappa\rho} j_\mu^\rho &= \frac{1}{2} (\bar{\Psi}\gamma^\mu\Psi V_{\text{tt}}\bar{\Psi}\gamma_\mu\Psi - \bar{\Psi}\gamma^\mu\gamma^3\gamma^5\Psi V_{\text{tt}}\bar{\Psi}\gamma_\mu\gamma^3\gamma^5\Psi) \\ &+ \frac{1}{2} (\bar{\Psi}\gamma^\mu\Psi V_{\text{tb}}\bar{\Psi}\gamma_\mu\Psi + \bar{\Psi}\gamma^\mu\gamma^3\gamma^5\Psi V_{\text{tb}}\bar{\Psi}\gamma_\mu\gamma^3\gamma^5\Psi), \\ &= \frac{1}{2} (\mathcal{J}^\mu V_{\text{tt}}\mathcal{J}_\mu - \mathcal{J}_{35}^\mu V_{\text{tt}}\mathcal{J}_\mu^{35}) + \frac{1}{2} (\mathcal{J}^\mu V_{\text{tb}}\mathcal{J}_\mu + \mathcal{J}_{35}^\mu V_{\text{tb}}\mathcal{J}_\mu^{35}), \end{aligned} \quad (5.B.6)$$

where $\mathcal{J}^\mu = \bar{\Psi}\gamma^\mu\Psi$ and $\mathcal{J}_{35}^\mu = \bar{\Psi}\gamma^\mu\gamma^3\gamma^5\Psi$. The last step is to substitute the interactions,

$$V_{\text{tt}} = \frac{1}{4\pi^2|r-r'|^2}$$

and

$$V_{\text{tb}} \approx \frac{1}{4\pi^2|r-r'|^2} - \frac{d}{2}\delta(r-r')$$

into Eq. (5.B.6), to find

$$j_\kappa^\mu V_{\kappa\rho} j_\mu^\rho = -\frac{d}{4} [\mathcal{J}^\mu\delta(r-r')\mathcal{J}_\mu + \mathcal{J}_{35}^\mu\delta(r-r')\mathcal{J}_\mu^{35}] + \mathcal{J}^\mu \frac{1}{4\pi^2|r-r'|^2} \mathcal{J}_\mu. \quad (5.B.7)$$

It is straightforward to check that by replacing Eq. (5.B.7) into Eq. (5.3.1), one finds the interactions terms of Eq. (5.3.5).

5.C η -function in the strong coupling regime

By rewriting Eq. (5.4.8) of the main text in spherical coordinates, we obtain

$$0 = \frac{1}{Np^2} \int_0^\infty \frac{k^2 dk}{(2\pi)^2} \frac{1}{k^2 + C_m^2} \int_0^\pi d\theta \sin\theta [f_1(q^2, k^2, p^2) \cos\theta - f_2(q^2, k^2, p^2) \sin^2\theta], \quad (5.C.1)$$

where

$$f_1(q^2, k^2, p^2) \equiv \tilde{G}_0(q^2)(\eta + 1)\sqrt{k^2 p^2}$$

and

$$f_2(q^2, k^2, p^2) \equiv \frac{\tilde{G}_0(q^2)2\eta k^2 p^2}{q^2}.$$

Here, we denote $\tilde{G}_0 = \lim_{\tau_N \rightarrow \infty} G_0$, in the massless gauge boson limit. Now, we integrate by parts the first integral over θ in Eq. (5.C.1), which yields

$$\int_0^\pi d\theta \sin\theta \cos\theta f_1 = - \int_0^\pi d\theta \sin^3\theta \frac{d\tilde{f}_1}{dq^2}, \quad (5.C.2)$$

where we used that $q^2 = p^2 + k^2 - 2\sqrt{k^2 p^2} \cos \theta$ and $\tilde{f}_1 = \sqrt{k^2 p^2} f_1$. Replacing the result (5.C.2) into Eq. (5.C.1), we find

$$0 = \frac{1}{N} \int_0^\infty \frac{dk}{(2\pi)^2} \frac{k^4}{k^2 + C_m^2} \int_0^\pi d\theta \sin^3 \theta \left\{ \frac{d[(\eta + 1)\tilde{G}_0]}{dq^2} + \frac{2\eta\tilde{G}_0}{q^2} \right\}, \quad (5.C.3)$$

with

$$\frac{d[(\eta + 1)\tilde{G}_0]}{dq^2} + \frac{2\eta\tilde{G}_0}{q^2} = \frac{1}{q^4} \left[\frac{d(\eta\tilde{G}_0 q^4)}{dq^2} + q^4 \frac{d\tilde{G}_0}{dq^2} \right].$$

Thus, η satisfies the following differential equation

$$d(\eta\tilde{G}_0 q^4) = -q^4 \frac{d\tilde{G}_0}{dq^2} dq^2,$$

and

$$\eta(q^2) = \frac{2}{\tilde{G}_0(q^2)q^4} \int_0^{q^2} \tilde{G}_0(\zeta^2)\zeta^2 d\zeta^2 - 1 = \frac{2\Pi(q^2)}{q^4} \int_0^{q^2} \frac{\zeta^2}{\Pi(\zeta^2)} d\zeta^2 - 1 = \frac{1}{3}, \quad (5.C.4)$$

where $\Pi(q^2) = \sqrt{q^2}/8$.

EMERGENT HELICAL LUTTINGER LIQUID IN 2D TOPOLOGICAL INSULATORS FROM ELECTROMAGNETIC INTERACTIONS

It has been shown that local four-fermion interactions on the edges of 2D time-reversal-invariant TIs give rise to a new non-Fermi-liquid phase, called helical Luttinger liquid (HLL). In this chapter, we provide a first-principle derivation of this HLL based on the gauge-theory approach. We start by considering massless Dirac fermions confined on the 1D boundary of the TI and interacting through a 3D quantum dynamical electromagnetic field. Within these assumptions, through a dimensional-reduction procedure, we derive the effective (1+1)D interacting fermionic theory and reveal its underlying gauge theory. In the low-energy regime, the gauge theory that describes the edge states is given by a conformal QED, which can be mapped exactly into a HLL with a Luttinger parameter and a renormalized Fermi velocity that depend on the value of the fine-structure constant α .

Note: This chapter is based in Ref. [102], where I contributed by performing all the calculations of the work.

6.1 Introduction

TIs represent a large family of materials characterized by gapped bulks and metallic edge states. The spin-orbit interaction locks the spin and the chirality together and produces counter-propagating edge currents, giving rise to the QSHE. These topologically protected edge modes are right-handed and left-handed Dirac modes

that always come in pairs, in agreement with the time-reversal symmetry of the bulk. Their dynamics is consistently described by a (1+1)D massless Dirac theory.

Due to the 1D nature of the edges, local four-fermion interactions on the edge may transform the free-fermion phase into a new non-Fermi-liquid phase, known as the HLL[122, 123]. In this picture, the strength of the interactions is encoded in the Luttinger parameter K_L , which depends on the value of the coupling constant ρ of the four-fermion term. Although many studies have pointed out for which values of K_L the interactions are relevant, it is still unclear how the constant ρ is related to the microscopic properties of the Dirac edge modes, such as their spin, electric charge, etc. The relevant open question is whether there is any fundamental way to derive the HLL from the universal properties of TIs.

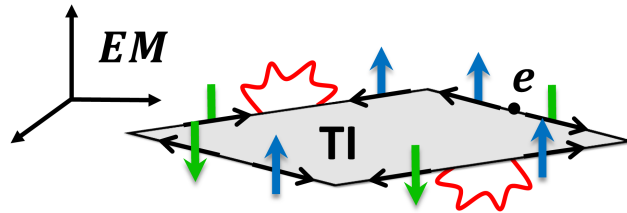


Figure 6.1: The red wavy lines represent the virtual photons that are free to propagate in all the 3D, while the massless Dirac fermions with electric charge e are confined on the 1D boundary of the TI. The arrows at the edges indicate the propagation of the topologically protected right- and left-handed chiral modes.

The main goal of the work presented in chapter is to provide an answer to this question. Firstly, we consider massless Dirac fermions constrained in 1D (the boundary), while the quantum excitations (i.e. the virtual photons) of the $U(1)$ gauge field are free to propagate in all the 3D that represent the physical space where the TI is embedded, see Fig. 6.1. From this assumption, we derive the interacting fermionic theory for the edge states of 2D time-reversal-invariant TIs. By using a Hubbard-Stratonovich transformation, we determine the effective (1+1)D gauge theory that mediates the fermionic interaction, which is given by the sum of a CQED [124, 125] plus the (1+1)D massless QED, also known as the Schwinger model [126, 127].

In this chapter, we focus on the CQED because it describes a massless mode along the whole edge and is dominant in the low-energy regime. It also preserves the dimensionality of both, the electric charge and the gauge field of the (3+1)D QED from which the CQED will be derived by using a dimensional reduction procedure. This method has been already used in studies of graphene [56, 67] and related 2D massive Dirac systems, such as silicene and transition metal dichalcogenides [101], but to the best of our knowledge, it has not yet been employed in

the description of 1D systems, such as the edge currents of TIs. Notice that in Ref. [46], a projection of QED in (3+1)D to a (1+1)D-brane was performed. However, a finite-size regulator was introduced to avoid ultraviolet divergences that appear when confining the system to 1D. Therefore, the effective theory obtained is not scale invariant and cannot be conformal. In our approach, we found an explicit way to deal with the divergences, such that we obtain the CQED without any regulator. Furthermore, by integrating out the CQED gauge field in the corresponding partition function, we find that this gauge theory gives rise to a (1+1)D Thirring model [128]. We then demonstrate that the bosonized version of the interacting-fermion Hamiltonian describes exactly a HLL with a Luttinger parameter K_L and a renormalized Fermi velocity that depend on the value of the fine-structure constant α .

6.2 Conformal QED on the boundary of topological insulators

We start by considering 2D time-reversal invariant TIs in class AII [31], which have a gapped bulk and topologically protected Dirac edge modes. These systems realize the QSHE, i.e. the chirality of the Dirac edge modes is locked to the spin, which is preserved due to the time-reversal symmetry. Thus, the dynamics of the edge modes can be described by a (1+1)D massless Dirac theory with a two-component Dirac spinor $\psi = (\psi_R, \psi_L)^T$, where ψ_R and ψ_L are the right-handed spin-up and left-handed spin-down chiral modes, respectively. It was theoretically proposed in Refs. [122, 123] and experimentally confirmed in Ref. [129] that these TIs can support HLLs on the boundary due to the presence of unavoidable electron-electron interactions. These non-Fermi liquid phases fully preserve the time-reversal symmetry and are formally described by the free Dirac theory plus suitable four-fermion interactions. We now show that this model and the corresponding HLL can be derived from a gauge theory by simply assuming that the electrically charged propagating Dirac fermions on the edge interact through a quantum dynamical electromagnetic field A_ρ . The essential point of our approach is that the massless Dirac fermions are confined on the 1D boundary, whereas the quantum excitations (i.e. photons) of the electromagnetic field are free to propagate in all the 3D, as shown in Fig. 6.1. The corresponding covariant QED action reads

$$S_{\text{QED}}[A_\rho, \bar{\psi}, \psi] = i\hbar \int d^2r \bar{\psi} \gamma^\mu \partial_\mu \psi - \int d^4r \left(\frac{\epsilon_0 c}{4} F_{\rho\beta} F^{\rho\beta} + e j_{3+1}^\rho A_\rho \right), \quad (6.2.1)$$

where $d^2r = v_F dx dt$ and $d^4r = c dx dy dz dt$. Here, γ^μ are 2×2 Dirac/Pauli matrices with $\mu = 0, 1$ and $\{\gamma^\nu, \gamma^\mu\} = 2g^{\mu\nu}$, $F_{\rho\beta} = \partial_\rho A_\beta - \partial_\beta A_\rho$ is the field-strength tensor, $j_{3+1}^\rho = \bar{\psi}\gamma^\rho\psi$, and $\bar{\psi} = \psi^\dagger\gamma^0$ with $\rho, \beta = 0, 1, 2, 3$. The effective interaction felt by the massless Dirac fermions due to the gauge field can be obtained by integrating out the A_ρ -field in the partition function \mathcal{Z} , i.e.

$$\mathcal{Z} = \int \mathcal{D}\bar{\psi} \int \mathcal{D}\psi \int \mathcal{D}A_\rho \exp\left(\frac{i}{\hbar} S_{\text{QED}}\right) = \int \mathcal{D}\bar{\psi} \int \mathcal{D}\psi \exp\left(\frac{i}{\hbar} S_{\text{eff}}[\bar{\psi}, \psi]\right), \quad (6.2.2)$$

where $S_{\text{eff}} = S_D + S_{\text{int}}$ is the effective action, with S_D the free Dirac action, given by the first term in Eq. (6.2.1), and S_{int} the interaction term, given by

$$S_{\text{int}} = -\frac{e^2}{2\varepsilon_0 c} \int d^4r d^4r' j_{3+1}^\rho(r) \frac{1}{(-\square)} j_\rho^{3+1}(r'), \quad (6.2.3)$$

where we performed a Wick rotation and \square is the d'Alembertian operator in the Euclidean space. Now, by imposing a constraint on the matter current,

$$j_{3+1}^\rho(t, x, y, z) = j_{1+1}^\mu(t, x)\delta(y)\delta(z), \quad (6.2.4)$$

we create the dimensional mismatch between the Dirac fermions and the virtual photons, preserving the (3+1)D character of the electromagnetic field. Hence, by inserting Eq. (6.2.4) into Eq. (6.2.3), we get

$$S_{\text{int}} = -\frac{e^2}{2\varepsilon_0 c} \int d^2r d^2r' j_{1+1}^\mu(r) \left[\frac{1}{(-\square)} \right]_{**} j_\mu^{1+1}(r'), \quad (6.2.5)$$

where the symbol $**$ means that we need to evaluate the Green's function at $y = y' = 0$ and $z = z' = 0$. To evaluate Eq. (6.2.5), we first write the Fourier transform of the Green's function

$$\frac{1}{(-\square)} = -\square \int \frac{d^4k}{(2\pi)^4} \frac{e^{ik \cdot (r-r')}}{(k^2)^2}, \quad (6.2.6)$$

where $\square = \partial_t^2 + \partial_x^2 + \partial_y^2 + \partial_z^2$ acts on the coordinates. We integrate over the momenta k and then impose the above constraints on the coordinates, to eventually find (see Sec. 6.A)

$$\left[\frac{1}{(-\square)} \right]_{**} = \frac{1}{2\pi} \delta(x-x')\delta(t-t') + \frac{1}{4\pi^2} \frac{1}{\square_{1+1}}, \quad (6.2.7)$$

where $\delta(x-x')$ and $\delta(t-t')$ are two Dirac delta functions and \square_{1+1} is the d'Alembertian in (1+1)D. Notice that in Refs. [46, 130], a finite-size regulator

for the Dirac delta function in Eq. (6.2.4) was introduced. This result agrees with ours in the limit when the finite-size regulator is removed.

The replacement of the terms in Eq. (6.2.7) in the effective interaction (6.2.5) leads to

$$S_{\text{int}} = -\frac{e^2}{4\pi\varepsilon_0 c} \int d^2 r j_{1+1}^\mu(r) j_\mu^{1+1}(r) - \frac{e^2}{8\pi^2\varepsilon_0 c} \int d^2 r' d^2 r j_{1+1}^\mu(r) \frac{1}{\square_{1+1}} j_\mu^{1+1}(r'). \quad (6.2.8)$$

By using a Hubbard-Stratonovich transformation, we rewrite individually each Gaussian-type interaction in Eq. (6.2.8) in terms of new and independent auxiliary (1+1)D gauge fields \mathcal{A}_μ^a (with $a = 1, 2$), and obtain

$$\begin{aligned} S[\mathcal{A}_\mu^a, \bar{\psi}, \psi] &= \int d^2 r \left(i\hbar \bar{\psi} \gamma^\mu \partial_\mu \psi - e j_{1+1}^\mu \mathcal{A}_\mu^1 - \frac{\pi\varepsilon_0 c}{2} F_{\mu\nu}^1 \frac{1}{\square_{1+1}} F_1^{\mu\nu} \right. \\ &\quad \left. - \bar{e} j_{1+1}^\mu \mathcal{A}_\mu^2 - \pi^2 \varepsilon_0 c F_{\mu\nu}^2 F_2^{\mu\nu} \right), \end{aligned} \quad (6.2.9)$$

which replaces the action (6.2.1) and represents the main result of this chapter. By integrating out the \mathcal{A}_μ^a -fields in Eq. (6.2.9) one obtains, besides the free Dirac action, exactly the interacting terms given by Eq. (6.2.8) (see Sec. 6.B for details). From our result (6.2.9) we can derive two well-known exactly solvable models in (1+1)D: by integrating out the \mathcal{A}_μ^1 -field, we obtain the Thirring model [128], whereas the Lagrangian for the \mathcal{A}_μ^2 -field can be identified with the Schwinger model [126, 131]. The pseudo-differential operator in the kinetic term of the \mathcal{A}_μ^1 -field determines its dimensionality, such that the coupling constant e remains dimensionless, while $\bar{e} = e\Lambda$ is a dimensionful bare constant and Λ has a mass dimension (see Sec. 6.B for more details).

It is known that the Schwinger-Thirring model leads to a massless and a massive bosonic mode [132, 133]. However, in the low-energy limit, i.e. $k \ll ev_F\Lambda$, only the former describes a propagating mode along the whole edge. The massive mode is localized and may be accessed only at higher values of the energy. Moreover, this massless bosonic mode reveals the critical – zero mass – nature of the original fermion. From now on, by focusing on the low-energy regime, we proceed our analysis by neglecting the contribution from the massive \mathcal{A}_μ^2 -field.

We want to emphasize that the dimensional reduction procedure performed here has been already employed in the study of 2D materials, such as graphene. In this case, the corresponding effective field theory is the so-called Pseudo QED (PQED) [45, 49], i.e., a (2+1)D QED with higher-order derivatives in the Maxwell term (see Table I). When electrons are confined in (1+1)D, the non-local (higher derivative) Maxwell term of the effective theory in Eq. (6.2.9) leads to a conformal theory when $c = v_F$ [124, 125]. Importantly, both time-reversal and conformal symmetries are relevant in the identification of the right interacting phase of the

TI in the low-energy regime. Thus, because the boundary of a 2D non-interacting TI is described by a free conformal field theory defined in terms of a 1D Dirac theory, we will consider the conformal fixed point ($c = v_F$) even for the interacting phase by deriving the corresponding HLL in the following section. This CQED shares some properties with PQED. In fact, in both theories the electric charge e is a dimensionless parameter, as in usual (3+1)D QED. The fact that the coupling constant remains dimensionless makes perturbative studies more reliable. Moreover, just like in the Luttinger-liquid case, in PQED and in CQED the excitations are collective modes and there are no quasi-particles because the Green's function has branch cuts instead of poles [130].

U(1) gauge theories	Bosonic Lagrangians
1+1 CQED	$-\frac{\pi}{2} F_{\mu\nu} (\square_{1+1})^{-1} F^{\mu\nu}$
2+1 PQED	$-\frac{1}{2} F_{\mu\nu} (\square_{2+1})^{-1/2} F^{\mu\nu}$
3+1 QED	$-\frac{1}{4} F_{\mu\nu} F^{\mu\nu}$

Table 6.1: The bosonic sector of the QED, PQED and CQED in the second column for $\varepsilon_0 = c = 1$. In lower dimensions, the Maxwell theory is replaced by suitable versions that contain pseudo-operators, i.e. $(\partial^2)^{-\vartheta}$ with $\vartheta = 1$ or $1/2$, to adjust and preserve the dimensionality of the coupling constant $[e] = 1$. This means that QED, PQED and CQED are renormalizable theories.

6.3 Thirring model and helical Luttinger liquid

Here, we derive in a straightforward way the HLL from our effective field-theory model. The fermionic kinematical term in Eq. (6.2.1), together with the local interaction term in Eq. (6.2.8), allow us to write the purely effective fermionic action

$$S_{1+1}^{\text{eff}} = \int d^2r \left[i\hbar \bar{\psi} \gamma^\mu \partial_\mu \psi - \varrho (\bar{\psi} \gamma^\mu \psi)^2 \right], \quad (6.3.1)$$

which can be recognized as the massless Thirring model [128], with the coupling constant $\varrho = e^2/4\pi\varepsilon_0c$. The corresponding Hamiltonian is then calculated by employing a Legendre transformation,

$$H_{\text{eff}} = v_F \int dx \left[i\hbar \left(\psi_R^\dagger \partial_x \psi_R - \psi_L^\dagger \partial_x \psi_L \right) + \frac{e^2}{\pi\varepsilon_0c} \psi_R^\dagger \psi_R \psi_L^\dagger \psi_L \right], \quad (6.3.2)$$

where the interaction term is nothing but the forward scattering, and we have used the chiral basis with $\psi = (\psi_R, \psi_L)^T$, with the fermion operators satisfying usual anti-commutation relations. The bosonization of Eq. (6.3.2) is straightforward

[134] (a detailed calculation is shown Sec. 6.C), and we obtain

$$H_{\text{eff}}^{\text{bos}} = \tilde{v}_F \int dx \left[\frac{1}{K_L} (\partial_x \varphi)^2 + K_L (\partial_x \theta)^2 \right], \quad (6.3.3)$$

which is the HLL Hamiltonian, with the scalar fields $\varphi = (\phi_R + \phi_L)/\sqrt{2}$ and $\theta = (\phi_R - \phi_L)/\sqrt{2}$. Here, the bosonization rules read

$$\psi_R = \frac{1}{\sqrt{2\pi}} e^{-i\sqrt{4\pi}\phi_R}, \quad \psi_L = \frac{1}{\sqrt{2\pi}} e^{i\sqrt{4\pi}\phi_L}, \quad (6.3.4)$$

with the Luttinger parameter K_L and the renormalized velocity \tilde{v}_F respectively given by

$$K_L = \sqrt{\left(1 - \frac{2\alpha}{\pi}\right) \left(1 + \frac{2\alpha}{\pi}\right)^{-1}}, \quad (6.3.5)$$

$$\tilde{v}_F = \hbar v_F \sqrt{1 - \frac{4\alpha^2}{\pi^2}}, \quad (6.3.6)$$

where $\alpha \equiv e^2/4\pi\hbar\varepsilon v_F$ is a measure of the strength of the electron-electron interaction, also known as the fine-structure constant. Because α is an observable that depends on the material, i.e. on the dielectric constant of the medium, $\varepsilon = \varepsilon_G \varepsilon_0$ and v_F is the velocity of the fermions when they propagate in this material. Thus, due to gauge principle and to the projection from QED to CQED, we have been able to derive the HLL on the boundary of the TI. Moreover, we have determined the value of the Luttinger parameter and the renormalized velocity, which depend, in our framework, only on the generic properties of the Dirac modes, i.e. the value of their electric charge, the Fermi velocity and the dielectric constant by means of the fine-structure constant α .

6.4 Luttinger-parameter discussion

The parameter K_L in the HLL defines different regimes of the interaction, which changes from repulsive ($K_L < 1$), passing through non-interacting ($K_L = 1$), to attractive ($K_L > 1$) [135]. Nonetheless, how this parameter relates to fundamental properties of the materials was still unclear. In Refs. [136, 137], a formula that connects K_L with α is derived by employing perturbation theory with either the Kondo or the backscattering interaction. Here, we have presented a gauge-principle derivation of the Luttinger parameter, which is found to depend on the strength of the electron-electron interaction α .

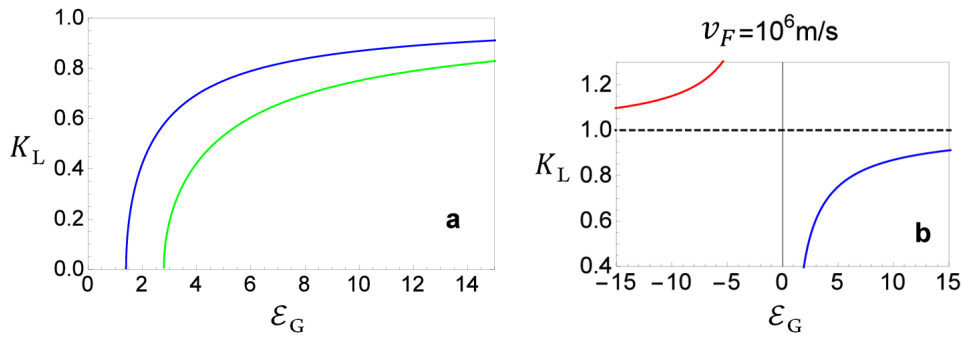


Figure 6.2: (Color online) Luttinger parameter K_L dependence on the dielectric constant ε_G for fixed values of the Fermi velocity v_F . (a) The blue (black) and green (grey) curves are for $v_F = 10^6 \text{m/s}$ and $v_F = 5 \times 10^5 \text{m/s}$, respectively, and they indicate that for sufficiently large values of ε_G , the system becomes non-interacting ($K_L = 1$), while for smaller values of ε_G the interaction is repulsive ($K_L < 1$). (b) A proposal to obtain attractive interactions $K_L > 1$ by changing the sign of the dielectric constant (red/grey curve) for a sample with $v_F = 10^6 \text{m/s}$.

Now, we compare our results with a prior theoretical prediction proposed in Refs. [136, 137], $K_L = \left[1 + (8\alpha/\pi) \ln(\tilde{d}/\ell)\right]^{-1/2}$. Here, \tilde{d} is the distance from the quantum wells to a closeby metallic gate, and ℓ acts as a cutoff for short distances. This dependence of the parameter K_L on α was obtained at the level of perturbation theory on the HLL Hamiltonian, i.e. additional interaction terms had to be taken into account, such as the Kondo or the backscattering interaction. Although our approach is non-perturbative, there are implicit approximations based on the theoretical description of the edge states in terms of QED. The presence of metallic gates in realistic experiments, for instance, could have crucial influence on the field lines of the virtual photons and would modify the effective action in a non-trivial way. Using the values of the parameters reported experimentally for HgTe quantum wells, $v_F \approx 5.5 \times 10^5 \text{ m/s}$ [22, 138], $\varepsilon_G = 15$ [137, 139], $d = 150 \text{ nm}$ and $\ell = \max\{30, 12\} \text{ nm}$ [129], the authors in Ref. [137] find $K_L \approx 0.8$. Within our model, which depends only on α , we obtain $K_L \approx 0.84$.

Notice that our approach does not involve the backscattering term, which induces further corrections to the parameter K_L , as seen in the case of InAs/GaSb quantum wells [129]. This implies that our theoretical prediction applies to materials that have weak backscattering and high Fermi velocities, such as HgTe [140]. Nevertheless, the backscattering term can be obtained within our approach upon considering the *massive* Thirring model. The corresponding bosonization is discussed in the Sec. 6.D with the Klein factors defined as in Ref. [141]. Other possible 2D TIs that would be good candidates to test our theoretical proposal

are plumbene monolayers [142] and germanene films [143]. The Fermi velocity in these materials has the same order of magnitude as that in HgTe, indicating that backscattering might not be so relevant.

Furthermore, we show how to tune K_L in order to obtain different regimes of interaction. From Eq. (6.3.5), we notice that to change K_L we can either change v_F or the dielectric constant of the medium. In Fig. 6.2 **a**, we depict the dependence of K_L on the dielectric constant ε_G in the range [1-15], for a fixed velocity $v_F = 10^6$ m/s. In the asymptotic limit where $\varepsilon_G \rightarrow \infty$ (meaning that we are considering very large values of the dielectric constant, not a mathematical infinity), it would be possible to reach the value of $K_L = 1$. For smaller velocities v_F , the minimum value of the dielectric constant for which K_L becomes real increases, i.e., for $v_F = 5 \times 10^5$ m/s, e.g., $\varepsilon_G^{\min} \approx 2.7$, instead of $\varepsilon_G^{\min} \approx 1.4$ for $v_F = 10^6$ m/s. On the other hand, if we consider negative values of the dielectric constant by placing the TI on top of a meta-material, then it is possible to switch from repulsive to attractive interactions, i.e., $K_L(x) \rightarrow K_L(-|x|) = \sqrt{(1+|x|)/(1-|x|)}$ with $x = 2\alpha/\pi$. We illustrate this situation in Fig. 6.2 **b**. The dielectric constant of the medium here plays the same role of Feshbach resonances in ultracold atoms, which allow to tune the interaction parameter from the repulsive to the attractive regime [144].

6.5 Conclusions

In this chapter, we derived a gauge theory on the boundary of 2D time-reversal-invariant TIs. Our starting point was to assume that the interactions between the charged 1D Dirac fermions at the edge are mediated by a quantum dynamical electromagnetic field, where the virtual photons are free to propagate in all the 3D. By implementing a dimensional-reduction procedure, we derived the corresponding CQED, which describes the HLL. We emphasize that our approach is non-perturbative, and has a more vast applicability in condensed-matter physics. Indeed, the 1D effective theory derived here also works in the case of nanowires deposited on a substrate, in which the HLL phase can be easily obtained [145, 146], as done for TIs.

In our work, we provide a field-theory derivation of the Thirring model, which opens the path to the manipulation of the Luttinger parameter K_L by modifying the dielectric constant of the substrate on which the 1D system might be deposited. Interestingly, we find that upon the use of a meta-material as a substrate, it is possible to change the interactions from repulsive into attractive. These results might have profound implications for transport properties in nanostructures in particular, and nanotechnology in general.

6.A Details on the projection from (3+1)D to (1+1)D

Here, we show the detailed calculation starting from Eq. (6.2.6) to obtain Eq. (6.2.7) in Sec. 6.2. The Fourier transform of the photon propagator reads

$$\frac{1}{(-\square)} = \int \frac{d^4 k}{(2\pi)^4} \frac{e^{ik \cdot (r-r')}}{k^2}, \quad (6.A.1)$$

where $k^2 = k_x^2 + k_y^2 + k_z^2 + \omega^2$. First, we apply the constraint only on the z -component ($z = z' = 0$) and integrate Eq. (6.A.1) over k_z to obtain

$$\left[\frac{1}{(-\square)} \right]_* = \frac{1}{2} \int \frac{d^3 k}{(2\pi)^3} \frac{e^{ik(r-r')}}{\sqrt{k^2}}, \quad (6.A.2)$$

which is the known result of PQED [45]. The symbol $*$ means that we already imposed one of the constraints in the interaction term. Now, if one tries to follow the same steps and integrates over k_y , after applying the constraints on the y -component ($y = y' = 0$), the integral does not converge unless a cutoff is introduced. However, since our goal is to derive a conformal theory, we do not intend to introduce a new scaling in the theory by means of a cutoff.

We present an alternative way to solve this problem by rewriting Eq. (6.A.2) as

$$\begin{aligned} \left[\frac{1}{(-\square)} \right]_* &= -\frac{\square}{2} \int \frac{d^3 k}{(2\pi)^3} \frac{e^{ik(r-r')}}{(k^2)^{3/2}} \\ &= -\frac{\square}{4\pi} \int \frac{d^2 k}{(2\pi)^2} e^{ik_x(x-x') + i\omega(t-t')} \int_{-\infty}^{\infty} dk_y \frac{e^{ik_y(y-y')}}{(k_x^2 + k_y^2 + \omega^2)^{3/2}}, \end{aligned} \quad (6.A.3)$$

where $\square = \partial_t^2 + \partial_x^2 + \partial_y^2 + \partial_z^2$ is a differential operator that acts on the coordinates. The exponential in k_y can be expanded as

$$e^{ik_y(y-y')} = \sum_{n=0}^{\infty} \frac{i^n k_y^n (y-y')^n}{n!} = 1 + \sum_{n=1}^{\infty} \frac{i^n k_y^n (y-y')^n}{n!}. \quad (6.A.4)$$

We split the contributions for $n = 0$ and $n > 0$ in the summation of Eq. (6.A.4) to show explicitly how the contact interaction emerges.

Replacing Eq. (6.A.4) into Eq. (6.A.3) and focusing on the integral over k_y , we find

$$\int_{-\infty}^{\infty} dk_y \frac{1}{(k_x^2 + k_y^2 + \omega^2)^{3/2}} \left(1 + \sum_{n=1}^{\infty} \frac{i^n k_y^n (y-y')^n}{n!} \right) = \frac{2}{k_x^2 + \omega^2} + \sum_{n=1}^{\infty} \frac{i^n (y-y')^n}{n!} \frac{[1 + (-1)^n] \Gamma(1 - \frac{n}{2}) \Gamma(\frac{n+1}{2})}{\sqrt{\pi} (k_x^2 + \omega^2)^{1 - \frac{n}{2}}}, \quad (6.A.5)$$

where the sum is only valid for even values of n , and for $n = 2$ the Gamma function has a pole. We show later that this pole cancels when one integrates further.

By replacing Eq. (6.A.5) into Eq. (6.A.3), we find

$$\left[\frac{1}{(-\square)} \right]_* = -\frac{\square}{4\pi} \int \frac{d^2 k}{(2\pi)^2} e^{ik_x(x-x') + i\omega(t-t')} \times \left\{ \frac{2}{k_x^2 + \omega^2} + \sum_{n=1}^{\infty} \frac{i^n (y-y')^n}{n!} \frac{[1 + (-1)^n] \Gamma(1 - \frac{n}{2}) \Gamma(\frac{n+1}{2})}{\sqrt{\pi} (k_x^2 + \omega^2)^{1 - \frac{n}{2}}} \right\}, \quad (6.A.6)$$

and now we can apply the derivatives to the remaining functions. The first term of Eq. (6.A.6) generates the local interaction, i.e.

$$-\frac{\square}{2\pi} \int \frac{d\omega}{2\pi} \int \frac{dk_x}{2\pi} \frac{e^{ik_x(x-x') + i\omega(t-t')}}{k_x^2 + \omega^2} = \frac{1}{2\pi} \delta(x-x') \delta(t-t'), \quad (6.A.7)$$

which appears due to the first contribution of the expansion of Eq. (6.A.4). The result obtained in Eq. (6.A.7) does not depend on whether we consider or not the constraint on the y -component. However, this is not the case for the second term of Eq. (6.A.6), which gives

$$\begin{aligned} & -\frac{1}{2\pi} \sum_{n \text{ even}}^{\infty} \frac{i^n \Gamma(1 - \frac{n}{2}) \Gamma(\frac{n+1}{2})}{\sqrt{\pi} (n!)} \square \left[(y-y')^n \int \frac{d^2 k}{(2\pi)^2} \frac{e^{ik_x(x-x') + i\omega(t-t')}}{(k_x^2 + \omega^2)^{1 - \frac{n}{2}}} \right] \\ = & -\frac{1}{2\pi} \sum_{n \text{ even}}^{\infty} \frac{i^n \Gamma(1 - \frac{n}{2}) \Gamma(\frac{n+1}{2})}{\sqrt{\pi} (n!)} \left[n(n-1) (y-y')^{n-2} \int \frac{d^2 k}{(2\pi)^2} \frac{e^{ik_x(x-x') + i\omega(t-t')}}{(k_x^2 + \omega^2)^{1 - \frac{n}{2}}} \right] \\ & + \frac{1}{2\pi} \sum_{n \text{ even}}^{\infty} \frac{i^n (-n/2) \Gamma(-\frac{n}{2}) \Gamma(\frac{n+1}{2})}{\sqrt{\pi} (n!)} \left[(y-y')^n \int \frac{d^2 k}{(2\pi)^2} \frac{e^{ik_x(x-x') + i\omega(t-t')}}{(k_x^2 + \omega^2)^{-\frac{n}{2}}} \right]. \end{aligned} \quad (6.A.8)$$

Integrating over ω for both terms in Eq. (6.A.8), we find

$$\begin{aligned} & \frac{1}{(2\pi)^2} \int_{-\infty}^{\infty} dk_x e^{ik_x(x-x')} \int_{-\infty}^{\infty} d\omega \frac{e^{i\omega(t-t')}}{(k_x^2 + \omega^2)^{1-\frac{n}{2}}} = \frac{2^{(1+n)/2} \sqrt{\pi}}{(2\pi)^2 \Gamma(1 - \frac{n}{2})} \\ & \times \int_{-\infty}^{\infty} dk_x e^{ik_x(x-x')} |t-t'|^{(1-n)/2} (k_x^2)^{\frac{n-1}{4}} \mathcal{K}_{\frac{n-1}{2}} \left(|t-t'| \sqrt{k_x^2} \right), \end{aligned} \quad (6.A.9)$$

and

$$\begin{aligned} & \frac{1}{(2\pi)^2} \int_{-\infty}^{\infty} dk_x e^{ik_x(x-x')} \int_{-\infty}^{\infty} d\omega \frac{e^{i\omega(t-t')}}{(k_x^2 + \omega^2)^{-\frac{n}{2}}} = \frac{2^{(3+n)/2} \sqrt{\pi}}{(2\pi)^2 \Gamma(-\frac{n}{2})} \\ & \times \int_{-\infty}^{\infty} dk_x e^{ik_x(x-x')} |t-t'|^{-(1+n)/2} (k_x^2)^{\frac{n+3}{4}} \mathcal{K}_{\frac{n+1}{2}} \left(|t-t'| \sqrt{k_x^2} \right), \end{aligned} \quad (6.A.10)$$

where \mathcal{K}_ζ 's are modified Bessel functions of the second kind. Plugging the results of Eqs. (6.A.9) and (6.A.10) into Eq. (6.A.8), we see that the poles disappear. Moreover, by imposing the constraint on the y -component ($y = y' = 0$), we observe that all the n -even contributions vanish, except $n = 2$ for the first term of Eq. (6.A.8). For $n = 2$, Eq. (6.A.8) becomes

$$\frac{1}{2(2\pi)^2} \int_{-\infty}^{\infty} dk_x e^{ik_x(x-x')} \frac{e^{-|t-t'| \sqrt{k_x^2}}}{|t-t'|} = \frac{1}{4\pi^2} \frac{1}{|t-t'|^2 + |x-x'|^2}. \quad (6.A.11)$$

Hence, summing the results of Eqs. (6.A.7) and (6.A.11), we have

$$\left[\frac{1}{(-\square)} \right]_{**} = \frac{1}{2\pi} \delta(x-x') \delta(t-t') + \frac{1}{4\pi^2} \frac{1}{(t-t')^2 + (x-x')^2}, \quad (6.A.12)$$

where the symbol $**$ means that we took both the y - and the z -coordinate constraints into account. Interestingly, the Fourier transform of the second term in Eq. (6.A.12) is actually

$$\frac{1}{(t-t')^2 + (x-x')^2} = \int \frac{dk_x}{2\pi} \int \frac{d\omega}{2\pi} \frac{e^{ik_x(x-x') + i\omega(t-t')}}{\omega^2 + k_x^2} \equiv \frac{1}{\square_{1+1}}, \quad (6.A.13)$$

which then yields an effective interaction composed of a sum of a local and a non-local term, i.e.

$$\left[\frac{1}{(-\square)} \right]_{**} = \frac{1}{2\pi} \delta(x-x') \delta(t-t') + \frac{1}{4\pi^2} \frac{1}{\square_{1+1}}. \quad (6.A.14)$$

6.B Effective action and (1+1)D Lagrangian

From the result found in Eq. (6.A.14), the effective action reads

$$\begin{aligned}
S_{\text{int}} &= -\frac{e^2}{2\varepsilon_0 c} \int d^4 r d^4 r' j_{3+1}^\mu(r) \frac{1}{(-\square)} j_\mu^{3+1}(r') \\
&= -\frac{e^2}{2\varepsilon_0 c} \int d^2 r d^2 r' j_{1+1}^\mu(r) \left[\frac{1}{(-\square)} \right]_{**} j_\mu^{1+1}(r') \\
&= \underbrace{-\frac{e^2}{4\pi\varepsilon_0 c} \int d^2 r j_{1+1}^\mu(r) j_{1+1}^\mu(r)}_{S_{\text{int}}^1} \quad \underbrace{-\frac{e^2}{8\pi^2\varepsilon_0 c} \int d^2 r d^2 r' j_{1+1}^\mu(r) \frac{1}{\square_{1+1}} j_\mu^{1+1}(r')}_{S_{\text{int}}^2}.
\end{aligned} \tag{6.B.1}$$

Now, the effective theory has the following partition function

$$\mathcal{Z} = \int \mathcal{D}\bar{\psi} \int \mathcal{D}\psi \exp \left[\frac{i}{\hbar} (S_{\text{free}} + S_{\text{int}}^1 + S_{\text{int}}^2) \right], \tag{6.B.2}$$

where we split the effective action in Eq. (6.B.1) in two parts, i.e., $S_{\text{int}} = S_{\text{int}}^1 + S_{\text{int}}^2$, and S_{free} contains the *free* Dirac Lagrangian in (1+1)D. Because both interaction terms S_{int}^a (with $a = 1, 2$) are quadratic in the fields, by using a Hubbard-Stratonovich transformation

$$\exp \left\{ \frac{i}{\hbar} S_{\text{int}}^a[\bar{\psi}, \psi] \right\} = \int \mathcal{D}\mathcal{A}_\mu^a \exp \left\{ \frac{i}{\hbar} \tilde{S}_{\text{int}}^a[\bar{\psi}, \psi, \mathcal{A}_\mu^a] \right\}, \tag{6.B.3}$$

we introduce auxiliary gauge-fields \mathcal{A}_μ^a and unveil the underlying gauge theory that mediates the four-fermion (local and non-local) interaction. Thus, the partition function becomes

$$\mathcal{Z} = \int \mathcal{D}\mathcal{A}_\mu^1 \int \mathcal{D}\mathcal{A}_\mu^2 \int \mathcal{D}\bar{\psi} \int \mathcal{D}\psi \exp \left\{ \frac{i}{\hbar} \int d^2 \mathbf{r} \mathcal{L}_{1+1}[\bar{\psi}, \psi, \mathcal{A}_\mu^1, \mathcal{A}_\mu^2] \right\}, \tag{6.B.4}$$

where

$$\mathcal{L}_{1+1} = i\hbar\bar{\psi}\gamma^\mu\partial_\mu\psi - e j^\mu \mathcal{A}_\mu^1 - \bar{e} j^\mu \mathcal{A}_\mu^2 - \varrho_1 F_{\mu\nu}^1 \frac{1}{\square_{1+1}} F_1^{\mu\nu} - \varrho_2 F_{\mu\nu}^2 F_2^{\mu\nu}, \tag{6.B.5}$$

with $\varrho_1 = \pi\varepsilon_0 c/2$ and $\varrho_2 = \pi^2\varepsilon_0 c$ dimensionless constants. By integrating out the \mathcal{A}_μ^1 -field we obtain the Thirring model [128], whereas the Lagrangian for \mathcal{A}_μ^2 gives us the Schwinger model [126]. Both models are exactly solvable in (1+1)D. Notice that \bar{e} is a dimensionful bare constant, which is in agreement with the Schwinger model. Because the action is dimensionless, all the terms inside the parenthesis in Eq. (6.2.9) must have dimension of $(\text{mass})^2 = (\text{length})^{-2}$. Thus, the product

$c_1 A_\mu^1$ and $c_2 A_\mu^2$ (with c_1 and c_2 coupling constants) share the same dimensionality, i.e. $(\text{length})^{-1}$. However, the fields A_μ^1 and A_μ^2 have different kinematical terms, yielding a different dimensionality to each of them. While A_μ^1 has dimension $(\text{length})^{-1}$, leading to a dimensionless coupling $c_1 = e$; A_μ^2 is dimensionless and its coupling with the fermionic current has dimension $(\text{length})^{-1}$, i.e. $c_2 = e\Lambda \equiv \bar{e}$.

The correspondence between Eqs. (6.B.1) and (6.B.5) can be seen explicitly by squaring the gauge fields \mathcal{A}_μ^1 and \mathcal{A}_μ^2 . In this manner, we obtain the following effective interactions between the matter currents

$$\begin{aligned} \varrho_1 \left(-F_{\mu\nu}^1 \frac{1}{\square_{1+1}} F_1^{\mu\nu} - \frac{e j^\mu \mathcal{A}_\mu^1}{\varrho_1} \right) &= 2\varrho_1 \left(\mathcal{A}_\mu^1 \mathcal{A}_1^\mu - \frac{e j^\mu \mathcal{A}_\mu^1}{2\varrho_1} \right) \\ &= 2\varrho_1 \left(\mathcal{A}_\mu^1 \mathcal{A}_1^\mu - \frac{2e j^\mu \mathcal{A}_\mu^1}{4\varrho_1} + \frac{e^2 j^\mu j_\mu}{16\varrho_1^2} \right) - \frac{e^2 j^\mu j_\mu}{8\varrho_1}, \end{aligned}$$

and

$$\begin{aligned} \varrho_2 \left(-F_{\mu\nu}^2 F_2^{\mu\nu} - \frac{\bar{e} j^\mu \mathcal{A}_\mu^2}{\varrho_2} \right) &= 2\varrho_2 \left(\mathcal{A}_\mu^2 \partial^\nu \partial_\nu \mathcal{A}_2^\mu - \frac{\bar{e} j^\mu \mathcal{A}_\mu^2}{2\varrho_2} \right) \\ &= 2\varrho_2 \left(\mathcal{A}_\mu^2 \partial^2 \mathcal{A}_2^\mu - \frac{2\bar{e} j^\mu \mathcal{A}_\mu^2}{4\varrho_2} + \frac{\bar{e}^2 j^\mu \partial^{-2} j_\mu}{16\varrho_2^2} \right) - \frac{\bar{e}^2}{8\varrho_2} j^\mu \frac{1}{\square_{1+1}} j_\mu, \end{aligned}$$

which reproduce the two terms in Eq. (6.B.1) for $\varrho_1 = \pi\varepsilon_0 c/2$ and $\varrho_2 = \pi^2\varepsilon_0 c$.

6.C Details on the bosonization procedure

From Eq. (6.3.1), we may write down the effective (massless) fermionic Lagrangian density in (1+1)D

$$\mathcal{L}_{1+1}^{\text{eff}}(\bar{\psi}, \psi) = i\hbar\bar{\psi}\gamma^\mu\partial_\mu\psi - \frac{e^2}{8\pi\varepsilon_0 c}(\bar{\psi}\gamma^\mu\psi)^2, \quad (6.C.1)$$

which leads to the following Hamiltonian density

$$\mathcal{H}_{\text{eff}} = i\hbar\bar{\psi}\gamma^0\dot{\psi} - \mathcal{L}_{1+1}^{\text{eff}} = -i\hbar v_F \bar{\psi}\gamma^1\partial_1\psi + \frac{e^2 v_F}{8\pi\varepsilon_0 c}(\bar{\psi}\gamma^\mu\psi)^2. \quad (6.C.2)$$

Here, by choosing the chiral basis

$$\gamma^0 = \begin{pmatrix} 0 & 1 \\ 1 & 0 \end{pmatrix}, \quad \gamma^1 = \begin{pmatrix} 0 & 1 \\ -1 & 0 \end{pmatrix}$$

and $\psi^\dagger = (\psi_R^\dagger, \psi_L^\dagger)$, with their respective anti-commutation relations, we find

$$\bar{\psi}\gamma^1\partial_1\psi = \psi^\dagger\gamma^0\gamma^1\partial_1\psi = -\psi_R^\dagger\partial_x\psi_R + \psi_L^\dagger\partial_x\psi_L, \quad (6.C.3)$$

and

$$(\bar{\psi}\gamma^\mu\psi)(\bar{\psi}\gamma_\mu\psi) = (\bar{\psi}\gamma^0\psi)(\bar{\psi}\gamma_0\psi) + (\bar{\psi}\gamma^1\psi)(\bar{\psi}\gamma_1\psi) = 4\psi_R^\dagger\psi_R\psi_L^\dagger\psi_L. \quad (6.C.4)$$

Hence, the effective 1D Hamiltonian reads

$$H_{\text{eff}} = \int dx \mathcal{H}_{\text{eff}} = v_F \int dx \left\{ i\hbar \left(\psi_R^\dagger \partial_x \psi_R - \psi_L^\dagger \partial_x \psi_L \right) + \frac{e^2}{2\pi\epsilon_0 c} \psi_R^\dagger \psi_R \psi_L^\dagger \psi_L \right\}. \quad (6.C.5)$$

By defining the bosonization rules in Eq. (6.3.4), with $\{\psi_{L,R}(x), \psi_{L,R}(x')\} = 0$, we derive the expressions for the currents by using the point splitting method. In the case of right movers, we find

$$\begin{aligned} J_R(x) &= \lim_{\varepsilon \rightarrow 0} \left[\psi_R^\dagger(x + \varepsilon) \psi_R(x) - \left\langle \psi_R^\dagger(x + \varepsilon) \psi_R(x) \right\rangle \right] \\ &= \frac{1}{2\pi} \lim_{\varepsilon \rightarrow 0} \left[e^{i\sqrt{4\pi}\phi_R(x+\varepsilon)} e^{-i\sqrt{4\pi}\phi_R(x)} - \left\langle e^{i\sqrt{4\pi}\phi_R(x+\varepsilon)} e^{-i\sqrt{4\pi}\phi_R(x)} \right\rangle \right] \\ &= \frac{1}{2\pi} \lim_{\varepsilon \rightarrow 0} \left[e^{i\varepsilon\sqrt{4\pi}\frac{1}{\varepsilon}[\phi_R(x+\varepsilon)-\phi_R(x)]} \frac{1}{\varepsilon} - \frac{1}{\varepsilon} \right] \\ &= \frac{1}{2\pi} \lim_{\varepsilon \rightarrow 0} \left[e^{i\varepsilon\sqrt{4\pi}\partial_x\phi_R(x)} \frac{1}{\varepsilon} - \frac{1}{\varepsilon} \right] \\ &= \frac{1}{2\pi} \lim_{\varepsilon \rightarrow 0} \left\{ \left[1 + i\varepsilon\sqrt{4\pi}\partial_x\phi_R(x) + \mathcal{O}(\varepsilon^2) \right] \frac{1}{\varepsilon} - \frac{1}{\varepsilon} \right\} \\ &= \frac{i}{\sqrt{\pi}} \partial_x \phi_R(x), \end{aligned} \quad (6.C.6)$$

where we have used

$$e^{i\alpha\phi(x)} e^{i\beta\phi(x')} = e^{i\alpha\phi(x)+i\beta\phi(x')} (x-x')^{\alpha\beta/4\pi}, \quad (6.C.7)$$

and

$$\left\langle \psi_R^\dagger(x) \psi_R(x') \right\rangle = \frac{1}{2\pi} \frac{1}{x-x'}. \quad (6.C.8)$$

By performing a similar procedure, we obtain the current for the left movers

$$J_L(x) = -\frac{i}{\sqrt{\pi}} \partial_x \phi_L(x). \quad (6.C.9)$$

Now, we look at the kinetic term in the Hamiltonian density (6.C.5),

$$\psi_R^\dagger(x) \partial_x \psi_R(x) = -i \lim_{\varepsilon \rightarrow 0} \left\{ \psi_R^\dagger(x + \varepsilon) \partial_x \psi_R(x) - \left\langle \psi_R^\dagger(x + \varepsilon) \partial_x \psi_R(x) \right\rangle \right\}, \quad (6.C.10)$$

and by using that

$$\partial_x \psi_R(x) = \lim_{\varepsilon' \rightarrow 0} \frac{\psi_R(x + \varepsilon') - \psi_R(x)}{\varepsilon'},$$

we obtain

$$\begin{aligned} & \psi_R^\dagger(x) \partial_x \psi_R(x) \\ &= -i \lim_{\varepsilon, \varepsilon' \rightarrow 0} \frac{1}{\varepsilon'} \left\{ \psi_R^\dagger(x + \varepsilon) [\psi_R(x + \varepsilon') - \psi_R(x)] - \left\langle \psi_R^\dagger(x + \varepsilon) [\psi_R(x + \varepsilon') - \psi_R(x)] \right\rangle \right\} \\ &= -i \lim_{\varepsilon, \varepsilon' \rightarrow 0} \frac{1}{\varepsilon'} \left\{ \psi_R^\dagger(x') \psi_R(x + \varepsilon') - \psi_R^\dagger(x') \psi_R(x) - \frac{1}{2\pi(x' - x - \varepsilon')} + \frac{1}{2\pi(x' - x)} \right\} \\ &= -i \lim_{\varepsilon, \varepsilon' \rightarrow 0} \frac{1}{\varepsilon'} \left\{ \psi_R^\dagger(x') \psi_R(x + \varepsilon') - \psi_R^\dagger(x') \psi_R(x) - \frac{1}{2\pi(\varepsilon - \varepsilon')} + \frac{1}{2\pi\varepsilon} \right\}, \end{aligned}$$

with $x' = x + \varepsilon$. By using Eqs. (6.C.7) and (6.C.8), we find

$$\begin{aligned} \psi_R^\dagger(x') \psi_R(x + \varepsilon') &= \frac{1}{2\pi} e^{i\sqrt{4\pi}\phi_R(x')} e^{-i\sqrt{4\pi}\phi_R(x + \varepsilon')} = \frac{1}{2\pi} \frac{e^{i\sqrt{4\pi}[\phi_R(x') - \phi_R(x + \varepsilon')]} }{x' - x - \varepsilon'} \\ &= \frac{1}{2\pi} \frac{1}{\varepsilon - \varepsilon'} e^{-i\sqrt{4\pi}\frac{\varepsilon'}{\varepsilon}[\phi_R(x + \varepsilon') - \phi_R(x')]}, \end{aligned}$$

and

$$\begin{aligned} \psi_R^\dagger(x') \psi_R(x) &= \frac{1}{2\pi} e^{i\sqrt{4\pi}\phi_R(x + \varepsilon)} e^{-i\sqrt{4\pi}\phi_R(x)} = \frac{1}{2\pi\varepsilon} e^{i\sqrt{4\pi}\frac{\varepsilon}{\varepsilon}[\phi_R(x + \varepsilon) - \phi_R(x)]} \\ &= \frac{1}{\varepsilon} e^{i\sqrt{4\pi\varepsilon}\partial_x\phi_R(x)} = \frac{1}{2\pi\varepsilon} \left\{ 1 + i\sqrt{4\pi\varepsilon}\partial_x\phi_R(x) + \mathcal{O}(\varepsilon^2) \right\}. \end{aligned}$$

Then, by replacing the results above into Eq. (6.C.10), we obtain

$$\begin{aligned} \psi_R^\dagger(x) \partial_x \psi_R(x) &= -i \lim_{\varepsilon, \varepsilon' \rightarrow 0} \frac{1}{\varepsilon'} \left\{ \psi_R^\dagger(x') \psi_R(x + \varepsilon') - \frac{1}{2\pi\varepsilon} \left[1 + i\sqrt{4\pi\varepsilon}\partial_x\phi_R(x) + \dots \right] \right. \\ &\quad \left. - \frac{1}{2\pi(\varepsilon - \varepsilon')} + \frac{1}{2\pi\varepsilon} \right\} \\ &= -i \lim_{\varepsilon' \rightarrow 0} \frac{1}{\varepsilon'} \left\{ -\frac{1}{2\pi\varepsilon'} e^{-i\sqrt{4\pi}\frac{\varepsilon'}{\varepsilon}[\phi_R(x + \varepsilon') - \phi_R(x)]} - \frac{i}{\sqrt{\pi}} \partial_x \phi_R(x) + \frac{1}{2\pi\varepsilon'} \right\} \\ &= -i \lim_{\varepsilon' \rightarrow 0} \frac{1}{\varepsilon'} \left\{ -\frac{1}{2\pi\varepsilon'} e^{-i\sqrt{4\pi\varepsilon'}\partial_x\phi_R(x)} - \frac{i}{\sqrt{\pi}} \partial_x \phi_R(x) + \frac{1}{2\pi\varepsilon'} \right\} \\ &= i \lim_{\varepsilon' \rightarrow 0} \frac{1}{\varepsilon'} \left\{ \frac{1}{2\pi\varepsilon'} \left[-i\sqrt{4\pi\varepsilon'}\partial_x\phi_R(x) - 2\pi\varepsilon'^2[\partial_x\phi_R(x)]^2 + \mathcal{O}(\varepsilon^3) \right] + \frac{i}{\sqrt{\pi}} \partial_x \phi_R(x) \right\} \\ &= i \lim_{\varepsilon' \rightarrow 0} \frac{1}{\varepsilon'} \left\{ -\frac{i}{\sqrt{\pi}} \partial_x \phi_R(x) - \varepsilon'[\partial_x\phi_R(x)]^2 + \frac{i}{\sqrt{\pi}} \partial_x \phi_R(x) \right\} \\ &= -i [\partial_x \phi_R(x)]^2 = i\pi J_R^2. \end{aligned}$$

where we used the following expansion

$$e^{-i\sqrt{4\pi}\varepsilon'\partial_x\phi_R(x)} = 1 - i\sqrt{4\pi}\varepsilon'\partial_x\phi_R(x) - \frac{4\pi\varepsilon'^2}{2!}[\partial_x\phi_R(x)]^2 + \mathcal{O}(\varepsilon'^3).$$

Analogously, we find

$$\psi_L^\dagger(x)\partial_x\psi_L(x) = -i\pi J_L^2,$$

and the non-interacting Hamiltonian (H_0) reads

$$H_0 = i\hbar v_F \int dx \left(\psi_R^\dagger \partial_x \psi_R - \psi_L^\dagger \partial_x \psi_L \right) = -v_F \hbar \pi \int dx \left(J_R^2 + J_L^2 \right). \quad (6.C.11)$$

For the interacting term, we have

$$H_{\text{int}} = \frac{e^2 v_F}{2\pi \varepsilon_0 c} \int dx J_{R,\uparrow} J_{L,\downarrow}, \quad (6.C.12)$$

where we wrote explicitly the spin dependence of right (and left) movers because in the case of the helical liquid the spin and momentum are locked, respecting time-reversal symmetry.

Now, we perform a change of variables in a way similar to spin-charge separation, i.e.

$$\varphi = \frac{1}{\sqrt{2}} (\phi_R + \phi_L) \quad \text{and} \quad \theta = \frac{1}{\sqrt{2}} (\phi_R - \phi_L), \quad (6.C.13)$$

thus

$$\phi_R = \frac{1}{\sqrt{2}} (\varphi + \theta) \quad \text{and} \quad \phi_L = \frac{1}{\sqrt{2}} (\varphi - \theta). \quad (6.C.14)$$

By replacing the results for $J_{R,L}(x)$ into Eqs. (6.C.11) and (6.C.12), we obtain

$$\begin{aligned} H_0^{\text{bos}} &= v_F \hbar \int dx \left[(\partial_x \phi_R)^2 + (\partial_x \phi_L)^2 \right] \\ &= \frac{v_F \hbar}{2} \int dx \left\{ [\partial_x (\varphi + \theta)]^2 + [\partial_x (\varphi - \theta)]^2 \right\} \\ &= v_F \hbar \int dx \left[(\partial_x \varphi)^2 + (\partial_x \theta)^2 \right], \end{aligned} \quad (6.C.15)$$

and

$$\begin{aligned}
 H_{\text{int}}^{\text{bos}} &= \frac{e^2 v_F}{2\pi\epsilon_0 c} \int dx \frac{1}{\pi} (\partial_x \phi_R) (\partial_x \phi_L) \\
 &= \frac{e^2 v_F}{4\pi^2 \epsilon_0 c} \int dx [\partial_x (\varphi + \theta)] [\partial_x (\varphi - \theta)] \\
 &= \frac{e^2 v_F}{4\pi^2 \epsilon_0 c} \int dx [(\partial_x \varphi)^2 - (\partial_x \theta)^2]. \tag{6.C.16}
 \end{aligned}$$

Therefore, by summing Eqs. (6.C.15) and (6.C.16), we find the full bosonic Hamiltonian

$$\begin{aligned}
 H_{\text{eff}}^{\text{bos}} &= H_0^{\text{bos}} + H_{\text{int}}^{\text{bos}} \\
 &= v_F \hbar \int dx \left[\left(1 + \frac{e^2}{4\pi^2 \hbar \epsilon_0 c}\right) (\partial_x \varphi)^2 + \left(1 - \frac{e^2}{4\pi^2 \hbar \epsilon_0 c}\right) (\partial_x \theta)^2 \right] \\
 &= v_F \hbar \left[\left(1 + \frac{e^2}{4\pi^2 \hbar \epsilon_0 c}\right) \left(1 - \frac{e^2}{4\pi^2 \hbar \epsilon_0 c}\right) \right]^{1/2} \times \\
 &\quad \int dx \left[\frac{\left(1 + \frac{e^2}{4\pi^2 \hbar \epsilon_0 c}\right)^{1/2}}{\left(1 - \frac{e^2}{4\pi^2 \hbar \epsilon_0 c}\right)^{1/2}} (\partial_x \varphi)^2 + \frac{\left(1 - \frac{e^2}{4\pi^2 \hbar \epsilon_0 c}\right)^{1/2}}{\left(1 + \frac{e^2}{4\pi^2 \hbar \epsilon_0 c}\right)^{1/2}} (\partial_x \theta)^2 \right] \\
 &= \tilde{v}_F \int dx \left[\frac{1}{K} (\partial_x \varphi)^2 + K (\partial_x \theta)^2 \right], \tag{6.C.17}
 \end{aligned}$$

where the Luttinger parameter K_L and the renormalized velocity \tilde{v}_F are respectively given by Eqs. (6.3.5) and (6.3.6).

6.D Masses in the Thirring model and the backscattering interaction

To investigate the properties of the edge states in presence of an external Zeeman field, which breaks time-reversal symmetry, one may add a mass (i.e. $m\bar{\psi}\psi$) to the Dirac fermions in Eq. (6.2.1). The parameter m is proportional to the intensity of the Zeeman field, which we consider for simplicity constant in modulus and direction. Because this mass term is not affected by the dimensional-reduction procedure, it also appears in the Thirring model, generating a gap in the boundary modes. In the Hamiltonian picture, this massive term is written as

$$H_m = m \int dx \left(\psi_R^\dagger \psi_L + \psi_L^\dagger \psi_R \right). \tag{6.D.1}$$

Now, by using the bosonization rules with the Klein factors properly defined [141], the above massive term becomes

$$H_m^{\text{bos}} = \frac{m}{\pi} \int dx \cos(\sqrt{8\pi}\varphi). \quad (6.D.2)$$

For the bosonic representation, this cosine term, when localized in a small region, acts as a boundary in the system, changing the fermionic orientation of propagation. The existence of such contribution leads to the study of the renormalization group of the Sine-Gordon model, as already analyzed in Ref. [136]. Note that the above term looks similar to the one obtained in Ref. [122], induced by the Umklapp scattering.

At a theoretical level, another possible massive term is $i\Delta\bar{\psi}\gamma^5\psi$ with $\gamma^5 = \gamma^0\gamma^1$. The coefficient Δ is known as the chiral mass and it adds to the fermionic Hamiltonian the following contribution

$$H_\Delta = i\Delta \int dx (\psi_R^\dagger\psi_L - \psi_L^\dagger\psi_R), \quad (6.D.3)$$

which mainly differs from the usual Dirac mass by a factor minus between $\psi_R^\dagger\psi_L$ and its conjugated. The minus sign in Eq. (6.D.3) leads to a bosonized Hamiltonian containing an interaction term that depends on a sine function instead of a cosine, i.e.,

$$H_\Delta^{\text{bos}} = -\frac{\Delta}{\pi} \int dx \sin(\sqrt{8\pi}\varphi). \quad (6.D.4)$$

Here, we can easily recover the standard potential in Eq. (6.D.2) after a constant shift of the scalar field, i.e. $\varphi \rightarrow \varphi - \pi/2$.

ATYPICAL HALL CONDUCTIVITY IN THE VARMA PHASE

In this chapter, we analyze the topological response of a fermionic model defined on the Lieb lattice in presence of an electromagnetic field. The tight-binding model is built in terms of three species of spinless fermions and supports a topological Varma phase due to the spontaneous breaking of time-reversal symmetry. In the low-energy regime, the emergent effective Hamiltonian coincides with the so-called Duffin-Kemmer-Petiau (DKP) Hamiltonian, which describes relativistic pseudospin-0 quasiparticles. By considering a minimal coupling between the DKP quasiparticles and an external Abelian gauge field, we first find the Landau-level spectrum by fixing the Landau gauge; then we compute the emergent Chern-Simons theory for a weak-electromagnetic-field regime. The corresponding Hall conductivity reveals an atypical QHE, which can be simulated in an artificial Lieb lattice.

Note: This chapter is based in Ref. [147], where I contributed by performing the calculations in Sec. 7.4.

7.1 Introduction

In 1928, Dirac proposed a theory for the description of relativistic spin-1/2 particles. Since then, his model has found several theoretical applications, which have extrapolated the boundaries between high- and low-energy physics. Nowadays, the Dirac theory plays a fundamental role in condensed-matter physics on the description of materials such as graphene [2], TIs [81], and topological superconductors [148], due to their relativistic-like bulk/edge band dispersion. These so-called Dirac materials have unique properties, like the bulk-edge correspondence [149],

which allow for innovative applications in future quantum technologies [150, 151]. Differently from the fundamental fermions in the original model [152], the effective low-energy theory in these materials describes either Dirac or Weyl quasiparticles that emerge in their bulk and/or edge. For instance, in 3D, massless Dirac and Weyl quasiparticles appear in the bulk of Dirac [153] and Weyl semimetals [154], respectively. Moreover, there exists a deep connection between the Dirac theory and topology via the Clifford bundles, K-theory and the index theorem [30], which has allowed to classify, in a mathematical way, TIs, topological superconductors and topological semimetals in any dimension [29, 31–33].

Dirac materials, however, represent only a particular class of quantum systems with relativistic band dispersion. Several models described by *quasi-relativistic* non-Dirac Hamiltonians have been recently proposed both in condensed-matter and cold-atom systems [155–168]. In these works, quasiparticles carrying pseudo-spin-1 [169] emerge in the bulk of the material and are associated to the presence of flat bands on the Lieb lattice. This lattice has been recently implemented in artificial electronic [38, 39] and photonic [40–42] systems, opening the way to experimentally investigating novel quantum phenomena related to the presence of quasiparticles with integer pseudospin.

Furthermore, unlike the previously mentioned works, a novel topological system on the Lieb lattice supporting *relativistic* pseudospin-0 quasiparticles has been theoretically proposed in Ref. [170]. These quasiparticles are described by a 2D DKP theory [171], which represents an extension of the Dirac theory for integer-spin particles. This model gives rise to a Chern-semimetallic phase, where the chiral edge modes are topologically protected by a non-zero Chern number in the bulk.

From a more concrete perspective, the Lieb lattice is relevant in the study of high-Tc cuprates, where the Varma phase [172, 173] was shown to be important in the description of the pseudogap regime. Within this picture, the copper (Cu) sites are characterized by $d_{x^2-y^2}$ orbitals and the planar oxygen (O) by p_x (p_y) orbitals. Due to interaction, orbital current loops emerge, spontaneously breaking time-reversal symmetry, but preserving the translational symmetry of the lattice (see Fig. 7.1).

The aim of this chapter is to study the topological response of the Varma phase introduced in Ref. [37] to an applied electromagnetic field. We first show that the low-energy theory coincides with the 2D DKP theory by unveiling the pseudospin-0 character of quasiparticles emerging in the Varma phase. In this regime, we calculate the Landau levels in the presence of a constant magnetic field and emphasize the main differences with the Landau levels that appear in quasi-relativistic systems on the Lieb lattice [160, 161]. We then determine the emergent

Chern-Simons theory [174] in the bulk induced by a weak external electromagnetic field, and derive the Hall conductivity. Surprisingly, an atypical QHE is found for the DKP quasiparticles, which emerges from the relativistic nature of the low-energy theory.

To our knowledge, our work provides the first derivation of a Chern-Simons theory from a microscopic model that is described by a relativistic non-Dirac Hamiltonian. This opens the way to a full quantum-field-theory characterization of topological phases on the Lieb lattice. We propose an implementation of this model in an artificial electronic system, where Landau level spectroscopy can be employed to reveal the effective electric charge of DKP quasiparticles.

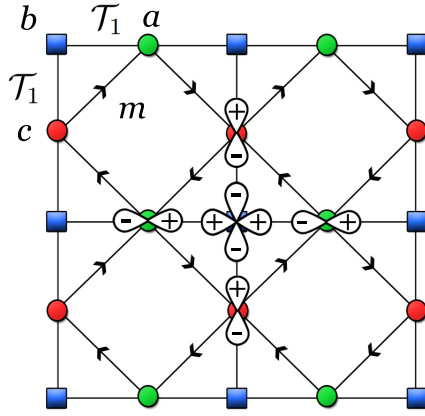


Figure 7.1: Lieb lattice with three species of spinless fermions labeled by a , b and c , which are associated to p_x , $d_{x^2-y^2}$ and p_y orbitals, respectively. The tunneling \mathcal{T}_1 is induced by the overlap between $d_{x^2-y^2}$ and p_x (p_y) orbitals in x (y)-direction. The diagonal lines correspond to the next-nearest-neighbor (NNN) loop currents between p_x and p_y orbitals, which arise from a mean-field description, with m the amplitude of the complex hopping.

7.2 DKP theory on the Lieb lattice

We start by considering a tight-binding model on the Lieb lattice with three different species of fermions, as proposed in Ref. [37]. The fermions are represented by the operators a , b and c in Fig. 7.1, where a and c represent p orbitals, while b is a d orbital. The momentum-space Hamiltonian of the model is divided in a free and an interacting part, i.e. $H = H_0 + H_{\text{int}}$, with

$$H_0 = 2i\mathcal{T}_1 b_{\mathbf{k}}^\dagger (s_x a_{\mathbf{k}} + s_y c_{\mathbf{k}}) - \mathcal{T}_2 s_x s_y a_{\mathbf{k}}^\dagger c_{\mathbf{k}} + \text{H.c.} \quad (7.2.1)$$

Here, \mathcal{T}_1 and \mathcal{T}_2 are real hopping parameters, $s_x = \sin(k_x/2)$, $s_y = \sin(k_y/2)$ and

$$H_{\text{int}} = \mathcal{V} \sum n_a n_c + \text{H.c.}, \quad (7.2.2)$$

which represents the interaction between p orbitals in the a and c sites, with n_i denoting the number operator and \mathcal{V} the interaction strength. By employing a mean-field approximation for the interaction term in Eq. (7.2.2) in the particle-hole channel [37], a new complex hopping term is induced between NNN,

$$H_{\text{int}}^{\text{MF}} = im \cos(k_x/2) \cos(k_y/2) a_{\mathbf{k}}^\dagger c_{\mathbf{k}} + \text{H.c.}, \quad (7.2.3)$$

where $M(k_x, k_y) = im \cos(k_x/2) \cos(k_y/2) = \mathcal{V} \langle c^\dagger a \rangle$ is the order parameter that behaves like a mass term. For $m = 0$, the system exhibits a single Dirac-like cone at the Γ -point in the first Brillouin zone and a zero-energy flat band. For $m \neq 0$, the time-reversal symmetry is broken and the system displays an anomalous quantum Hall phase characterized by a non-zero Chern number for the lower band [37].

For \mathcal{T}_2 smaller than \mathcal{T}_1 , in the low-energy limit, the corresponding effective Hamiltonian H_{DKP} is fully relativistic and reads (see Sec. 7.A for a detailed derivation)

$$H_{\text{DKP}} = \mathcal{T}_1 [\beta^1, \beta^0] k_x + \mathcal{T}_1 [\beta^2, \beta^0] k_y + m\beta^0, \quad (7.2.4)$$

where the 3×3 matrices β^μ with $\mu = 0, 1, 2$ are given by

$$\beta^0 = \begin{pmatrix} 0 & 0 & 0 \\ 0 & 0 & i \\ 0 & -i & 0 \end{pmatrix}, \quad \beta^1 = \begin{pmatrix} 0 & 0 & -1 \\ 0 & 0 & 0 \\ 1 & 0 & 0 \end{pmatrix}, \quad \beta^2 = \begin{pmatrix} 0 & 1 & 0 \\ -1 & 0 & 0 \\ 0 & 0 & 0 \end{pmatrix}.$$

These matrices satisfy the relation

$$\beta^\mu \beta^\nu \beta^\sigma + \beta^\sigma \beta^\nu \beta^\mu = \beta^\mu g^{\nu\sigma} + \beta^\sigma g^{\nu\mu}, \quad (7.2.5)$$

where $g^{\mu\nu}$ is the Minkowski metric. The above conditions identify the DKP algebra [171], which is the core of the DKP theory and describes relativistic pseudospin-0 quasiparticles in 2D.

By implementing a Legendre transformation on Eq. (7.2.4), the DKP action may be written in terms of a first-order Lagrangian [171], i.e.

$$S_{\text{DKP}}[\bar{\chi}, \chi] = \int d^3x \bar{\chi} (i\hbar\beta^\mu \partial_\mu - m)\chi, \quad (7.2.6)$$

where $d^3x = dt d^2x$, $\chi = (\chi_b, \chi_a, \chi_c)^T$, the adjoint spinor $\bar{\chi} = \chi \xi^0$, with $\xi^0 =$

$2(\beta^0)^2 - \mathbf{1}_{3 \times 3}$, and \mathcal{T}_1 has been fixed to unit for simplicity. Similarly to other relativistic field theories, the spinor field χ satisfies the Klein-Gordon equation at semiclassical level, i.e. $(\square + m^2)\chi = 0$.

7.3 Landau levels in the DKP theory

Now, we proceed by investigating the effect of an external perpendicular magnetic field on the Lieb lattice. As for the Dirac theory, we introduce an electromagnetic field in the DKP theory by minimally coupling the gauge field A_μ and vector DKP current $j^\mu = \bar{\chi}\beta^\mu\chi$, i.e. $\partial_\mu \rightarrow D_\mu = \partial_\mu - i(q/\hbar)A_\mu$, where q is the electric charge. We choose the Landau gauge, and determine the Landau levels in our (2+1)D system (details in Sec. 7.B), in analogy to Ref. [175], where the (3+1)D case is treated. We then find

$$E(\mathcal{B}) = \pm\sqrt{m^2 + (2\mathcal{N} + 1)\hbar q\mathcal{B}}, \quad (7.3.1)$$

with $\mathcal{N} = 0, 1, 2, \dots$. For $m = 0$, the Landau levels coincide with those ones derived in Ref. [160], when the (non-dispersing) flat band appears at zero energy. However, for $m \neq 0$, the Landau levels found here for a fully relativistic theory are different from those of the gapped phase on the Lieb lattice calculated in Ref. [160] for a quasi-relativistic theory.

Importantly, Eq. (7.3.1) is equivalent to the Landau levels of a 2D *scalar* field coupled to an external magnetic field [176]. This unveils the bosonic nature of the DKP field.

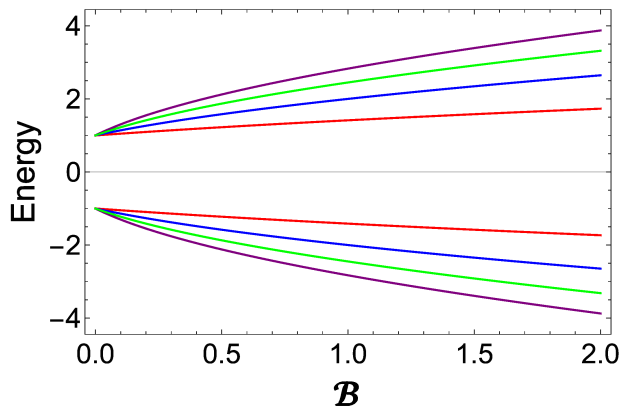


Figure 7.2: Plot of Landau levels with respect to the magnetic field \mathcal{B} for $\mathcal{N} = 0, 1, 2, 3$ at fixed mass m and charge q .

7.4 Chern-Simons theory and Hall conductivity

So far, in the Landau gauge, we have shown that the Landau level spectrum of the DKP quasiparticles is different from the Dirac case. Now, we investigate, in the weak-field approximation [149], the topological response of the system to an external electromagnetic field $A_\mu = A_\mu(\mathbf{x}, t)$, which contains both the scalar and the vector potentials. In this way, the gauge field acts like a flux in the Haldane model [36] and yields an anomalous Hall response. Hence, the action (7.2.6) becomes

$$S_{\text{DKP}}[\bar{\chi}, \chi, A_\mu] = \int d^3x \bar{\chi} (i\hbar\beta^\mu \partial_\mu + q\beta^\mu A_\mu - m)\chi. \quad (7.4.1)$$

The topological behavior is encoded in the effective topological field theory (ETFT) $S_{\text{eff}}^{\text{T}}[A_\mu]$ that can be derived from the above action by integrating out the spinor fields in the corresponding partition function. We have that

$$e^{\frac{i}{\hbar} S_{\text{eff}}[A_\mu]} = \int \mathcal{D}\bar{\chi} \mathcal{D}\chi e^{\frac{i}{\hbar} S_{\text{DKP}}[\bar{\chi}, \chi, A_\mu]}, \quad (7.4.2)$$

where the effective action $S_{\text{eff}}[A_\mu]$ splits into a sum of a topological (T) and a non-topological (NT) contribution,

$$\begin{aligned} S_{\text{eff}}[A_\mu] &= -i\hbar \log \det(i\hbar\beta^\mu \partial_\mu + q\beta^\mu A_\mu - m) \\ &= S_{\text{eff}}^{\text{T}} + S_{\text{eff}}^{\text{NT}}. \end{aligned} \quad (7.4.3)$$

Like in the 2D massive Dirac theory [174, 177–179], the ETFT in our case is determined by the calculation of the photon one-loop self-energy diagram and is given by an Abelian Chern-Simons theory

$$S_{\text{eff}}^{\text{T}}[A_\mu] = \frac{1}{2} \int \frac{d^3p}{(2\pi)^3} A_\mu(-p) \Pi^{\mu\nu}(p) A_\nu(p), \quad (7.4.4)$$

where the polarization tensor $\Pi^{\mu\nu}$ is obtained via

$$i\Pi^{\mu\nu} = -\frac{q^2}{\hbar} \int \frac{d^3k}{(2\pi)^3} \text{Tr} [\beta^\mu G_\chi(k) \beta^\nu G_\chi(k-p)], \quad (7.4.5)$$

and G_χ is the DKP quasiparticle propagator,

$$G_\chi(k) = i \frac{\beta^\gamma k_\gamma + m}{k^2 - m^2}. \quad (7.4.6)$$

Next, we substitute the expression for the propagator above into Eq. (7.4.5), and perform the calculations focusing on the antisymmetric (AS) part of the tensor

$\Pi^{\mu\nu}$, which leads to the Chern-Simons term (see Sec. 7.C for details)

$$i\Pi_{\text{AS}}^{\mu\nu} = \frac{q^2}{8\pi\hbar} \epsilon^{\mu\nu\alpha} p_\alpha \text{sgn}(m). \quad (7.4.7)$$

Notice that the Levi-Civita tensor $\epsilon^{\mu\nu\alpha}$ arises due to the trace properties of DKP matrices β^μ , i.e. $\text{Tr}[\beta^\mu\beta^\nu\beta^\alpha] = i\epsilon^{\mu\nu\alpha}$. With the result (7.4.7), by using Kubo's formula, we obtain the Hall conductivity (for $i, j = 1, 2$)

$$\sigma^{ij} = \lim_{p_0 \rightarrow 0} \frac{i\Pi_{\text{AS}}^{ij}}{p_0} = \text{sgn}(m) \frac{q^2}{4h}. \quad (7.4.8)$$

As it stands, Eq. (7.4.8) predicts a *quarter-integer* QHE for charge $q = e$ fermions. This result is astonishing because we started from the single-particle Hamiltonian (7.2.4), and as such, one should expect to obtain an integer QHE, even because the Chern number for this model is integer [37, 170]. We explain below the reasons behind this unexpected finding.

The knowledge and understanding of the QHE in Dirac materials relies on the behavior of Dirac quasiparticles, which are described by the relativistic spin-1/2 Dirac theory. Within this category, we can distinguish three main examples in 2D: the Haldane model [36], the Bernevig-Hughes-Zhang (BHZ) model [24], and the gapped boundary of 3D TIs [25].

In the first case, there appear two massive Dirac cones in the bulk due to the Nielsen-Ninomiya theorem (namely, the fermion doubling problem, see Ref. [180]). Each massive Dirac fermion in the bulk with a constant Dirac mass contributes 1/2 to the total Chern number, such that the bulk Chern number is always an integer. Indeed, the Haldane model supports an QAHE.

In the BHZ model, there appears a single Dirac cone in the bulk, and in the gapped phase, the Dirac mass is not constant but momentum-dependent. This is a sort of regularization, where one can avoid the Nielsen-Ninomiya theorem for the Dirac fermion, which induces directly an integer value for the topological invariant in the bulk of the system.

In the case of 3D TIs, each gapped surface state supports a 2D massive Dirac fermion leading to a half-integer Chern number, and a half-integer QHE [25]. Here, the Nielsen-Ninomiya theorem is avoided because the 2D system lives on the boundary of a higher-dimensional bulk. The Chern number per surface is 1/2 and the Hall conductivity is given in units of $e^2/2h$ even if there is no topological ground state degeneracy on the gapped boundary. Moreover, the corresponding effective field theory is given by an Abelian Chern-Simons theory with half-integer level.

The result of Eq. (7.4.8) challenges this understanding in two ways: First, the

Chern number in the lower band of the DKP model is ± 1 as shown in Refs. [37, 170]. This implies that the non-integer value of the Hall conductivity in Eq. (7.4.8) cannot come from a non-integer value of the Chern number, like in the case of a single massive Dirac fermion mentioned above. On the other hand, the Nielsen-Ninomiya theorem is avoided in our model because of the presence of a flat band [181]. In other words, there is a single valley and at the same time the DKP mass is also constant in the low-energy limit. Second, the trace of the three β matrices is half of the value of the trace of three Pauli matrices. This trace is related to the anti-symmetric part of the polarization tensor that gives rise to the Chern-Simons action. These are the two formal reasons behind the fractional coefficient in Eq. (7.4.8).

This original result could nevertheless be reconciled with the integer-valued Hall conductivity if the charge $q = 2e$. This picture is consistent with the bosonic nature of our low-energy DKP quasiparticles, which behave effectively like bosons, as revealed by analyzing the properties of their wavefunctions [182]. Hidden charge $2e$ bosons have been already proposed to appear in the pseudogap regime of high- T_c cuprates, where they emerge from a low-energy theory of a *doped* Mott insulator [183, 184]. However, there is no interaction in our Hamiltonian (7.2.4) that could lead to pairing within a conventional picture of superconductivity.

7.5 Edge modes

The existence of topologically protected chiral edge modes on the Lieb lattice has been shown in Ref. [170] by employing the entanglement spectrum. Here, we provide an analytic derivation of the Dirac edge modes from the DKP Hamiltonian by following a domain-wall argument. In particular, we employ the Jackiw-Rebbi approach [185], as already done in Dirac systems.

The boundary of the system corresponds to a nodal interface at $x = 0$, where the mass $m(x)$ runs from negative to positive (or vice-versa). Let us consider the DKP Hamiltonian in Eq. (7.2.4) with a spatially varying mass term, and for simplicity we set $\mathcal{T}_1 = 1$ and $\hbar = 1$. Importantly, we assume that $m(x)_{x \rightarrow \pm\infty} = \pm m_0$. Notice that due to the periodicity in the y -direction, k_y is still a good quantum number. Therefore, we can replace $\partial_y \rightarrow ik_y$ in the Hamiltonian, such that the eigenvalue problem $H_{\text{DKP}}\mathcal{X} = E\mathcal{X}$ can be solved by solutions $\mathcal{X}(x, y) = (\mathcal{C}_u(x), \mathcal{C}_v(x), \mathcal{C}_w(x))^\top e^{ik_y y}$ with energy $E(k_y) = k_y$. We then obtain the following

first-order differential equations

$$\begin{aligned}
-k_y \mathcal{C}_u + \partial_x \mathcal{C}_v + ik_y \mathcal{C}_w &= 0, \\
-\partial_x \mathcal{C}_u - k_y \mathcal{C}_v + im \mathcal{C}_w &= 0, \\
-ik_y \mathcal{C}_u - im \mathcal{C}_v - k_y \mathcal{C}_w &= 0.
\end{aligned} \tag{7.5.1}$$

The last equality leads to $\mathcal{C}_u = i(k_y \mathcal{C}_w + im \mathcal{C}_v)/k_y$, which may be substituted into the first equation to yield a first-order differential equation for $\mathcal{C}_v(x)$

$$\partial_x \mathcal{C}_v(x) = -m(x) \mathcal{C}_v(x). \tag{7.5.2}$$

The solution of Eq. (7.5.2) reads $\mathcal{C}_v(x) = \tilde{c}_0 e^{-\int dx m(x)}$, with \tilde{c}_0 a suitable real constant. In the simplest case, in which the domain wall is described by a Heaviside step function, i.e. $m(x) = m_0[2\theta(x) - 1]$, we obtain

$$\mathcal{C}_v(x) = \tilde{c}_0 e^{-m_0[2\theta(x)-1]x} = \tilde{c}_0 e^{-m_0|x|}, \tag{7.5.3}$$

which represents a localized edge state at $x = 0$ when $m(x)$ goes from positive to negative, i.e. m_0 is positive and Eq. (7.5.3) is a normalizable wave function. From Eqs. (7.5.1), we also obtain

$$\partial_x \mathcal{C}_u(x) - m(x) \mathcal{C}_u(x) = \left(\frac{m_0^2 - k_y^2}{k_y} \right) \mathcal{C}_v(x), \tag{7.5.4}$$

where the equality holds because $\theta(x)^2 = \theta(x)$. Thus, the solution of Eq. (7.5.4) is given by

$$\mathcal{C}_u(x) = \left(\frac{m_0^2 - k_y^2}{k_y} \right) e^{\int dx m(x)} \int dx e^{-2\int dx m(x)}, \tag{7.5.5}$$

which does not describe any localized edge mode at $x = 0$. It can be easily shown that $\mathcal{C}_u(x)_{x \rightarrow 0} = 0$ and $\mathcal{C}_u(x)_{x \rightarrow \pm\infty} = \pm\infty$. At the same time, $\mathcal{C}_w(x)$ does not describe any edge mode either. However, when $m(x)$ goes from negative to positive, m_0 is negative and Eq. (7.5.3) does not correspond to any physical solution because it yields a non-renormalizable solution. In this case, c_1 is zero, such that $\mathcal{C}_v(x) = 0$. By plugging this solution into Eqs. (7.5.1), we get different solutions for $\mathcal{C}_u(x)$ and $\mathcal{C}_w(x)$. In this case, we find that $\mathcal{C}_u(x) = \bar{c}_0 e^{\int dx m(x)}$ (with \bar{c}_0 a suitable real constant), which identifies a localized edge mode because $m_0 < 0$. On the other hand, we get also $\mathcal{C}_w(x) = -i\mathcal{C}_u(x)$, which does not correspond to any localized mode in the real plane.

Thus, in both cases, i.e. $m_0 > 0$ and $m_0 < 0$, we can show that there is always a single propagating edge mode along the domain wall at $x = 0$. This single Dirac

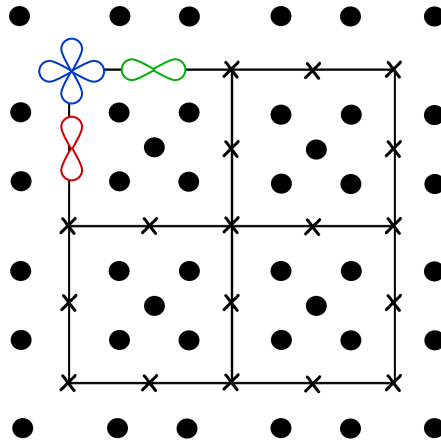


Figure 7.3: Patterning of an electronic Lieb lattice using CO adsorbates.

edge mode propagating on the boundary of the system may be represented by a scalar field in (1+1)D. Therefore, in this system, the DKP theory exists only in (2+1)D, and is absent at the edge.

7.6 Experimental realization

Here, we propose an electronic quantum simulation of the Cu-O model analyzed in this chapter. By following Ref. [38], we consider an electronic Lieb lattice built by confining the electrons on the surface state of Cu(111) by an array of CO molecules positioned with a scanning tunneling microscope (STM), as shown in Fig. 7.3. The CO molecules are represented by black circles, which act as a repulsive potential and confine the electrons to the Lieb-lattice geometry. To simulate, respectively, the d and p -orbitals at the corner and side sites, we propose to use an anisotropic configuration, in which the four COs are further away from the corner, and closer to the side sites, as depicted in Fig. 7.3. This leads to weaker confinement at the corner, and hence to higher orbital wave functions.

By investigating the behavior of the system at low temperatures, under ultra-clean conditions, we expect to reach the interacting regime, where the mean-field Varma phase with loop currents in each plaquette should emerge. Similar systems have been emulated with ultra cold bosons in optical lattices [186, 187]. Finally, an external magnetic field will be added perpendicularly to the Lieb lattice, to induce Landau levels and the quantum Hall state in the system.

In this electronic quantum simulator, the value of the quasiparticle charge may be determined by spectroscopic measurements of the Landau levels. This

procedure may provide a direct observation of the charge q in the Varma phase, and resolve the puzzling result obtained for the Hall conductivity.

7.7 Conclusions

Here, we investigate the electromagnetic response of pseudospin-0 DKP quasiparticles on the Lieb lattice. First, we derive the Landau levels induced by a constant magnetic field orthogonal to the system. Then, we analyze the topological response of the model in presence of a U(1) gauge potential in terms of an Abelian Chern-Simons theory, from which we obtained an atypical Hall conductivity. The experimental realization of this setup will reveal the real effective value of the electric charge of DKP quasiparticles. In any case, the relativistic description of non-Dirac systems holds promises to reveal a much richer physics than in conventional Dirac materials.

7.A Low-energy Hamiltonian

Here, we detail how to obtain Eq. (7.2.4). Starting from the Hamiltonian $H = H_0 + H_{\text{int}}^{\text{MF}}$, after the mean-field treatment of the interaction,

$$H = 2i\mathcal{T}_1 \left[b_{\mathbf{k}}^\dagger (s_x a_{\mathbf{k}} + s_y c_{\mathbf{k}}) - (s_x a_{\mathbf{k}}^\dagger + s_y c_{\mathbf{k}}^\dagger) b_{\mathbf{k}} \right] + M(k_x, k_y) (a_{\mathbf{k}}^\dagger c_{\mathbf{k}} - c_{\mathbf{k}}^\dagger a_{\mathbf{k}}), \quad (7.A.1)$$

where we used that $\mathcal{T}_1 \gg \mathcal{T}_2$. For small momenta, we may expand the functions

$$s_x = \sin\left(\frac{k_x}{2}\right) \approx \frac{k_x}{2}, \quad s_y = \sin\left(\frac{k_y}{2}\right) \approx \frac{k_y}{2},$$

$$M(k_x, k_y) = im(1 + \mathcal{O}(k_x^2))(1 + \mathcal{O}(k_y^2)) \approx im,$$

and obtain

$$\begin{aligned} H &= i\mathcal{T}_1 \left[k_x (b_{\mathbf{k}}^\dagger a_{\mathbf{k}} - a_{\mathbf{k}}^\dagger b_{\mathbf{k}}) + k_y (b_{\mathbf{k}}^\dagger c_{\mathbf{k}} - c_{\mathbf{k}}^\dagger b_{\mathbf{k}}) \right] + im (a_{\mathbf{k}}^\dagger c_{\mathbf{k}} - c_{\mathbf{k}}^\dagger a_{\mathbf{k}}) \\ &= (b_{\mathbf{k}}^\dagger \ a_{\mathbf{k}}^\dagger \ c_{\mathbf{k}}^\dagger) \begin{pmatrix} 0 & i\mathcal{T}_1 k_x & i\mathcal{T}_1 k_y \\ -i\mathcal{T}_1 k_x & 0 & im \\ -i\mathcal{T}_1 k_y & -im & 0 \end{pmatrix} \begin{pmatrix} b_{\mathbf{k}} \\ a_{\mathbf{k}} \\ c_{\mathbf{k}} \end{pmatrix} = \chi^\dagger H_{\mathbf{k}} \chi. \end{aligned} \quad (7.A.2)$$

By rewriting $H_{\mathbf{k}}$, we find

$$\begin{aligned} H_{\mathbf{k}} &= \mathcal{T}_1 k_x \begin{pmatrix} 0 & i & 0 \\ -i & 0 & 0 \\ 0 & 0 & 0 \end{pmatrix} + \mathcal{T}_1 k_y \begin{pmatrix} 0 & 0 & i \\ 0 & 0 & 0 \\ -i & 0 & 0 \end{pmatrix} + m \begin{pmatrix} 0 & 0 & 0 \\ 0 & 0 & i \\ 0 & -i & 0 \end{pmatrix} \\ &= \mathcal{T}_1 k_x i \beta^2 - \mathcal{T}_1 k_y i \beta^1 + m \beta^0, \end{aligned} \quad (7.A.3)$$

which by using $[\beta^n, \beta^m] = i\epsilon\beta^{nmj}\beta^j$ leads to Eq. (7.2.4).

7.B DKP Landau-level solution

By starting from Eq. (7.2.4) with $\mathcal{T}_1 = \hbar = 1$, and minimally coupling to an external magnetic field perpendicular to the plane via $\mathbf{k} - q\mathbf{A}$, where $\mathbf{A} = (0, \mathcal{B}x)$, we find

$$\begin{pmatrix} 0 & ik_x & i(k_y - e\mathcal{B}x) \\ -ik_x & 0 & im \\ -i(k_y - e\mathcal{B}x) & -im & 0 \end{pmatrix} \begin{pmatrix} \chi_b \\ \chi_a \\ \chi_c \end{pmatrix} = E \begin{pmatrix} \chi_b \\ \chi_a \\ \chi_c \end{pmatrix}, \quad (7.B.1)$$

where $E > 0$ are the energy eigenvalues, and $\chi_i(\mathbf{r}) = \chi_i(x, y)$. From Eq. (7.B.1), we obtain the coupled equations

$$ik_x \chi_a + i(k_y - e\mathcal{B}x) \chi_c = E \chi_b, \quad (7.B.2)$$

$$-ik_x \chi_b + im \chi_c = E \chi_a, \quad (7.B.3)$$

$$-i(k_y - e\mathcal{B}x) \chi_b - im \chi_a = E \chi_c. \quad (7.B.4)$$

Now, our aim is to find equations for χ_a, χ_b and χ_c , separately. First, we may isolate χ_b in Eqs. (7.B.2) and (7.B.4),

$$\chi_b = \frac{ik_x \chi_a + i(k_y - e\mathcal{B}x) \chi_c}{E}, \quad (7.B.5)$$

and

$$\chi_b = \frac{im \chi_a + E \chi_c}{-i(k_y - e\mathcal{B}x)}. \quad (7.B.6)$$

Then, we compare Eqs. (7.B.5) and (7.B.6),

$$\begin{aligned} \frac{ik_x \chi_a + i(k_y - e\mathcal{B}x) \chi_c}{E} &= \frac{im \chi_a + E \chi_c}{-i(k_y - e\mathcal{B}x)} \\ \therefore \chi_c &= \frac{(k_y - e\mathcal{B}x) k_x - iEm}{[E^2 - (k_y - e\mathcal{B}x)^2]} \chi_a, \end{aligned} \quad (7.B.7)$$

to obtain a relation between two of the solutions, χ_c and χ_a . By plugging Eq. (7.B.7) into (7.B.6), we find a second relation, between χ_b and χ_a ,

$$\begin{aligned}\chi_b &= \frac{im}{-i(k_y - e\mathcal{B}x)}\chi_a + \frac{E}{-i(k_y - e\mathcal{B}x)} \frac{(k_y - e\mathcal{B}x)k_x - iEm}{[E^2 - (k_y - e\mathcal{B}x)^2]}\chi_a \\ &= \frac{m(k_y - e\mathcal{B}x) + iEk_x}{[E^2 - (k_y - e\mathcal{B}x)^2]}\chi_a\end{aligned}\quad (7.B.8)$$

We substitute the results (7.B.7) and (7.B.8) into Eq. (7.B.3),

$$\begin{aligned}-ik_x \frac{m(k_y - e\mathcal{B}x) + iEk_x}{[E^2 - (k_y - e\mathcal{B}x)^2]}\chi_a + im \frac{(k_y - e\mathcal{B}x)k_x - iEm}{[E^2 - (k_y - e\mathcal{B}x)^2]}\chi_a &= E\chi_a \\ \left[E^2 - k_x^2 - (k_y - e\mathcal{B}x)^2 - m^2 - \frac{me\mathcal{B}}{E} \right] \chi_a &= 0,\end{aligned}\quad (7.B.9)$$

to get the equation for the χ_a solution.

Analogously, we may obtain the solutions for both χ_b and χ_c . Now, we isolate χ_a in Eqs. (7.B.3) and (7.B.4), and obtain

$$\chi_a = \frac{-ik_x\chi_b + im\chi_c}{E},\quad (7.B.10)$$

and

$$\chi_a = \frac{-i(k_y - e\mathcal{B}x)\chi_b - E\chi_c}{im}.\quad (7.B.11)$$

By comparing Eqs. (7.B.10) and (7.B.11), we find

$$\begin{aligned}\frac{-ik_x\chi_b + im\chi_c}{E} &= \frac{-i(k_y - e\mathcal{B}x)\chi_b - E\chi_c}{im} \\ \therefore \chi_c &= -\frac{[iE(k_y - e\mathcal{B}x) + mk_x]}{(E^2 - m^2)}\chi_b.\end{aligned}\quad (7.B.12)$$

We replace Eq. (7.B.12) into (7.B.10),

$$\begin{aligned}\chi_a &= \frac{-ik_x}{E}\chi_b - \frac{im}{E} \frac{[iE(k_y - e\mathcal{B}x) + mk_x]}{E^2 - m^2}\chi_b \\ &= \frac{[-ik_xE + m(k_y - e\mathcal{B}x)]}{(E^2 - m^2)}\chi_b.\end{aligned}\quad (7.B.13)$$

Then, we substitute the results (7.B.12) and (7.B.13) into Eq. (7.B.2)

$$\begin{aligned}ik_x \frac{[-ik_xE + m(k_y - e\mathcal{B}x)]}{(E^2 - m^2)}\chi_b - i(k_y - e\mathcal{B}x) \frac{[iE(k_y - e\mathcal{B}x) + mk_x]}{(E^2 - m^2)}\chi_b &= E\chi_b \\ \left[E^2 - k_x^2 - (k_y - e\mathcal{B}x)^2 - m^2 + \frac{me\mathcal{B}}{E} \right] \chi_b &= 0.\end{aligned}\quad (7.B.14)$$

The last equation we need to find is the one for χ_c . From Eq. (7.B.3), we isolate χ_b to obtain the relation

$$\chi_b = \frac{E\chi_a - im\chi_c}{-ik_x}. \quad (7.B.15)$$

We compare (7.B.15) and (7.B.5),

$$\frac{E\chi_a - im\chi_c}{-ik_x} = \frac{ik_x\chi_a + i(k_y - e\mathcal{B}x)\chi_c}{E} \quad (7.B.16)$$

$$\therefore \chi_a = \frac{[iEm + k_x(k_y - e\mathcal{B}x)]}{(E^2 - k_x^2)}\chi_c. \quad (7.B.17)$$

By plugging Eq. (7.B.17) into (7.B.15), we find

$$\begin{aligned} \chi_b &= \frac{iE[iEm + (k_y - e\mathcal{B}x)k_x]}{k_x(E^2 - k_x^2)}\chi_c + \frac{m}{k_x}\chi_c \\ &= \frac{iE(k_y - e\mathcal{B}x) - mk_x}{(E^2 - k_x^2)}\chi_c. \end{aligned} \quad (7.B.18)$$

Then, we replace Eqs. (7.B.17) and (7.B.18) into (7.B.4), to obtain

$$\begin{aligned} &\frac{-i(k_y - e\mathcal{B}x)[iE(k_y - e\mathcal{B}x) - mk_x]}{(E^2 - k_x^2)}\chi_c - \frac{im[iEm + k_x(k_y - e\mathcal{B}x)]}{(E^2 - k_x^2)}\chi_c = E\chi_c \\ &\left[E^2 - k_x^2 - (k_y - e\mathcal{B}x)^2 - m^2 - \frac{me\mathcal{B}}{E} \right] \chi_c = 0. \end{aligned} \quad (7.B.19)$$

Therefore, by considering $\chi(x, y) = \tilde{\chi}(x)e^{ik_y y}$, we may summarize the results of Eqs. (7.B.9), (7.B.14) and (7.B.19) as

$$\left[\left(\partial_{\tilde{x}}^2 - \tilde{x}^2 + \frac{E^2 - m^2}{|e\mathcal{B}|} \right) \mathbb{1}_{3 \times 3} - \frac{me\mathcal{B}}{E|e\mathcal{B}|} \xi^0 \right] \tilde{\chi} = 0, \quad (7.B.20)$$

where we redefine the x -variable as $\tilde{x} = \sqrt{e\mathcal{B}}[(k_y/e\mathcal{B}) - x]$, and $\xi^0 = 2(\beta^0)^2 - \mathbb{1}_{3 \times 3}$. The \tilde{x} -independent term reads

$$\frac{E^2 - m^2}{|e\mathcal{B}|} \mathbb{1}_{3 \times 3} - \frac{me\mathcal{B}}{E|e\mathcal{B}|} \xi^0 = a \rightarrow E[E^2 - (m^2 + a|e\mathcal{B}|)] \mathbb{1}_{3 \times 3} = me\mathcal{B}\xi^0, \quad (7.B.21)$$

where $a = 2\mathcal{N} + 1$ indicates the quantization. The presence of a nonzero term on the right-hand side of Eq. (7.B.21) is an inherent consequence of the three-band model, which sets a clear difference between the DKP and Dirac theories in the presence of an external magnetic field. The physical meaning of such extra term has been a topic of debate [175, 188, 189]. Mathematically, it is an inevitable

contribution that actually reveals the three-energy solution character, i.e. yields a third-degree polynomial. At this point, we may set $m = 0$ and find the following eigenvalues for Eq. (7.B.21)

$$E = 0, \quad E = \pm\sqrt{a|e\mathcal{B}|}. \quad (7.B.22)$$

For $m \neq 0$, we may focus on the behavior of the dispersive bands,

$$E^2 - (m^2 + a|e\mathcal{B}|) = 0 \rightarrow E = \pm\sqrt{m^2 + a|e\mathcal{B}|}. \quad (7.B.23)$$

where we considered the region $E \gg m$. Differently from the Dirac theory (see Sec. 2.3), the Landau-level spectrum here is not spin degenerated, thus indicating a theory of spin-0 (pseudospin-0) (quasi)particles.

7.C Polarization tensor details

We replace the propagator (7.4.6) into Eq. (7.4.5), and obtain

$$i\Pi^{\mu\nu} = q^2 \int \frac{d^3k}{(2\pi)^3} \frac{\text{Tr} [\beta^\mu (\beta^\alpha k_\alpha + m) \beta^\nu (\beta^\sigma (k-p)_\sigma + m)]}{(k^2 - m^2)[(k-p)^2 - m^2]}. \quad (7.C.1)$$

Now, we focus on the product of three β -matrices only,

$$\begin{aligned} i\Pi_{\text{AS}}^{\mu\nu} &= q^2 \int \frac{d^3k}{(2\pi)^3} \frac{\text{Tr} [\beta^\mu \beta^\alpha \beta^\nu k_\alpha m + \beta^\mu \beta^\nu \beta^\alpha (k-p)_\alpha m]}{(k^2 - m^2)[(k-p)^2 - m^2]} \\ &= -q^2 \int \frac{d^3k}{(2\pi)^3} \frac{i\epsilon^{\mu\nu\alpha} p_\alpha m}{(k^2 - m^2)[(k-p)^2 - m^2]}, \end{aligned} \quad (7.C.2)$$

where AS identifies the antisymmetric part of the polarization tensor. The linear terms in k do not contribute due to the symmetric integration. The denominator of Eq. (7.C.2) may be rewritten as

$$\frac{1}{(k^2 - m^2)[(k-p)^2 - m^2]} = \int_0^1 dx \frac{1}{(k^2 - \Delta)^2},$$

where $\Delta = m^2 - p^2x(1-x)$, and we perform the integrations in the regime $m \gg p$, to obtain

$$\begin{aligned}
i\Pi_{\text{AS}}^{\mu\nu} &= -iq^2\epsilon^{\mu\nu\alpha}p_\alpha m \int_0^1 dx \int \frac{d^3k}{(2\pi)^3} \frac{1}{(k^2 - \Delta)^2} \\
&= q^2 \frac{\epsilon^{\mu\nu\alpha}p_\alpha m}{8\pi} \int_0^1 \frac{dx}{\sqrt{m^2 - p^2x(1-x)}} \\
&= \frac{q^2}{8\pi} \epsilon^{\mu\nu\alpha} p_\alpha \text{sgn}(m).
\end{aligned} \tag{7.C.3}$$

Trace properties

It is straightforward to show that $\text{Tr}[\beta^\alpha] = 0$ and $\text{Tr}[\beta^\mu\beta^\sigma] = 2g^{\mu\sigma}$. In the case of three β -matrices, we find

$$\begin{aligned}
\text{Tr}[\beta^\alpha\beta^\mu\beta^\nu] &= \text{Tr}\left[\frac{1}{2}\beta^\alpha\beta^\mu\beta^\nu + \frac{1}{2}\beta^\alpha\beta^\mu\beta^\nu \pm \frac{1}{2}\beta^\mu\beta^\nu\beta^\alpha\right] \\
&= \text{Tr}\left[\frac{1}{2}(\beta^\alpha\beta^\mu\beta^\nu + \beta^\mu\beta^\nu\beta^\alpha) + \frac{1}{2}(\beta^\alpha\beta^\mu\beta^\nu - \beta^\mu\beta^\nu\beta^\alpha)\right] \\
&= \text{Tr}\left[\frac{1}{2}\{\beta^\alpha, \beta^\mu\beta^\nu\} + \frac{1}{2}[\beta^\alpha, \beta^\mu\beta^\nu]\right] \\
&= \frac{1}{2}\text{Tr}[\{\beta^\alpha, \beta^\mu\}\beta^\nu - \beta^\mu[\beta^\alpha, \beta^\nu] + [\beta^\alpha, \beta^\mu]\beta^\nu + \beta^\mu[\beta^\alpha, \beta^\nu]] \\
&= \frac{i}{2}\epsilon^{\alpha\mu\lambda}\text{Tr}[\beta_\lambda\beta^\nu] = i\epsilon^{\alpha\mu\nu},
\end{aligned} \tag{7.C.4}$$

where $\text{Tr}[\{\beta^\alpha, \beta^\mu\}\beta^\nu] = 0$ for $\alpha \neq \mu \neq \nu$.

BIBLIOGRAPHY

- [1] K. S. Novoselov, A. K. Geim, S. V. Morozov, D. Jiang, Y. Zhang, S. V. Dubonos, I. V. Grigorieva and A. A. Firsov, *Science* **306**, 666 (2004).
- [2] K. S. Novoselov, A. K. Geim, S. V. Morozov, D. Jiang, M. I. Katsnelson, I. V. Grigorieva, S. V. Dubonos and A. A. Firsov, *Nature* **438**, 197 (2005).
- [3] <https://www.flickr.com/photos/armymaterielcommand/6795812766>
- [4] C. R. Dean, A. F. Young, P. Cadden-Zimansky, L. Wang, H. Ren, K. Watanabe, T. Taniguchi, P. Kim, J. Hone and K. L. Shepard, *Nat. Phys.* **7**, 693 (2011).
- [5] X. Du, I. Skachko, F. Duerr, A. Luican and E. Y. Andrei, *Nature* **462**, 192 (2009).
- [6] K. I. Bolotin, F. Ghahari, M. D. Shulman, H. L. Stormer and P. Kim, *Nature* **462**, 196 (2009).
- [7] D. C. Elias, R. V. Gorbachev, A. S. Mayorov, S. V. Morozov, A. A. Zhukov, P. Blake, L. A. Ponomarenko, I. V. Grigorieva, K. S. Novoselov, F. Guinea and A. K. Geim, *Nat. Phys.* **7**, 701 (2011).
- [8] A. Luican, G. Li and E. Y. Andrei, *Phys. Rev. B* **83**, 041405(R) (2011).
- [9] J. Chae, S. Jung, A. F. Young, C. R. Dean, L. Wang, Y. Gao, K. Watanabe, T. Taniguchi, J. Hone, K. L. Shepard, P. Kim, N. B. Zhitenev and J. A. Stroscio, *Phys. Rev. Lett.* **109**, 116802 (2012).
- [10] J. González, F. Guinea and M. A. H. Vozmediano, *Nucl. Phys. B* **424**, 595 (1994).

- [11] J. González, F. Guinea and M. A. H. Vozmediano, *Phys. Rev. B* **59**, 2474 (1999).
- [12] M. S. Foster and I. L. Aleiner, *Phys. Rev. B* **77**, 195413 (2008).
- [13] J. González, F. Guinea and M. A. H. Vozmediano, *Phys. Rev. Lett.* **77**, 3589 (1996).
- [14] F. Juan, A. G. Grushin and M. A. H. Vozmediano, *Phys. Rev. B* **82**, 125409 (2010).
- [15] M. A. H. Vozmediano and F. Guinea, *Phys. Scr.* **T146**, 014015 (2012).
- [16] E. V. Kurganova, H. J. van Elferen, A. McCollam, L. A. Ponomarenko, K. S. Novoselov, A. Veligura, B. J. van Wees, J. C. Maan and U. Zeitler, *Phys. Rev. B* **84**, 121407 (R) (2011).
- [17] J. Schwinger, *Phys. Rev.* **73**, 416 (1948).
- [18] R. S. Van Dyck Jr., P. B. Schwinberg and H. G. Dehmelt, *Phys. Rev. Lett.* **59**, 26 (1987).
- [19] D. Hanneke, S. Fogwell and G. Gabrielse, *Phys. Rev. Lett.* **100**, 120801 (2008).
- [20] T. Aoyama, M. Hayakawa, T. Kinoshita and M. Nio, *Phys. Rev. Lett.* **109**, 111807 (2012).
- [21] Y. J. Song, A. F. Otte, Y. Kuk, Y. Hu, D. B. Torrance, P. N. First, A. W. de Heer, H. Min, S. Adam, M. D. Stiles, A. H. MacDonald and J. A. Stroscio, *Nature* **467**, 185 (2010).
- [22] M. König, S. Wiedmann, C. Brune, A. Roth, H. Buhmann, L. W. Molenkamp, X.-L. Qi and S.-C. Zhang, *Science* **318**, 766 (2007).
- [23] C. L. Kane and E. J. Mele, *Phys. Rev. Lett.* **95**, 226801 (2005).
- [24] B. A. Bernevig, T. L. Hughes and S.-C. Zhang, *Science* **314**, 1757 (2006).
- [25] X.-L. Qi, T. L. Hughes and S.-C. Zhang, *Phys. Rev. B* **78**, 195424 (2008).
- [26] Y. L. Chen, J. G. Analytis, J.-H. Chu, Z. K. Liu, S.-K. Mo, X.-L. Qi, H. J. Zhang, D. H. Lu, X. Dai, Z. Fang, S.-C. Zhang, I. R. Fisher, Z. Hussain and Z.-X. Shen, *Science* **325**, 178 (2009).

-
- [27] Y. Zhang, K. He, C.-Z. Chang, C.-L. Song, L.-L. Wang, X. Chen, J.-F. Jia, Z. Fang, X. Dai, W.-Y. Shan, S.-Q. Shen, Q. Niu, X.-L. Qi, S.-C. Zhang, X.-C. Ma and Q.-K. Xue, *Nat. Phys.* **6**, 584 (2010).
- [28] C. L. Kane and E. J. Mele, *Phys. Rev. Lett.* **95**, 146802 (2005).
- [29] A. Altland and M. R. Zirnbauer, *Phys. Rev. B* **55**, 1142 (1997).
- [30] M. Nakahara, *Geometry, Topology and Physics*, CRC Press (2003).
- [31] A. P. Schnyder, S. Ryu, A. Furusaki and A. W. W. Ludwig, *Phys. Rev. B* **78**, 195125 (2008).
- [32] A. Kitaev, *AIP Conf. Proc.* **1134**, 22 (2009).
- [33] C.-K. Chiu, J. C. Y. Teo, A. P. Schnyder and S. Ryu, *Rev. Mod. Phys.* **88**, 035005 (2016).
- [34] K. von Klitzing, G. Dorda and M. Pepper, *Phys. Rev. Lett.* **45**, 494 (1980).
- [35] D. J. Thouless, M. Kohmoto, M. P. Nightingale and M. den Nijs, *Phys. Rev. Lett.* **49**, 405 (1982).
- [36] F. D. M. Haldane, *Phys. Rev. Lett.* **61**, 2015 (1988).
- [37] Y. He, J. Moore and C. M. Varma, *Phys. Rev. B* **85**, 155106 (2012).
- [38] M. R. Slot, T. S. Gardenier, P. H. Jacobse, G. C. P. van Miert, S. N. Kempkes, S. J. M. Zevenhuizen, C. Morais Smith, D. Vanmaekelbergh and I. Swart, *Nat. Phys.* **13**, 672 (2017).
- [39] R. Drost, T. Ojanen, A. Harju and P. Liljeroth, *Nat. Phys.* **13**, 668 (2017).
- [40] D. Guzman-Silva, C. Mejia-Cortes, M. A. Bandres, M. C. Rechtsman, S. Weimann, S. Nolte, M. Segev, A. Szameit and R. A. Vicencio, *New J. Phys.* **16**, 063061 (2014).
- [41] S. Mukherjee, A. Spracklen, D. Choudhury, N. Goldman, P. Ohberg, E. Andersson and R. R. Thomson, *Phys. Rev. Lett.* **114**, 245504 (2015).
- [42] F. Diebel, D. Leykam, S. Kroesen, C. Denz and A. S. Desyatnikov, *Phys. Rev. Lett.* **116**, 183902 (2016).
- [43] M. Goerbig, *Rev. Mod. Phys.* **83**, 1193 (2011).
- [44] L. L. Foldy and S. A. Wouthuysen, *Phys. Rev.* **78**, 29 (1950).

- [45] E. C. Marino, Nucl. Phys. B **408**, 551 (1993).
- [46] E. V. Gorbar, V. P. Gusynin and V. A. Miransky, Phys Rev D **64**, 105028 (2001).
- [47] E. V. Gorbar, V. P. Gusynin, V. A. Miransky and I. A. Shovkovy, Phys. Scr. **T146**, 014018 (2012).
- [48] R. L. P. G. Amaral and E. C. Marino, J. Phys. A **25**, 5183 (1992).
- [49] E. C. Marino, L. O. Nascimento, V. S. Alves and C. Morais Smith, Phys. Rev. D **90**, 105003 (2014).
- [50] N. Menezes, V. S. Alves and C. Morais Smith, Eur. Phys. J. B **89**, 271 (2016).
- [51] B. Lalmi, H. Oughaddou, H. Enriquez, A. Kara, S. Vizzini, B. Ealet and B. Aufray, Appl. Phys. Lett. **97**, 223109 (2010).
- [52] Y. Xu, B. Yan, H.-J. Zhang, J. Wang, G. Xu, P. Tang, W. Duan and S.-C. Zhang, Phys. Rev. Lett. **111**, 136804 (2013).
- [53] X.-S. Ye, Z.-G. Shao, H. Zhao, L. Yangab and C.-L. Wang, RSC Adv. **4**, 21216 (2014).
- [54] X. Duan, C. Wang, A. Pan, R. Yu and X. Duan, Chem. Soc. Rev. **44**, 8859 (2015).
- [55] G. L. Yu, R. Jalil, B. Belle, A. S. Mayorov, P. Blake, F. Schedin, S. V. Morozov, L. A. Ponomarenko, F. Chiappini, S. Wiedmann, Uli Zeitler, M. I. Katsnelson, A. K. Geim, K. S. Novoselov and D. C. Elias, Proc. Natl. Acad. Sci. USA **110**, 3282 (2013).
- [56] N. Menezes, V. S. Alves, E. C. Marino, L. Nascimento, L. O. Nascimento and C. Morais Smith, Phys. Rev. B **95**, 245138 (2017).
- [57] In our opinion, the most appropriated use of the term weak magnetic field is to denote the regime of Shubnikov-de Haas oscillations, and not the regime of intermediate magnetic field, when several Landau levels are occupied. The strong magnetic field regime denotes the case when the physics involves only the lowest-Landau level.
- [58] V. R. Khalilov, Theo. and Math. Phys. **125**, 132-151 (2000).
- [59] E. V. Gorbar, V. A. Miransky, I. A. Shovkovy and Xinyang Wang, Phys. Rev. D **88**, 025043 (2013).

-
- [60] E. V. Gorbar, V. A. Miransky, I. A. Shovkovy and Xinyang Wang, Phys. Rev. D **88**, 025025 (2013).
- [61] K. Funakubo and M. Sakamoto, Prog. Theor. Phys. **76**, 490 (1986).
- [62] H. Matsumoto, Y. Nakano and H. Umezawa, Phys. Rev. D **29**, 1116 (1984).
- [63] A. Kovner and B. Rosenstein, Phys. Rev. B **42**, 4748 (1990).
- [64] N. Dorey and N. E. Mavromatos, Nucl. Phys. B **386**, 614 (1992).
- [65] S. Teber, Phys. Rev. D **86**, 025005 (2012).
- [66] S. Teber, Phys. Rev. D **89**, 067702 (2014).
- [67] E. C. Marino, L. O. Nascimento, V. S. Alves and C. Morais Smith, Phys. Rev. X **5**, 011040 (2015).
- [68] M. Koshino and T. Ando, Phys. Rev. B **81**, 195431 (2010).
- [69] C. G. Bollini and J. J. Giambiagi, Phys. Lett. B **40**, 566 (1972).
- [70] G. 't Hooft and M. Veltman, Nucl. Phys. B **44**, 189 (1972).
- [71] M. E. Peskin and D. V. Schroeder, *An Introduction to Quantum Field Theory*, Addison-Wesley Publishing Company (1995).
- [72] J. D. Bjorken and S. D. Drell, *Relativistic Quantum Mechanics*, McGraw-Hill Book Company (1964).
- [73] T. Ando and Y. Uemura, J. Phys. Soc. Jpn. **37**, 1044 (1974).
- [74] R. J. Nicholas, R. J. Haug, K. v. Klitzing and G. Weimann, Phys. Rev. B **37**, 1294 (1988).
- [75] A. V. Volkov, A. A. Shylau and I. V. Zozoulenko, Phys. Rev. B **86**, 155440 (2012).
- [76] S. Das Sarma, E. H. Hwang and W.-K. Tse, Phys. Rev. B **75**, 121406(R) (2007).
- [77] It was shown in Ref. [7] that it is possible to describe the renormalization of the Fermi velocity in leading order, given that a more elaborated RPA expression is used for the dielectric constant ε_G because it depends on the doping concentration n . Although the changes in ε_G upon varying n from 10^9 to 10^{12} cm $^{-2}$ would be significant, in the regime of the experimental data [16] used in our manuscript the carrier concentration $n \approx 1 - 4 \times 10^{12}$ cm $^{-2}$ remains nearly constant.

- [78] K. Shizuya, Phys. Rev. B **81**, 075407 (2010).
- [79] D. A. Siegel, C.-H. Park, C. Hwang, J. Deslippe, A. V. Fedorov, S. G. Louie and A. Lanzara, Proc. Natl. Acad. Sci. USA **108**, 11365 (2011).
- [80] N. Menezes, C. Morais Smith and G. Palumbo, J. Phys.: Condens. Matter **29**, 335601 (2017).
- [81] M. Z. Hasan and C. L. Kane, Rev. Mod. Phys. **82**, 3045 (2010).
- [82] R. B. Laughlin, Phys. Rev. Lett. **50**, 1395 (1983).
- [83] J. K. Jain, Phys. Rev. Lett. **63**, 199 (1989).
- [84] A. Lopez and E. Fradkin, Phys. Rev. B **44**, 5246 (1991).
- [85] M. O. Goerbig, Eur. Phys. J. B **85**, 15 (2012).
- [86] G. Murthy and R. Shankar, Phys. Rev. B **86**, 195146 (2012).
- [87] N. Read and D. Green, Phys. Rev. B **61**, 10267 (2000).
- [88] J. P. Eisenstein and A. H. MacDonald, Nature **432**, 691 (2004).
- [89] H. Leal and D. V. Khveshchenko, Nucl. Phys. B **687**, 323 (2004).
- [90] C.-H. Zhang and Y. N. Joglekar, Phys. Rev. B **77**, 233405 (2008).
- [91] J. C. Budich, B. Trauzettel and P. Michetti, Phys. Rev. Lett. **112**, 146405 (2014).
- [92] R. Nandkishore and L. Levitov, Phys. Rev. Lett. **104**, 156803 (2010).
- [93] O. V. Gamayun, E. V. Gorbar and V. P. Gusynin, Phys. Rev. B **81**, 075429 (2010).
- [94] B. Seradjeh, H. Weber and M. Franz, Phys. Rev. Lett. **101**, 246404 (2008).
- [95] R. L. Doretto, A. O. Caldeira and C. Morais Smith, Phys. Rev. Lett. **97**, 186401 (2006).
- [96] E. Rossi, A. S. Nunez, and A. H. MacDonald, Phys. Rev. Lett. **95**, 266804 (2005).
- [97] B. Seradjeh, J. E. Moore, and M. Franz, Phys. Rev. Lett. **103**, 066402 (2009).
- [98] E. G. Moon and C. Xu, EPL **97**, 66008 (2012).

-
- [99] D. K. Efimkin, Y. E. Lozovik and A. A. Sokolik, *Phys. Rev. B* **86**, 115436 (2012).
- [100] K. Wu, L. Rademaker and J. Zaanen, *Phys. Rev. Appl.* **2**, 054013 (2014).
- [101] L. O. Nascimento, E. C. Marino, V. S. Alves and C. Morais Smith, [arXiv:cond-mat/1702.01573](https://arxiv.org/abs/1702.01573).
- [102] N. Menezes, G Palumbo and C. Morais Smith, *Sci. Rep.* **7**, 14175 (2017).
- [103] Igor F. Herbut, V. Juricic, and B. Roy, *Phys. Rev. B* **79**, 085116 (2009).
- [104] G. Palumbo and J. K. Pachos, *Phys. Rev. Lett.* **110**, 211603 (2013).
- [105] G. Palumbo and M. Cirio, *Sci. Rep.* **5**, 10824 (2015).
- [106] M. Gomes, R. S. Mendes, R. F. Ribeiro and A. J. da Silva, *Phys. Rev. D* **43**, 3516 (1991).
- [107] T. Itoh, Y. Kim, M. Sugiura and K. Yamawaki, *Prog. of Theo. Phys.* **93**, 417 (1995).
- [108] K.-I. Kondo, *Prog. of Theo. Phys.* **98**, 211 (1997).
- [109] L. Janssen and H. Gies, *Phys. Rev. D* **86**, 105007 (2012).
- [110] V. S. Alves, W. S. Elias, L. O. Nascimento, V. Juricic and F. Peña, *Phys. Rev. D* **87**, 125002 (2013).
- [111] D. Tilahun, B. Lee, E. M. Hankiewicz and A. H. MacDonald, *Phys. Rev. Lett.* **107**, 246401 (2011).
- [112] E. V. Gorbar, V. A. Miransky, I. A. Shovkovy and P. O. Sukhachov, *Phys. Rev. B* **94**, 115429 (2016).
- [113] V. S. Alves, R. O. C. Junior, E. C. Marino and L. O. Nascimento, *Phys. Rev. D* **96**, 034005 (2017).
- [114] T. Appelquist, D. Nash and L. C. R. Wijewardhana, *Phys. Rev. Lett.* **60**, 2575 (1998).
- [115] S. Lu, C. Zhao, Y. Zou, S. Chen, Y. Chen, Y. Li, H. Zhang, S. Wen and D. Tang, *Opt. Express* **21**, 2072 (2013).
- [116] S. Chen, C. Zhao, Y. Li, H. Huang, S. Lu, H. Zhang and S. Wen, *Opt. Mat. Express* **4**, 587 (2014).

- [117] D. Wu, A. J. Pak, Y. Liu, Y. Zhou, X. Wu, Y. Zhu, M. Lin, Y. Han, Y. Ren, H. Peng, Y.-H. Tsai, G. S. Hwang and K. Lai, *Nano Lett.*, **15** (12), 8136 (2015).
- [118] I. A. Starkov and A. S. Starkov, *J. Phys.: Conf. Ser.* **741**, 012004 (2016).
- [119] S. K. Banerjee, L. F. Register, E. Tutuc, D. Reddy and A. H. MacDonald, *IEEE Electron Device Lett.* **30**, 158 (2009).
- [120] S. Peotta, M. Gibertini, F. Dolcini, F. Taddei, M. Polini, L. B. Ioffe, R. Fazio and A. H. MacDonald, *Phys. Rev. B* **84**, 184528 (2011).
- [121] D. S. L. Abergel, *Appl. Phys. Lett.* **106**, 213103 (2015).
- [122] C. Wu, B. A. Bernevig and S.-C. Zhang, *Phys. Rev. Lett.* **96**, 106401 (2006).
- [123] C. Xu and J. E. Moore, *Phys. Rev. B* **73**, 045322 (2006).
- [124] S. Giombi, I. R. Klebanov and G. Tarnopolsky, *J. Phys. A: Math. Theor.* **49**, 135403 (2016).
- [125] S. Giombi, G. Tarnopolsky and I. R. Klebanov, *JHEP* **08**, 156 (2016).
- [126] J. S. Schwinger, *Phys. Rev.* **128**, 2425 (1962).
- [127] R. Shankar and G. Murthy, *Phys. Rev. B* **72**, 224414 (2005).
- [128] W. Thirring, *Ann. Phys.* **3**, 91 (1958).
- [129] T. Li, P. Wang, H. Fu, L. Du, K. A. Schreiber, X. Mu, X. Liu, G. Sullivan, G. A. Csny, X. Lin and R.-R. Du, *Phys. Rev. Lett.* **115**, 136804 (2015).
- [130] A. V. Kotikov and S. Teber, *Phys. Rev. D* **89**, 065038 (2014).
- [131] F. R. Ruiz and F. R. Alvarez-Estrada, *Phys. Rev. D* **35**, 3161 (1987).
- [132] P. Mitra and A. Rahaman, *Ann. Phys. (N. Y.)* **249**, 34 (1996).
- [133] H. Georgi and Y. J. Kats, *High Energy Phys.* **65**, 2010 (2010).
- [134] D. Senechal, An introduction to bosonization, arXiv:cond-mat/9908262.
- [135] T. Giamarchi, *Quantum Physics in One Dimension*, Oxford University Press (2003).
- [136] J. Maciejko, C. Liu, Y. Oreg, X.-L. Qi, C. Wu and S.-C. Zhang, *Phys. Rev. Lett.* **102**, 256803 (2009).

-
- [137] J. C. Y. Teo and C. L. Kane, Phys. Rev. B **79**, 235321 (2009).
- [138] G. M. Gusev, Z. D. Kvon, E. B. Olshanetsky, A. D. Levin, Y. Krupko, J. C. Portal, N. N. Mikhailov and S. A. Dvoretzky, Phys. Rev. B **89**, 125305 (2014).
- [139] G. Tkachov, C. Thienel, V. Pinneker, B. Bttner, C. Brne, H. Buhmann, L. W. Molenkamp and E. M. Hankiewicz, Phys. Rev. Lett. **106**, 076802 (2011).
- [140] E. M. Spanton, K. C. Nowack, L. Du, G. Sullivan, R.-R. Du and K. A. Moler, Phys. Rev. Lett. **113**, 026804 (2014).
- [141] T. Lee, J. Korean Phys. Soc. **68**, 1272 (2016).
- [142] H. Zhao, C.-W. Zhang, W.-X. Ji, R.-W. Zhang, S.-S. Li, S.-S. Yan, B.-M. Zhang, P. Li and P.-J. Wang, Sci. Rep. **6**, 20152 (2016).
- [143] R.-W. Zhang, W.-X. Ji, C.-W. Zhang, S.-S. Li, P. Lia and P.-J. Wanga , J. Mater. Chem. C **4**, 2088 (2016).
- [144] C. Chin, R. Grimm, P. Julienne and E. Tiesinga, Rev. Mod. Phys. **82**, 1225 (2010).
- [145] Y. Oreg, G. Refael and F. von Oppen, Phys. Rev. Lett. **105**, 177002 (2010).
- [146] R. Egger, A. Zazunov and A. Levy Yeyati, Phys. Rev. Lett. **105**, 136403 (2010).
- [147] N. Menezes, C. Morais Smith and G. Palumbo, Phys. Rev. B **97**, 075135 (2018).
- [148] X.-L. Qi and S.-C. Zhang, Rev. Mod. Phys. **83**, 1057 (2011).
- [149] E. Fradkin, *Field Theories of Condensed Matter Physics*, Cambridge University Press (2013).
- [150] D. A. Pesin and A. H. MacDonald, Nature Materials **11**, 409 (2012).
- [151] J. K. Pachos, *Introduction to Topological Quantum Computation*, Cambridge University Press (2012).
- [152] P. Ramond, *Field Theory: A Modern Primer*, Hachette (1997).
- [153] S. M. Young, S. Zaheer, J. C. Y. Teo, C. L. Kane, E. J. Mele and A. M. Rappe, Phys. Rev. Lett. **108**, 140405 (2012).

- [154] X. Wan, A. M. Turner, A. Vishwanath and S. Y. Savrasov, *Phys. Rev. B* **83**, 205101 (2011).
- [155] D. Bercioux, D. F. Urban, H. Grabert and W. Hler, *Phys. Rev. A* **80**, 063603 (2009).
- [156] R. Shen, L. B. Shao, B. Wang and D. Y. Xing, *Phys. Rev. B* **81**, 041410(R) (2010).
- [157] D. Green, L. Santos and C. Chamon, *Phys. Rev. B* **82**, 075104 (2010).
- [158] C. Weeks and M. Franz, *Phys. Rev. B* **82**, 085310 (2010).
- [159] B. Dora, J. Kailasvuori and R. Moessner, *Phys. Rev. B* **84**, 195422 (2011).
- [160] N. Goldman, D. F. Urban and D. Bercioux, *Phys. Rev. A* **83**, 063601 (2011).
- [161] Z. Lan, N. Goldman, A. Bermudez, W. Lu and P. Ohberg, *Phys. Rev. B* **84**, 165115 (2011).
- [162] W. Beugeling, J. C. Everts and C. Morais Smith, *Phys. Rev. B* **86**, 195129 (2012).
- [163] M. Orlita, D. M. Basko, M. S. Zholudev, F. Teppe, W. Knap, V. I. Gavrilenko, N. N. Mikhailov, S. A. Dvoretiskii, P. Neugebauer, C. Faugeras, A.-L. Barra, G. Martinez and M. Potemski, *Nat. Phys.* **10**, 233 (2014).
- [164] B. Bradlyn, J. Cano, Z. Wang, M. G. Vergniory, C. Felser, R. J. Cava and B. A. Bernevig, *Science* **353**, (2016).
- [165] A. Julku, S. Peotta, T. I. Vanhala, D.-H. Kim and P. Torma, *Phys. Rev. Lett.* **117**, 045303 (2016).
- [166] Z. Zhu, G. W. Winkler, Q. Wu, J. Li and A. A. Soluyanov, *Phys. Rev. X* **6**, 031003 (2016).
- [167] M. Bercx, J. S. Hofmann, F. F. Assaad and T. C. Lang, *Phys. Rev. B* **95**, 035108 (2017).
- [168] I. C. Fulga and A. Stern, *Phys. Rev. B* **95**, 241116(R) (2017).
- [169] This pseudospin-1 characterizes an internal degree of freedom of the wavefunctions – as for layers, polarizations, sublattices etc.
- [170] G. Palumbo and K. Meichanetzidis, *Phys. Rev. B* **92**, 235106 (2015).
- [171] R. A. Krajcik and M. M. Nieto, *Phys. Rev. D* **10**, 4049 (1974).

-
- [172] C. M. Varma, Phys. Rev. B **55**, 14554 (1997).
- [173] C. M. Varma, Phys. Rev. B **73**, 155113 (2006).
- [174] G. V. Dunne, Les Houches Lectures 1998, arXiv:hep-th/9902115.
- [175] L. M. Abreu, E. S. Santos and J. D. M. Vianna, J. Phys. A: Math. Theor. **43**, 495402 (2010).
- [176] R. Schrader, Fortsch. Phys. **20**, 701 (1972).
- [177] A. N. Redlich, Phys. Rev. D **29**, 2366 (1984).
- [178] A. Niemi and G. Semenoff, Phys. Rev. Lett. **51**, 2088 (1983).
- [179] K. Ishikawa, Phys. Rev. Lett. **53**, 1615 (1984).
- [180] H. B. Nielsen and M. Ninomiya, Phys. Lett. B **105**, 219 (1981).
- [181] E. Dagotto, E. Fradkin and A. Moreo, Phys. Lett. B **172**, 383 (1986).
- [182] A. F. Bennett, Found. Phys. **46**, 1090 (2016).
- [183] S. Chakraborty and P. Phillips, Phys. Rev. B **80**, 132505 (2009).
- [184] R. G. Leigh, P. Phillips and T.-P. Choy, Phys. Rev. Lett. **99**, 046404 (2007).
- [185] R. Jackiw and C. Rebbi, Phys. Rev. D **13**, 3398 (1976).
- [186] G. Wirth, M. Olschlager and A. Hemmerich, Nat. Phys. **7**, 147 (2011).
- [187] M. Olschlager, T. Kock, G. Wirth, A. Ewerbeck, C. Morais Smith and A. Hemmerich, New J. Phys. **15**, 083041 (2013).
- [188] N. Kemmer, Proc. Roy. Soc. A **173**, 91 (1939).
- [189] M. Nowakowski, Phys. Lett. A **244**, 329 (1998).

SUMMARY

In this thesis, we investigated the effect of electron-electron interaction and gauge theories in low-dimensional condensed-matter systems by using a quantum field theory approach.

The-Fermi velocity renormalization, which reshapes the low-energy dispersion in graphene, is a signature of the non-local electronic interactions in this 2D material. This experimental observation led us to consider a gauge field to mediate the electronic interaction that does not have the same dimensional constraints as the electrons. A consistent description of the system is achieved by solving the dimensional mismatch between the electronic current and electromagnetic field via the projection of the interaction, which results in a theory called PQED. By adopting this framework, we showed in Chapter 3 that weak external magnetic fields do not modify the known logarithmic renormalization of the Fermi velocity. Here, we theoretically clarified why the measurements of the Fermi velocity performed in the group of Geim in the presence and absence of a magnetic field are identical. Still concerning interaction effects in graphene, in Chapter 4, we calculated the correction to the spin g -factor. We showed that the experiments probing the spin-splitting are well-explained by an enhanced spin g -factor, which depends on the electron density through the velocity renormalization.

After investigating the role of interactions in graphene, we carried on studies of interaction effects in time-reversal-invariant TIs. In Chapter 5, we used the projection method to investigate interaction effects between two surfaces of a 3D TI thin film. We showed that as long as the inter-surface distance is smaller than the characteristic in-plane distance, short-range interactions become more relevant, and the system can be treated as a single surface with two fermionic species. For sufficiently strong interactions, we found that short-range interactions break chiral symmetry by opening a gap in the system, and this may be interpreted as the formation of electron-hole (exciton) pairs. Thereafter, in Chapter 6, we focused

on the interaction effects at the boundary of 2D TIs. We showed that the low-energy regime of the projected 1D theory may be mapped into a helical Luttinger liquid with a Luttinger parameter that depends on the material fine-structure constant (including the dielectric constant of the substrate and the Fermi velocity instead of the speed of light). In this way, the Luttinger parameter can be tuned by changing the substrate where the TI is deposited on. Hence, it could be possible to change the interactions from repulsive to attractive by depositing the system on a metamaterial and by varying the sign of its dielectric constant.

At last, in Chapter 7, we investigated the topological response of a model defined on the Lieb lattice. This model leads to the so called Varma phase, in which staggered currents emerge in the plaquettes, in a way that breaks time-reversal-symmetry but preserves translational symmetry. This phase was proposed to describe the pseudogap regime of high- T_c cuprates. For small momenta, there is a mapping between the tight-binding model for the cuprates lattice and a quantum field theory called DKP. This connection allowed us to compute the Chern-Simons term that can be induced by radiative quantum effects. As result, we obtained a quarter-integer QHE for quasiparticles carrying charge e (or an IQHE for quasiparticles carrying charge $2e$). We suggested an experimental setup to resolve the value of the quasiparticle charge.

The research on the physics of 2D materials was boosted by the discovery of graphene in the beginning of this century. Since then, other 2D materials were experimentally realized such as silicene, stanene, germanene, TMDs etc. Differently from graphene, the lower-energy physics of these later materials may be describe by a massive Dirac theory, in which distinct masses have different meanings in condensed-matter systems. Often a mass term indicates the breaking of a symmetry, which can be associated to a different physical situation. In the concern of massive systems, there is an intensive activity towards the understanding of excitons and g-factors in TMDs. Both the electron-hole pairing and the degeneracy lifting suggest that some symmetry in the system was broken. However, specially in the case of the valley g-factor, it is still unclear how the bare value is defined, and gets modified by considering interactions effects and/or distortions in the material.

In the past few years, there has been a trend in the condensed-matter community to study new materials, which go beyond a Dirac-fermion description. An example are physical systems described by integer-pseudospin, such as the Lieb lattice. As discussed in Chapter 7, in the low-energy regime, it is possible to connect this three-band model to the DKP theory, in a similar way as graphene is related to the Dirac theory. This increases the possibilities to investigate interaction effects in three-band models by applying the technology developed for

quantum field theories, as it has been done in the past years for graphene-like systems. The field holds promises of unveiling many more models known in the scope of quantum field theory and realizing them in table-top experiments.

SAMENVATTING

In dit proefschrift hebben we het effect van elektron-elektron interactie en ijktheorieën in laag-dimensionale systemen van gecondenseerde materie onderzocht met behulp van een kwantumveldentheoretische benadering.

The-Fermi-snelheidshernormalisatie, die de lage energie-dispersie in grafen hervormt, is een handtekening van de niet-lokale elektronische interacties in dit 2D-materiaal. Deze experimentele waarneming bracht ons ertoe een meetveld te beschouwen om de elektronische interactie te bemiddelen die niet dezelfde dimensionale beperkingen heeft als de elektronen. Een consistente beschrijving van het systeem wordt bereikt door het oplossen van de dimensionale mismatch tussen de elektronische stroom en het elektromagnetische veld via de projectie van de interactie, wat resulteert in een theorie die PQED wordt genoemd. Door dit raamwerk aan te nemen hebben we in hoofdstuk 3 laten zien dat zwakke externe magnetische velden de bekende logaritmische renormalisatie van de Fermi-snelheid niet wijzigen. Hier verduidelijkten we theoretisch waarom de metingen van de Fermi-snelheid uitgevoerd in de groep Geim in de aanwezigheid en afwezigheid van een magnetisch veld identiek zijn. Nog steeds met betrekking tot interactie-effecten in grafen, in Hoofdstuk 4, berekenden we de correctie op de spin g -factor. We hebben aangetoond dat de experimenten die de spin-splitting onderzochten, goed worden verklaard door een verbeterde spin g -factor, die afhankelijk is van de elektronendichtheid door de snelheidshernormalisatie.

Na onderzoek naar de rol van interacties in grafen, voerden we studies uit van interactie-effecten in tijd-reversal-invariante TI's. In hoofdstuk 5 hebben we de projectiemethode gebruikt om interactie-effecten tussen twee oppervlakken van een 3D TI-dunne film te onderzoeken. We hebben aangetoond dat zolang de afstand tussen de oppervlakken kleiner is dan de karakteristieke afstand in het vlak, interacties op korte afstand relevanter worden en het systeem als een enkel oppervlak met twee fermionische soorten kan worden behandeld. Voor voldoende sterke

interacties vonden we dat interacties op korte afstand chirale symmetrie doorbreken door een gat in het systeem te openen, en dit kan worden geïnterpreteerd als de vorming van elektron-gat (exciton) paren. Daarna hebben we in hoofdstuk 6 aandacht besteed aan de interactie-effecten aan de grens van 2D TI's. We toonden aan dat het lage energieregime van de geprojecteerde 1D-theorie in kaart kan worden gebracht in een schroefvormige Luttinger-vloeistof met een Luttinger-parameter die afhankelijk is van de materiële fijnstructuurconstante (inclusief de diëlektrische constante van het substraat en de Fermi-snelheid in plaats van de snelheid van licht). Op deze manier kan de Luttinger-parameter worden afgestemd door het substraat waarop de TI wordt gedeponereerd te veranderen. Vandaar dat het mogelijk zou kunnen zijn om de interacties van afstotend naar aantrekkelijk te veranderen door het systeem op een metamateriaal te deponeren en door het teken van zijn diëlektrische constante te variëren.

Afsluitend, in Hoofdstuk 7, onderzochten we de topologische respons van een model gedefinieerd op het Lieb-rooster. Dit model leidt naar de zogenaamde Varma-fase, waarin gespreide stromingen in de plaquettes verschijnen, op een manier die de T-symmetrie verbreekt, maar de translationele symmetrie behoudt. Deze fase werd voorgesteld om het pseudogap-regime van hoge-T_c-cupraten te beschrijven. Voor kleine momenten bestaat er een mapping tussen het strakke bindende model voor het cuprates-rooster en een kwantumveldentheorie, DKP genaamd. Deze verbinding stelde ons in staat de Chern-Simons term te berekenen die kan worden opgewekt door stralingskwantumeffecten. Als resultaat hebben we een kwart-integer QHE verkregen voor quasipartikels met lading e (of een IQHE voor quasipartikels met lading $2e$). We hebben een experimentele opzet voorgesteld om de waarde van de quasideeltjeslading op te lossen.

Het onderzoek naar de fysica van 2D-materialen werd gestimuleerd door de ontdekking van grafen in het begin van deze eeuw. Sindsdien zijn andere 2D-materialen experimenteel gerealiseerd, zoals siliceen, staneen, germaneen, TMD's enz. Anders dan bij grafen kan de lagere energie-fysica van deze latere materialen worden beschreven door een massieve Dirac-theorie, waarin verschillende massa's verschillende betekenissen hebben in gecondenseerde materiesystemen. Vaak duidt een massaperiode op het verbreken van een symmetrie, die kan worden geassocieerd met een andere fysieke situatie. In het onderzoek naar massieve systemen is er intensieve activiteit gericht op het begrijpen van excitonen en g-factoren in TMD's. Zowel de elektron-gat-koppeling als de degeneratie-opheffing suggereren dat er een symmetrie in het systeem was verbroken. Met name in het geval van de dal-g-factor is het echter nog steeds onduidelijk hoe de onbetrouwbare waarde is gedefinieerd en wordt gewijzigd door interactie-effecten en / of vervormingen in het materiaal te beschouwen.

In de afgelopen paar jaar is er een tendens in de gemeenschap van gecondenseerde materialen om nieuwe materialen te bestuderen, die verder gaan dan een beschrijving van Dirac-fermion. Een voorbeeld zijn fysieke systemen die worden beschreven door integer-pseudospin, zoals het Lieb-rooster. Zoals besproken in hoofdstuk 7, is het in het lage-energieregime mogelijk om dit driebandsmodel aan te sluiten op de DKP-theorie, op een vergelijkbare manier als grafeen gerealiseerd is aan de Dirac-theorie. Dit vergroot de mogelijkheden om interactie-effecten in driebandsmodellen te onderzoeken door de technologie toe te passen die is ontwikkeld voor kwantumveldentheorieën, zoals in de afgelopen jaren voor grafeenachtige systemen is gedaan. Het veld bevat beloftes van het onthullen van nog veel meer modellen die bekend zijn in het kader van de kwantumveldentheorie en het realiseren ervan in experimenten.

ACKNOWLEDGMENTS

No man is an island (pt: Nenhum homem é uma ilha) – John Donne.

Começo meus agradecimentos com esta citação como meio de reconhecer a contribuição e importância de outras pessoas (direta- ou indiretamente) para o meu crescimento, tanto profissional quanto pessoal.

À minha orientadora, Cristiane, agradeço primeiramente pela oportunidade de fazer parte de seu grupo de pesquisa e pela confiança em mim depositada. Foram inúmeras lições e desafios nesses quatro anos de trabalho que hoje reconheço a fortuna que tive de encontrar uma orientadora tão empática, acessível e cujo entusiasmo em relação à Física contagia. Obrigada por cruzar meu caminho com sua atitude positiva e otimista, e por todos os conselhos sobre a vida em geral – minha sincera admiração e respeito.

A special thank you to all my scientific collaborators: Eduardo Marino, Giandomenico Palumbo, Leandro Nascimento, Leonardo Nascimento, Van Sergio Alves; and the master students I have worked with: Sander Kooi and Charlotte Beneke. I have learned a lot from you, maybe even more than you imagine. Thank you also to all other Cristiane's group members I had the pleasure to meet and discuss ideas.

To my friends, new and old ones, I am grateful for all the support not only now, but also in the past. Às minhas amigas Marina, Vitória e Yasmin, obrigada pela visita e pelo apoio nesta fase tão decisiva da minha vida. Aos meus outros amigos brasileiros Lucas, Tays, Sílvio, Thamy, Mateus, Jonas, José, muito obrigada por tudo que passamos juntos. To Leandro, Hai-Qing, Giandomenico, Tatjana, Mônica, Marco, Henrique and Giuliana, thank you so much for everything, life in Utrecht would have been harder without you.

To my beloved boyfriend Davide, grazie mille tesoro per tutto che fai e hai fatto per me. Sou muito feliz por ter encontrado uma pessoa carinhosa e companheira como você, e com uma família tão acolhedora como a sua (obrigada também aos seus pais pelo apoio).

Aos meus pais, Ana Paula e Josenildo, não há palavras que expressem toda minha gratidão pelo amor, educação e apoio que vocês me deram todos esses anos. Tenho muito orgulho e sorte de ter pais como vocês, e esta tese é resultado também dos valores por vocês a mim repassados. Agradeço também aos meus dois irmãos, Lucas e Mateus. À minha sobrinha Lis, que trouxe alegria em momentos difíceis, e a minha cunhada Camila pelo apoio nesses quatro anos. À toda família (tios, tias, primos, primas), muito obrigada, em especial, à minha avó Valdecy, uma pessoa cheia de vida que sempre me traz paz com seus conselhos. Amo todos vocês!

At last, I want to thank CNPq, the Brazilian funding agency that supported this PhD Thesis through the Brazilian government project *Science Without Borders*.

CURRICULUM VITAE

I was born in Recife, Brazil, on the 28th of December 1990. I have lived in different cities in Brazil while growing up, but the one I spent most of my school years was Belém, in the north of the country. In Belém, I attended highschool at Escola Tenente Rêgo Barros, which I concluded in 2007. In the following year, I started my bachelor studies in physics at Universidade Federal do Pará, which I finished in 2012. Soon after the end of my bachelor studies, I was admitted in the Masters Program at the same university to study theoretical physics with a scholarship given by the Brazilian funding agency CAPES. I received my masters degree in 2014 under the supervision of Van Sérgio Alves. In the same year I was awarded a scholarship, within the Brazilian government project Science without Borders, to pursue my doctoral degree at Utrecht University in the Netherlands under the supervision of Cristiane Morais Smith. This thesis is the result of the past four years.

